

**Magnetoelectric effects in ferromagnetic metal-oxide
junctions via modulation of interfacial magnetic anisotropy**

強磁性金属酸化物接合における界面磁気異方性の磁電効果

Angshuman Deka

School of Computer Sciences and Systems Engineering

Kyushu Institute of Technology, Japan

Copyright by 2020, A. Deka

Advisory Committee

Prof. Yasuhiro Fukuma, PhD advisor

Prof. Hironori Asada

Prof. Edmund Soji Otabe

Prof. Takeshi Okamoto

ABSTRACT

Magnetoelectric effects in ferromagnetic metal-oxide junctions via modulation of interfacial magnetic anisotropy

Angshuman Deka, Doctor of Philosophy

Supervisor: Prof. Y. Fukuma

Kyushu Institute of Technology, Iizuka, Japan 2020

Spintronics refers to the field of study which aims to overcome the limitations of charge currents using the spin angular momentum of electrons. Conventionally, in the field of information technology, efficient computing power has been targeted by increasing the density and switching speeds of field effect transistors (FETs) in the chips. However, as FETs are being scaled down to the nanometer regime, losses due to tunneling and capacitive effects increase drastically, in addition to Joule heating arising from an increase in the current driven interconnects' density in the chips. One of the preferred solutions to circumvent such issues is to eliminate the use of charge flow and transition towards magnetic devices for computing and storage. Naturally it then becomes important to have an efficient method to control such magnetic devices, in the same way as charges are being used for electronic devices. Spin currents and waves are emerging as a potential candidate in this regard. In addition, an efficient mechanism to generate magnetization dynamics for spin currents and waves is of utmost importance. Of particular interest today, is the ability to generate short wavelength and high frequency spin waves, which opens the route for miniaturization of spin wave based computing devices.

Traditionally, Oersted fields have been used to control magnetization for use in magnetic devices. But it was soon observed that the spin of an electron can also manipulate the magnetization via spin-transfer torque (STT) or spin-orbit torque (SOT). But at present, charge current densities of $\sim 10^{10} \text{Am}^{-2}$ is required for exciting magnetization dynamics via STT and SOT. Controlling

magnetization using electric-fields, on the other hand, can eliminate the need for charge flow. Of particular interest in the pursuit for power efficient computing is the ability to control magnetization of metallic ferromagnets using voltage controlled magnetic anisotropy (VCMA). Experimental demonstration of the control of coercive fields in FePd thin films using electric fields¹ spurred a series of research towards the control of magnetization in ultrathin ferromagnetic films using VCMA². Pioneering research on high frequency magnetoelectric effects in ferromagnetic metal/oxide junctions were recently reported using VCMA of perpendicular magnetic anisotropy (PMA) viz. ferromagnetic resonance (FMR) excitation, followed quickly by demonstration of magnetization switching and spin wave excitations using electric-fields³⁻⁶. However, electric-field excitation of magnetization dynamics in perfectly in-plane and out-of-plane magnetized films was not possible using voltage-controlled PMA because the corresponding torque on magnetization is a function of $\sin\theta\cos\theta$, θ being the elevation angle of the magnetization from the film plane. This proves to be counterintuitive for VCMA as a magnetic field is required to initiate voltage-controlled magnetization dynamics. Therefore, in order to achieve purely voltage-controlled magnetization dynamics, it becomes essential to have a non-zero electric-field torque on magnetization vector when it is oriented along its easy axis. In this thesis, we will discuss how the easy cone state can be used to control magnetization using electric fields. Subsequently, we will discuss another technique wherein we modulate the symmetry of the interfacial magnetic anisotropy of a ferromagnetic metal-oxide junction. Such a control of the interfacial symmetry of magnetic anisotropy enables us to have non-zero electric-field torque on magnetization oriented along its easy axis.

We chose the CoFeB/MgO junctions for studying the electric-field induced mechanisms. These junctions can be stabilized in the easy cone state which can potentially be used for purely voltage-controlled magnetization. We performed micromagnetic simulations to understand the magnetization switching behavior of an MTJ free layer as a function of anisotropy. It is seen that the electric-field can be used to excite magnetization dynamics and thereby switch the magnetization when the sample is in an easy cone state. While the effective PMA energy of the easy cone state is fundamental in determining

the minimum switching fields as expected, we find that the switching speeds are dependent on the angle of the easy cone state.

A non-zero electric-field torque can also be expected for in-plane magnetized films if the interfacial magnetic anisotropy has an in-plane uniaxial component $K_{u//}$, which is expressed in the form $K_{u//}\cos^2\theta\cos^2\phi$, ϕ being the azimuthal angle. Using temperature dependent measurements of magnetic anisotropy fields, we observed that in addition to the PMA, the in-plane magnetic anisotropy (IMA) could also have an interfacial origin in ultrathin CoFeB/MgO junctions. This is confirmed by our ability to control both using electric-fields. The high frequency response of both the anisotropy fields were confirmed by the electric-field induced ferromagnetic resonance (FMR). The most important aspect of our observations is that we were able to excite FMR using electric-fields for in-plane magnetized junctions. Using a combination of finite element method simulations and theory, we developed a phenomenological model to confirm the contribution of VCMA of IMA in the process of exciting FMR. This kind of an excitation can be used to generate spin current and spin waves that can be very useful towards the emerging field of spin-based logic devices.

Using micromagnetic simulations, we investigated the magnetization trajectories during FMR because they determine the spin current generation via spin pumping. It reveals that in CoFeB/MgO junctions, the spin pumping efficiency could be expected to be highest for the value of PMA where the corresponding ellipticity of precession trajectory is ~ 0.5 . The corresponding effective demagnetizing field $H_{d,eff}$ is found to be > 0 indicating an in-plane easy axis. Following the micromagnetic simulations, we fabricated devices to study spin pumping efficiency from CoFeB/MgO junctions into Ta underlayer. The spin current generation was found to be higher for samples where the PMA field is slightly lower than the demagnetizing field, confirming our observations from the simulations. A maximum spin current density generated in our electric-field controlled device of $\sim 1.5 \times 10^9 \text{ Am}^{-2}$ when $H_{d,eff} \sim 100 \text{ mT}$, while the corresponding spin current density for a sample with $H_{d,eff} \sim -100 \text{ mT}$ was estimated to be 1 order less for an equal input power.

Increase in the excitation power results in higher precession cone angles as observed from micromagnetic simulations. It also shows that the frequency of magnetization component parallel to the static field is twice of the applied frequency. Such an oscillating component can give rise to parametric excitation in the high-power regime, useful for excitation of exchange wavelength spin waves⁷. Therefore, finally the results on non-linear magnetization dynamics in CoFeB/MgO junctions are presented. Excitation of parametric resonance using electric-fields was observed in the high input power non-linear regime. The origin of this parametric excitation is estimated to be due to VCMA of IMA. The most interesting aspect is that parametric resonance for in-plane CoFeB/MgO junctions allow us to access higher frequency magnons towards lower magnetic fields compared to similar perpendicular magnetized junctions. This is therefore an important step for device miniaturization in the field of high frequency spin wave logic applications.

In conclusion, we have explored the ability to excite purely electric-field induced magnetization dynamics in this thesis. At first, we investigated the electric-field effects in an easy cone magnetization. Using micromagnetic simulations we studied the electric-field induced magnetization switching of samples as a function of their easy cone angles. Subsequently, we also controlled the symmetry of interfacial magnetic anisotropy and used it to overcome the limitations posed by VCMA of PMA. The VCMA of IMA was shown to enable excitation of magnetization dynamics using microwave electric-fields for in-plane magnetized CoFeB/MgO junctions. Such an excitation allows us to inject spin current from the CoFeB/MgO junctions into the adjacent layers. Spin pumping efficiency, which depends on precession trajectories during FMR, was found to be able to be controlled using the magnetic anisotropy. Using electric field, which is an efficient source of magnetic excitation, we were able to excite parametric resonance in in-plane CoFeB/MgO junctions. In addition to its CMOS compatibility, parametric resonance in these junctions enable us to excite exchange interaction dominated spin waves that have higher frequencies towards lower fields. Therefore, the culmination of experimental, simulation and theoretical results presented in this thesis could significantly enable us to understand and devise efficient ways to control magnetization purely using electric-fields in future computing technologies.

References:

1. M. Weisheit *et al.*, *Science* **315**, 349–351 (2007).
2. F. Matsukura *et al.*, *Nat. Nanotechnol.* **10**, 209-220 (2015).
3. T. Nozaki *et al.*, *Nat. Phys.* **8**, 491–496 (2012).
4. J. Zhu *et al.*, *Phys. Rev. Lett.* **108**, 197203 (2012).
5. Y. Shiota *et al.*, *Nat. Mater.* **11**, 39–43 (2012).
6. B. Rana *et al.*, *Appl. Phys. Lett.* **111**, 052404 (2017).
7. C.W. Sandweg *et al.*, *Phys. Rev. Lett.* **106**, 216601 (2011).

LIST OF PUBLICATIONS

This thesis is based on the results derived from experiments and simulations reported in the following papers:

1. Electric-field control of interfacial in-plane magnetic anisotropy in CoFeB/MgO junctions; A. Deka, B. Rana, R. Anami, K. Miura, H. Takahashi, Y. Otani and Y. Fukuma; *Physical Review B* **101**, 174405 (2020).
2. Modulation of magnetization precession trajectories by perpendicular magnetic anisotropy in CoFeB thin films; A. Deka, I. Tanaka, J. Mohan and Y. Fukuma; *IEEE Transactions on Magnetics* **56**, 7 (2020).
3. Simulations on the effect of magnetic anisotropy on switching of an easy cone magnetized free layer; A. Deka, K. Sato, I. Tanaka and Y. Fukuma; *IEEE Transactions on Magnetics* **56**, 3 (2020).
4. Voltage driven generation of exchange magnons from an in-plane magnetized Ta/CoFeB/MgO junction; A. Deka, B. Rana, R. Anami, K. Miura, H. Takahashi, Y. Otani and Y. Fukuma. (to be submitted).

CONTENTS

Chapter 1. Introduction	1
1.1. Evolution of magnetization control using electrical techniques.....	2
1.2. Utilizing electrical magnetization control techniques storage and logic device applications.....	6
1.3. Importance of CoFeB/MgO junctions and a major shortcoming of VCMA.....	9
1.4. Overview of the thesis.....	11
References for Chapter 1.....	12
Chapter 2. Methods: Experimental and Simulations	15
2.1. Thin film deposition.....	15
2.2. Magnetic annealing.....	16
2.3. Deposition of coplanar waveguides for ferromagnetic resonance measurements.....	17
2.4. Fabrication of current and electric field controlled spin pumping devices.....	18
2.5. Measurement techniques.....	21
2.5.1. FMR measurements	
2.5.2. Spin pumping and ISHE measurements.	
2.6. Micromagnetic simulations.....	23
2.6.1. Ferromagnetic resonance (FMR) simulations	
2.6.2. Magnetization switching simulations	
2.7. COMSOL Multiphysics simulations.....	25
References for Chapter 2.....	26
Chapter 3. Control of the symmetry of magnetic anisotropy in CoFeB/MgO junctions using magnetic annealing	27
3.1. Introduction.....	27
3.2. Estimation of magnetic anisotropy fields using in-plane angular dependence of FMR.....	31

3.3. Annealing temperature dependence of saturation magnetization.....	34
3.4. Estimation of magnetic anisotropy using ferromagnetic resonance.....	37
3.5. Temperature dependence of saturation magnetization and magnetic anisotropy.....	41
3.6. Conclusion.....	45
References for Chapter 3.....	46

Chapter 4. Micromagnetic simulations on the effect of magnetic anisotropy on switching of an easy cone magnetized free layer.....

4.1. Introduction.....	48
4.2. Easy cone state and thermal stability.....	50
4.3. Magnetization switching using electric-fields.....	53
4.4. Conclusions.....	57
References for Chapter 4.....	58

Chapter 5. Electric-field induced magnetization dynamics in an in-plane magnetized CoFeB/MgO junctions.....

5.1. Introduction.....	59
5.2. Modulation of magnetic anisotropy using a DC bias voltage.....	62
5.3. Angular dependence of torque on magnetization and rectified voltages from spin pumping.....	68
5.4. Field distribution in CoFeB/MgO junctions due to microwave voltages.....	73
5.5. Excitation of magnetization dynamics using electric-fields.....	77
5.6. Conclusions.....	80
References for Chapter 5.....	81

Chapter 6. Efficient generation of spin current and excitation of parametric resonance using electric fields.....

6.1. Introduction.....	83
6.2. Dependence of magnetization trajectories on perpendicular magnetic anisotropy.....	87

6.3. Enhanced spin pumping using electric fields.....	94
6.4. Power dependent inverse spin Hall spectra.....	97
6.4.1. Change of lineshapes of uniform resonance peak at higher excitation power	
6.4.2. Parametric resonance using electric-fields	
6.5. Conclusions.....	105
References for Chapter 6.....	106
Conclusions and future outlook based on the results reported in this thesis.....	108
Acknowledgements.....	111

Chapter 1

Introduction

Recent developments in the field of information technology has enabled us to communicate faster, store data more efficiently and increase the computing speeds significantly. This can largely be attributed to the efficient design of our computers that is based on the so-called *von Neumann* computing architecture using complementary metal oxide semiconductors (CMOS) technology. The fundamental aspect of this architecture is that the logic and memory devices in a computing machine, both of which have different circuit designs, are fabricated side by side on the same wafer and are interconnected by layers of wires. However, the separation poses a limitation in terms of increasing the communication speeds between the logic and memory devices. In addition, with reduction in device sizes to the nanometer scales, tunneling and capacitive losses emerge from the capacitive memories and field effect transistors used in the logic devices. Thus there is an imminent need for alternative architecture to improve the computing efficiency further. Recently significant progress has been made in the field of spintronics that gives us the idea for a new kind of architecture wherein the properties of spins can be utilized to integrate the logic and storage functionalities of computing elements. This could eliminate the need for having separate logic and memory devices. Such a feature of the spin based electronics i.e. spintronics promises to overcome the challenges faced in the *von Neumann* computing mechanism and thereby enable us to further improve the computing efficiency.

In this chapter the evolution of the various methods to control the magnetization using electric techniques will be first discussed. Following this, the use of these techniques towards storage and logic applications will be discussed with a focus on the importance of electric-field controlled magnetization. Subsequently, a brief discussion on the reason for choosing CoFeB/MgO junctions will be presented along with a major shortcoming of electric-field controlled magnetization. This shortcoming will form the purpose behind the work performed in this thesis. Finally, a brief overview of the simulations and experiments performed to achieve that purpose will be given in the last section of this chapter.

Section 1.1. Evolution of magnetization control using electrical techniques

Spintronics is the field of study that utilizes the property of the spin angular momentum of an electron instead of, or in addition, to its charge that is typically used in electronic devices. The discovery of giant magnetoresistance (GMR) effect in 1988 gave rise to a surge in research that tried to utilize the property of electrons spin to add new functionalities in electronic devices [1]. The sheer importance of this discovery of GMR, which refers to the magnetic-field dependent change of resistance in a magnetic multilayer, was acknowledged by the scientific community when its' discoverers Prof. A. Fert and Prof. P. Gruhnberg were awarded the Nobel Prize in 2007. Following the discovery of GMR, spin valve structures were invented in 1991, which came to be widely used in storage devices as magnetic field sensors owing to their sensitivity at low magnetic fields [2,3]. Another milestone in this field was in 1995 with the discovery of tunnel magneto resistance (TMR) junctions which is the combination of two metallic ferromagnetic electrodes separated by a 1-2 nm thick insulating tunnel barrier [4,5]. These magnetic tunnel junctions (MTJs) enabled magnetoresistance values to reach upto 500% [6-8]. Being magnetic devices, they also possess the property of non-volatility and thereby can be potentially used for memory applications. Yet another phenomenon that emerged from these junctions was that of spin dependent tunneling of electrons through the tunnel barrier that could give rise to a spin polarized current [9,10]. This has potential applications in logic device applications. Such properties could enable us to have both logic and memory functionalities in the same device, which can overcome the limitations posed by *von Neumann* computing. The very next requirement is of an efficient mechanism to manipulate the magnetization of an MTJ free layer. An electrical technique to control the magnetization is desirable since it can be compatible with the CMOS processes. Therefore, traditionally, Oersted fields generated from charge currents flowing in close proximity to the MTJs were used to control their free layers.

An important aspect of spin currents that was observed from the spin polarized currents in an MTJ is that spin current can also enable us to actuate magnetic devices. The simplest example would be the phenomenon of spin transfer torque (STT) on magnetization arising from the spin polarized

currents in a magnetic multilayer structure [11,12]. STT was predicted in 1996 independently by Slonczewski and Berger and experimentally demonstrated soon after [13]. It arises due to the exchange interaction between spins of the incoming polarized electrons and that of the local magnetization. A major achievement of this discovery was that it laid the foundation for spin currents as a source to control magnetization, instead of magnetic fields [13-15]. A schematic description of the phenomenon of STT is shown in Fig. 1.1a. Such an alternative mechanism for controlling the magnetization in a magnetic layer enables us to reduce the current densities and in turn the Joule heating. Infact, STT based magnetic random access memories (MRAMs) are in the final stages of development and are soon expected to be introduced in the market.

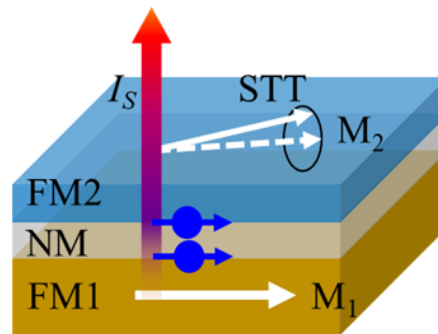


Figure 1.1, Schematic of the spin transfer torque (STT) phenomenon. FM1 and FM2 represent the two ferromagnetic layers separated by a non-magnetic (NM) layer. Magnetization of the two corresponding layers are M_1 and M_2 . Spin polarized current (circles with arrows) is represented by I_s . M_2 can be manipulated via STT if it is non collinear with M_1 .

Soon thereafter, yet another alternative technique to manipulate magnetization was discovered, namely spin-orbit torque (SOT). As the name suggests, SOT originates from the spin-orbit coupling (SOC) in structures lacking inversion symmetry [16,17]. When an electron moves in such a structure, it experiences a net electric field. Such an electric field translates into a magnetic field in the electron's rest frame as a result of which the spin of the electron is coupled to its orbital motion. Following theoretical predictions that such a spin-orbit field might intrinsically exist in ferromagnets, SOT induced magnetization switching [18-20], ferromagnetic resonance (FMR) [21], nano-oscillators [22] and spin-wave excitations [23] were demonstrated. It should be noticed that the SOT is fundamentally different

from STT in the fact that orbital angular momentum can be directly transferred to the spin angular momentum through spin orbit interaction intrinsic to the ferromagnet. STT, on the other hand, transfers the angular momentum of one ferromagnetic layer to another. Hence, SOT doesn't necessarily require two non-collinear ferromagnetic layers to manipulate magnetization like STT. Technologically, this is one of the most important achievements of SOT over STT because of the possibility of new spintronic device architectures [18-20]. The most common example of this can be seen from Fig. 1.2 which describes an SOT phenomenon. It can be seen that magnetic manipulation can be realized in a single ferromagnetic layer. This helps us to overcome one of the major drawbacks of STT based devices wherein the read and write paths interfere to cause effects detrimental to the performance of the devices. Another advantage of SOT was the reduction in current densities required to excite magnetization dynamics or switching. For example, recent experiments on magnetization switching and spin-wave excitation using SOT reported current densities of about 10^{10} Am⁻² [23,24]. On the contrary, typical current densities reported for the similar purposes using STT are atleast one order higher [25,26]. However, the current densities for exciting magnetization dynamics using SOT still give rise to significant Joule heating. Thus, for ultralow power spintronic devices, alternative techniques to further reduce current densities is desirable.

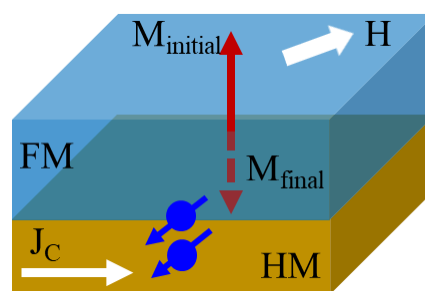


Fig. 1.2 Schematic of the spin orbit torque (SOT) phenomenon. A charge current passing through a heavy metal (HM) can be converted to a transverse spin current due to its high spin Hall angle. This spin current (circles with arrows) can exert torque on the magnetization of an adjacent ferromagnetic layer (FM). Such an SOT can be used to switch the magnetization from an initial M_{init} to final position M_{final} state. Typically, such experiments are performed in the presence of an external field H .

One of the major successes of modern computing technology lies in the development of field effect transistors (FETs) where an electric-field is used to control the output properties of a transistor. The highly localized nature of electric-fields has enabled the scaling down of FETs down to few tens of nanometers and in turn enhanced computing power significantly. Following the success of FETs, it became desirable to be able to control the magnetization using electric-fields. Infact, in 2000, Ohno *et al.* reported the electric-field control of semiconducting ferromagnets by modulating the Curie temperature T_c of (Ir,Mn)As system [27]. This was soon followed by the demonstration of magnetization reversal in a ferromagnetic semiconductor [28]. However, it should be noted that magnetization in semiconductors typically exist below room temperatures and therefore, control of ferromagnetism at room temperature is desired.

An ideal candidate would be the metallic ferromagnets Fe, Co and Ni, which have T_c much higher than room temperature. In 2007, Weisheit *et al.* demonstrated the electric-field control of coercive fields in FePd and FePt ultrathin films with a high surface-to-volume ratio [29]. Theoretical studies by Duan *et al.* and Nakamura *et al.* on the 3d transition ferromagnetic metals showed that giant modification of interfacial magnetocrystalline anisotropy is possible using electric-fields [30,31]. Following this, a series of research in the field of electric-field control of magnetization ensue, most notably the demonstration of voltage controlled magnetic anisotropy (VCMA) in ultrathin Fe films [32]. The origin of VCMA was proposed to be from the electric-field dependent electron occupancy in the d orbitals of Fe [32]. In 2012, demonstration of FMR excitation using electric-fields by Nozaki *et al.* and Zhu *et al.* showed that electric-fields can be used to control magnetization in the high frequency regime [33,34]. This was followed by the demonstration of magnetization switching and excitation of spin waves using electric fields mediated via VCMA [35-37]. Such developments established electric-fields as a power efficient avenue to control magnetization compared to STT and SOT, especially because of the elimination of the need for flowing electrons in the process of magnetization control. In particular, VCMA appeared to be a promising avenue towards reaching the Landeur limit of $k_B T \ln 2$ (k_B is the Boltzmann constant) in the computing processes, which is not possible in STT and SOT mechanisms owing to the Joule heating from charge currents involved [38-40].

Section 1.2. Utilizing electrical magnetization control techniques for storage and logic device applications

One of the major applications for the spintronic devices is in the field of storage devices owing to the property of non-volatile magnetic memories. With the advent of big data and artificial intelligence, there is a requirement for faster operation and an increase in the memory density, along with a fast power efficient accessibility to the various computing elements [39-41]. One of the potential solutions in this regard is the use of MRAMs which are non-volatile, unlike their present-day counterparts that are based on capacitive memory elements [41]. MRAMs use MTJs as a building block for coding memory based on the relative magnetization orientations of the two magnetic layers. Switching of the free layer i.e. the write task has been shown to be possible using torques arising from STT, SOT and VCMA as mentioned earlier. Of particular interest is VCMA because it doesn't require the need for a charge current to control magnetization. In addition to this, it is tempting to attempt to replace the charge currents that are used for communication between the various computing elements with a spin current. Therefore, not only is it important to understand the torques arising from VCMA towards magnetization switching, it is also equally important to efficiently use it as a source of spin current generation.

Technologically, it is desirable to generate spin current without necessarily flowing a charge current through the fixed layer of an MTJ, a major drawback of the spin filtering effect. One of the most intensively researched area in this regard is the spin Hall effect (SHE) first proposed by Hirsch [42]. It refers to the generation of a transverse spin current from a charge current via SOC. Such a *pure* spin current is fundamentally different from the spin *polarized* currents in the sense that there is no effective transfer of the electronic charge along with the spins unlike in the latter. Other techniques to generate pure spin currents include non-local spin injection in lateral spin valves and spin Seebeck effect [43,44]. In 2002, Tserkovnyak *et al.* proposed that a precessing ferromagnet could pump spin currents into an adjacent material [44]. This was particularly attractive because it paved the way for the

generation of high frequency spin currents via magnetization precession induced not only by magnetic fields but also by STT, SOT and VCMA alike.

Apart from storage devices, another major emerging application of spintronics is in the field of magnonic computing which utilizes the collective excitation of magnetization moments i.e. spin waves towards developing a new class of logic devices [46-49]. Conventionally, in logic devices, efficient computing power has been targeted by increasing the density and switching speeds of field effect transistors (FETs) in the chips. However, as FETs are being scaled down to the nanometer regime, losses due to tunneling effects increase drastically in addition to Joule heating arising from an increase in the current driven interconnects density in the chips. One of the potential solutions to circumvent such issues towards future computing technology, is by replacing the charge based electronics with the properties of spin angular momentum of electrons [48]. Spin waves, known quantum mechanically as magnons, possess several advantages over the use of electrons in computing technologies [46-48]. Firstly, the substitution of a scalar variable such as electrons using spin waves allow us to have an added functionality of its phase, in addition to the amplitude of the wave as depicted in Fig. 1.4 [49]. Such a property is promising towards the development of beyond-CMOS computing technologies in the future. Spin waves can exist not only in metals but also in insulators, thereby opening an option to utilize insulating ferromagnets in the computing processes. In addition, the spin waves have a much larger decay length unlike the spin currents which usually decay within few nanometers. It can range from millimeter range in metallic ferromagnets upto centimeters in the insulating counterparts [46-47]. The wavelength of spin waves can be tuned down to the exchange interaction limit (few nanometers) by changing the magnetic fields [50]. The corresponding frequency increases with a decrease in wavelength, which not only enables spin wave based devices to be scaled down, but also simultaneously increase the speed of computing [48]. Finally, a number of demonstrations showing the benefits of non-linearity of the magnons such as parametric amplification and transmission over large distances without loss of distortion promise to bring added functionalities to magnonic computing in future [46,47].

A typical magnonic device can be considered to be made up of four major parts viz. (a) a spin wave waveguide for transmitting the spin wave, (b) an excitation source that can be done using microwave electric or magnetic fields, STT, SOT or mediated thermally, (c) a detector for detection of the incoming spin waves and (d) additional functional elements such for tasks such as amplification, manipulation or channeling [49]. In order to make such devices compatible with the existing CMOS technologies, it is quite desirable to achieve the excitation and detection aspects of a magnonic device using electrical techniques. And as expected from the major motivation of developing efficient computing techniques via magnonics, power efficient magnon excitation avenues such as STT and SOT for these tasks are typically preferred over Oersted fields. However, it should be noted that the use of STT and SOT necessitates the use of charge currents within or in close proximity to the devices. Use of charge currents proves detrimental to the device functionalities as they are scaled down. Electric fields on the other hand have emerged as an efficient mechanism to excite magnons, as demonstrated recently by the spin wave excitation in ultrathin CoFeB/MgO junctions [37]. In addition, it was also demonstrated that parametric amplification could be achieved for a perpendicularly magnetized CoFeB/MgO junction, paving the way for generating magnons with wavelengths down to the exchange scale [51]. Based on such developments in the field of VCMA, we are motivated to explore this field of electric-field controlled magnetization dynamics for ultralow power spintronic devices.

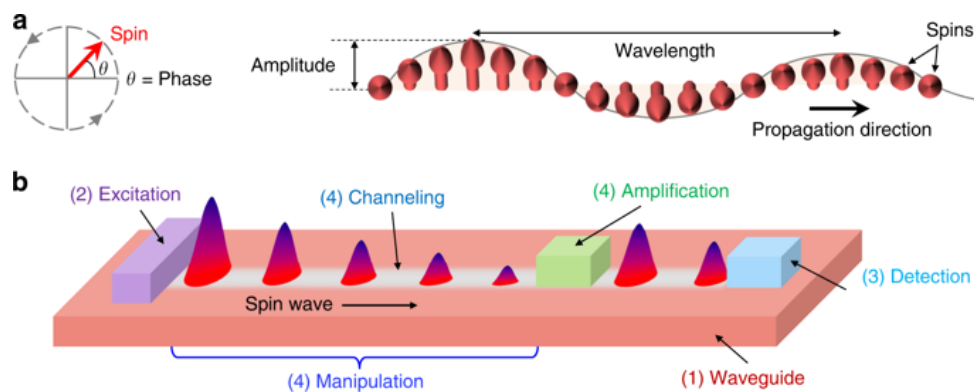


Fig. 1.4a, Schematic describing the various parameters associated with a spin wave. **b**, Schematic of a typical magnonic device. Image is reproduced with permission from B. Rana *et al* [48].

1.3. Importance of CoFeB/MgO junctions and a major shortcoming of VCMA

Section 1.1 highlighted the importance of the emergence of TMR structures in the field of spintronics. Initially most MTJ structures used an Al₂O₃ tunnel barrier but a modest TMR ratio of ~70% was a major limitation for device performances [4,5]. In 2004 Yuasa *et al.* and Parkin *et al.* independently demonstrated that by replacing the Al₂O₃ barrier with an MgO tunnel barrier, much higher TMR ratios of over 200% could be realized at room temperatures [6-8]. Of particular interest was that the ferromagnetic electrodes such as Fe or CoFe alloys used in these experiments could be deposited using scalable technologies such as sputtering [6]. Almost parallel to these discoveries, studies on magnetoelectric effects in metallic ferromagnetic films emerged, which attributed the electric-field effects to interfacial SOC [29-31,38]. Subsequent studies in 2010 revealed that interfacial anisotropy in CoFeB/MgO structures could be large enough to overcome the demagnetizing field of the ferromagnet [52]. In addition, the interfacial nature of the PMA enabled electric field modulation of magnetic properties [40]. Following this, in the same year, using the interfacial PMA of CoFeB/MgO junctions, a perpendicular anisotropy MTJ was demonstrated by Ikeda *et al.* [35]. In addition to greatly simplifying the design for a perpendicular anisotropy MTJ, these CoFeB/MgO/CoFeB junctions showed TMR ratios of over 120% and high thermal stability [35]. These findings established the CoFeB/MgO junctions as a preferred system for studying VCMA.

The PMA in these junctions arise from the hybridization between the interfacial 3*d* orbitals of the ferromagnetic atoms with that of the 2*p* orbitals of the interfacial O atoms in MgO layer [52]. This allowed the electronic occupancies to be modified not only by DC electric fields, but also microwave electric-fields leading to electric-field induced FMR and spin wave excitations in CoFeB/MgO junctions [53,37]. However, a drawback of the VCMA of PMA in the ferromagnetic metal – oxide junctions was that the electric-field torque on magnetization is zero for in-plane and perpendicular orientation of magnetization vector. Therefore, a bias magnetic field is always needed to initiate VCMA induced dynamical processes such as magnetization switching or excitation of spin waves. The need for bias fields necessitates the need for electric currents in close proximity to the devices that hampers

the power efficient nature of electric-field controlled magnetization dynamics. Thus, there is a need for solutions to overcome this limitation of VCMA for initiating dynamical magnetization processes. This can enable us to develop ultralow power devices that can be controlled purely using electric-fields.

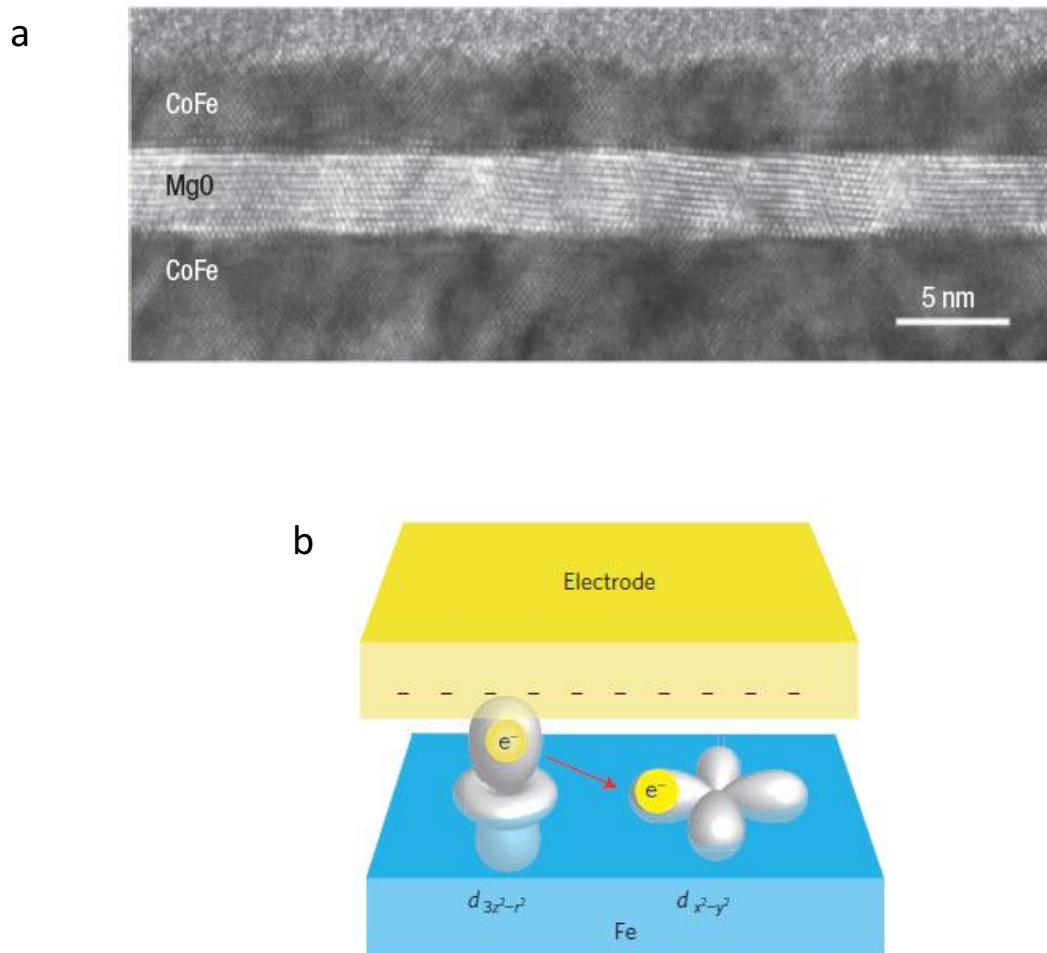


Figure 1.5a, High resolution transmission electron microscopic image of a CoFe/MgO/CoFe junction. Image is reproduced with permission from doi:10.1038/nmat1256. **b**, Mechanism of VCMA in ferromagnetic metal oxide junction. In case of CoFeB/MgO junctions, magnetic anisotropy arises from hybridization between the 3d orbitals of the ferromagnetic (FM) atom and 2p orbitals of the O atoms in the metal oxide interface. VCMA occurs via change of electron occupancies in the out-of-plane and in-plane oriented 3d orbitals of the interfacial FM atoms. Image is reproduced with permission from doi: 10.1038/nano.2008.406.

1.4. Overview of the thesis

In this thesis, we present a series of experiments and simulations in order to understand mechanisms towards achieving purely electric-field control of magnetization in ferromagnetic metals. First of all, in Chapter 2 we explain the various deposition, fabrication, measurement and simulation techniques used in this thesis. Following this, in Chapter 3, we present our experiments on the magnetic anisotropy of CoFeB/MgO junctions. We utilize magnetic annealing to control the symmetry of magnetic anisotropy in these junctions. Quite surprisingly, we observe that both PMA and in-plane magnetic anisotropy (IMA) can exhibit similar temperature dependences in ultrathin CoFeB/MgO junctions. This indicates a similar origin for both i.e. interfacial hybridization between $3d$ and $2p$ orbitals of Fe (Co) and O respectively.

Subsequently, we present our investigations towards purely electric-field controlled magnetization in CoFeB/MgO junctions. At first in Chapter 4, we present the micromagnetic simulations on electric-field induced magnetization switching in MTJs with an easy cone magnetized free layer. In addition to this, we note that the control of the symmetry of interfacial anisotropy seen in Chapter 3 could also be used towards purely electric-field controlled magnetization. In Chapter 5, we present our findings on VCMA. Electric-field effect is detected using spin pumping and inverse spin Hall effect measurements. We observe that both PMA and IMA could be modulated by DC electric-fields in ultrathin CoFeB/MgO junctions. We demonstrate that using an electric-field controllable IMA, FMR can be excited in CoFeB/MgO junctions magnetized along its in-plane easy axis. This can be used to eliminate the bias fields required to initialize electric-field induced magnetization dynamics. Finally, in Chapter 6 we focus on the efficiency of electric-field controlled magnetization dynamics towards generating spin currents and waves. We observe over 6 times higher spin pumping efficiency in electric-field controlled devices. In addition, we show that VCMA of IMA can also be used to pump parametric resonance modes. Finally, we conclude with a note regarding the main findings of this thesis and future outlook to achieve purely voltage controlled spintronic devices in future vis-a-vis the electric-field control of magnetization in easy cone and in-plane magnetized films.

References

1. M. Baibich, J.M. Broto, A. Fert, F. Nguyen Van Dau, F. Petroff, P. Etienne, G. Creuzet, A. Friederch, J. Chazelas, *Phys. Rev. Lett.* **61**, 2472–2475 (1988).
2. B. Dieny, V.S. Speriosu, S.S.P. Parkin, B.A. Gurney, D.R. Whilhoit, D. Mauri, *Phys. Rev. B Condens Matter* **43**, 1297–1300 (1991).
3. B. Dieny, R.C. Sousa, J. Hérault, C. Papusoi, G. Prenat, U. Ebels, D. Houssameddine, B. Rodmacq, S. Auffret, L. PrejbeanuBuda, M.C. Cyrille, B. Delaet, O. Redon, C. Ducruet, J.P. Nozieres, L. Prejbeanu, K.H.J. Buschow (*Ed.*), *Handbook of magnetic materials*, Elsevier 107-127 (2012).
4. T. Miyazaki, N. Tezuka, *J. Magn. Magn. Mater.* **139**, L231 (1995).
5. J.S. Moodera, L.R. Kinder, T.M. Wong, R. Meservey, *Phys. Rev. Lett.* **74**, 3273–3276 (1995).
6. S.S.P. Parkin, C. Kaiser, A. Panchula, P.M. Rice, B. Hughes, M. Samant, S.H. Yang, *Nat. Mater.* **3**, 862–867 (2004).
7. S. Yuasa, T. Nagahama, A. Fukushima, Y. Suzuki, K. Ando, *Nat. Mater.* **3** (12), 862–867 (2004).
8. S. Yuasa, A. Fukushima, H. Kubota, Y. Suzuki and K. Ando, *Appl. Phys. Lett.* **89**, 042505–042507 (2006).
9. W.H. Butler, X.-G. Zhang, T.C. Schulthess, J.M. MacLaren, *Phys. Rev. B* **63**, 054416 (2001).
10. J. Mathon and Umerski, *Phys. Rev. B* **63**, 220403–220407 (2001).
11. J. S. Slonczewski, *J. Magn. Magn. Mater.* **159**, L1-L7 (1996).
12. L. Berger, *Phys. Rev. B* **54**, 9353-9358 (1996).
13. J.A. Katine, F.L. Albert, R.A. Buhrman, E.B. Myers and D.C. Ralph, *Phys. Rev. Lett.* **84**, 3149–3152 (2000).
14. M. Tsoi, A.G.M. Jansen, J. Bass, W.-C. Chiang, M. Seck, V. Tsoi and P. Wyder, *Phys. Rev. Lett.* **80**, 4281–4284 (1998).
15. J.-E. Wegrowe, D. Kelly, Y. Jaccard, Ph. Guittienne and J.-P.H. Ansermet, *Europhys. Lett.* **45**, 626 (1999).
16. A. Manchon and S. Zhang, *Phys. Rev. B* **78**, 212405 (2008).
17. A. Manchon and S. Zhang, *Phys. Rev. B* **79**, 094422 (2009).
18. I.M. Miron, G. Gaudin, S. Auffret, B. Rodmacq, A. Schuhl, S. Pizzini, J. Vogel and P. Gambardella, *Nat. Mater.* **9**, 230-234 (2010).
19. I.M. Miron, K. Garello, G. Gaudin, P.-J. Zermatter M.V. Costache, S. Auffret, S. Bandiera, B. Rodmacq, A. Schuhl and P. Gambardella, *Nature* **476**, 189-193 (2011).
20. S. Fukami, T. Anekawa, C. Zhang and H. Ohno, *Nat. Nanotechnol.* **11**, 621-625 (2016).
21. L. Liu, T. Moriyama, D.C. Ralph and R.A. Buhrman, *Phys. Rev. Lett.* **106**, 036601 (2011).

22. H. Fulara, M. Zahedinejad, R. Khymyn, A.A. Awad, S. Muralidhar, M. Dvornik and J. Ackerman, *Science Advances* **5**, 9, eaax8467 (2019).
23. M. Haider, A.A. Awad, M. Dvornik, R. Khymyn, A. Shoushang and J. Ackerman, *Nat. Commun.* **10**, 2362 (2019).
24. S. Shi, Y. Ou, S.V. Aradhya, D.C. Ralph and R.A. Buhrman, *Phys. Rev. Appl.* **9**, 011002 (2018)
25. C.-Y. You, *Appl. Phys. Lett.* **100**, 252413 (2012).
26. M. Madami, S. Bonetti, G. Consolo, S. Tacchi, G. Carlotti, G. Gubbiotti, F.B. Mancoff, M.A. Yar and J. Ackerman, *Nature Nanotech.* **6**, 635-638 (2011).
27. H. Ohno, D. Chiba, F. Matsukura, T. Omiya, E. Abe, T. Dietl, Y. Ohno and K. Ohtani, *Nature* **408**, 944 (2000).
28. D. Chiba, M. Yamanouch, F. Matsukura and H. Ohno, *Science* **01**, 943 (2003).
29. M. Weisheit, S. Fahler, A. Marty, Y. Souche, C. Poinignon and D. Givord, *Science* **315**, 349–351 (2007).
30. C. –G. Duan, J.P. Valev, R.F. Sabirianov, Z. Zhu, J. Chu, S.S. Jaswal and E.Y Tsymbal, *Phys. Rev. Lett.* **101**, 137201 (2008).
31. K. Nakamura, R. Shimabukuro, Y. Fujiwara, T. Akiyama and T. Ito, *Phys. Rev. Lett.* **102**, 187201 (2009).
32. T. Maruyama, Y. Shiota, T. Nozaki, K. Ohta, N. Toda, M. Mizuguchi, A.A. Tulapurkar, T. Shinjo, M. Shiraishi, S. Mizukami, Y. Ando and Y. Suzuki, *Nat. Nanotechnol.* **18**, 158-161 (2009).
33. T. Nozaki, Y. Shiota, S. Miwa, S. Murakami, F. Bonell, S. Ishibashi, H. Kubota, K. Yakushiji, T. Saruya, A. Fukushima, S. Yuasa, T. Shinjo and Y. Suzuki, *Nat. Phys.* **8**, 491–496 (2012).
34. J. Zhu, J.A. Katine, G. E. Rowlands, Y-J. Chen, Z. Duan, J.G. Alzate, P. Upadhyaya, J. Langer, P.K. Amiri, K.L. Wang and I.N. Krivorotov, *Phys. Rev. Lett.* **108**, 197203 (2012).
35. S. Ikeda, K. Miura, H. Yamamoto, K. Mizunuma, H.D. Gan, M. Endo, S. Kanai, J. Hayakawa, F. Matsukura and H. Ohno, *Nat. Mater.* **9**, 721–724 (2010).
36. Y. Shiota, T. Nozaki, F. Bonell, S. Murakami, T. Shinjo and Y. Suzuki, *Nat. Mater.* **11**, 39–43 (2012).
37. B. Rana, Y. Fukuma, K. Miura, H. Takahashi and Y. Otani, *Appl. Phys. Lett.* **111**, 052404 (2017).
38. F. Matsukura, Y. Tokura and H. Ohno, *Nat. Nanotech.* **10**, 209-220 (2015).
39. S. Miwa, M. Suzuki, M. Tsujikawa, K. Matsuda, T. Nozaki, K. Tanaka, T. Tsukahara, K. Nawaoka, M. Goto, Y. Kotani, T. Ohkubo, F. Bonell, E. Tamura, K. Hono, T. Nakamura, M. Shirai, S. Yuasa and Y. Suzuki, *Nat. Commun.* **8**, 15848 (2017).
40. R. Landauer, *IBM J. Res. Dev.* **5**, 183–191 (1961).
41. S. Bhatti, R. Sbiaa, A. Hirohata, H. Ohno, S. Fukami, S.N. Piramanayagam, *Mater. Today* **20**, 530–548 (2017)

42. J.E. Hirsh, *Phys. Rev. Lett.* **83**, 1834 (1999).
43. M. Johnson and R.H. Silsbee, *Phys. Rev. Lett.* **55**, 1790 (1985).
44. K. Uchida, S. Takahashi, K. Harii, J. Ieda, W. Koshihara, K. Ando, S. Maekawa and E. Saitoh, *Nature* **455**, 778-781 (2008).
45. Y. Tserkovnyak, A. Brataas and G.E.W. Bauer, *Phys. Rev. B* **66**, 224403 (2002).
46. A.A. Serga, A.V. Chumak and B. Hillebrands, *J. Phys D: Appl Phys* **43**, 26 (2010).
47. A.V. Chumak, V.Y. Vasyuchka, A.A. Serga and B. Hillebrands, *Nat. Phys.* **11**, 453–461 (2015).
48. A. Khitun and K.L. Wang, *J. of Appl. Phys.* **110**, 034306 (2011).
49. B. Rana and Y. Otani, *Commun. Phys.* **2**, 90 (2019).
50. C.W. Sandweg, Y. Kajiwara, A.V. Chumak, A.A. Serga, V.Y. Vasyuchka, M. B. Jungfleisch, E. Saitoh, and B. Hillebrands, *Phys. Rev. Lett.* **106**, 216601 (2011).
51. Y.-J. Chen, H. K. Lee, R. Verba, J. A. Katine, I. Barsukov, V. Tiberkevich, J. Q. Xiao, A. N. Slavin, and I. N. Krivorotov, *Nano Lett.* **17**, 572 (2017).
52. M. Endo, S. Kanai, S. Ikeda, F. Matsukura and H. Ohno, *Appl. Phys. Lett.* **96**, 212503 (2010).
53. K. Miura, S. Yabuuchi, M. Yamada, M. Ichimura, B. Rana, S. Ogawa, H. Takahashi, Y. Fukuma and Y. Otani, *Sci. Rep.* **7**, 42511 (2017).

Chapter 2

Methods: Experimental and Simulations

The methods used for experiments and simulations that went into the work behind this thesis are presented in this chapter. We begin with the thin film deposition method, followed by the magnetic annealing and patterning of those these films. Finally, we describe the measurement techniques that were used to analyze the properties of our thin films.

Section 2.1: Thin film deposition

Multilayer stacks were deposited using DC Sputtering technique at room temperature at a base pressure of $\sim 1 \times 10^{-7}$ Pa. Thermally oxidized Si (100) substrates have been used for depositing the multilayer stacks. Typical multilayer stack used for the experiments presented in this thesis is of the type Substrate/Ta(5)/Ru(10)/Ta(5)/CoFeB(t)/MgO(2)/Al₂O₃(10). The nominal thicknesses of each layer mentioned in the parentheses are in nanometers (nm). The thickness of the CoFeB layers are varied from $t = 1.5$ to 5.0 nm in this study. A low thickness is essential to maintain high value of surface to volume ratio so that interfacial anisotropy is dominant in the films. As mentioned in Chapter 1, the role of MgO adjacent to the CoFeB layer is to induce PMA and therefore highly crystalline MgO is desirable for high value of PMA. However, MgO thin films are typically hydrophyllic and hence an additional capping layer is necessary. The Al₂O₃ layer serves as this capping layer to maintain the quality of the MgO layer which is very important for interfacial magnetic anisotropy.

Section 2.2: Magnetic annealing

For this process, the multilayer stacks were first cut into sizes of $\sim 2 \text{ mm} \times 2 \text{ mm}$. These samples were annealed in vacuum at different temperatures ranging from $100 \text{ }^\circ\text{C}$ to $400 \text{ }^\circ\text{C}$ in the presence of a magnetic field of 500 mT . A pressure level of $\sim 3 \times 10^{-3} \text{ Pa}$ was maintained during annealing process. The samples were placed in a carbon sample holder inside the quartz tube to ensure uniform heating as shown in Fig. 2.1. An infrared lamp placed right above the quartz tube was used as the heat source in the process of annealing. The recipe used for annealing is mentioned as follows:

- (a) Temperature was first risen from room temperature to the annealing temperature (e.g. 300°C) in 10 minutes.
- (b) Then temperature (e.g. 300°C) was maintained for 30 minutes.
- (c) Then the temperature is quenching down to room temperature in 10 minutes.
- (d) The magnetic field of 500 mT was applied during the entire annealing process starting from step (a) to step (c). The direction of this magnetic field in the samples could be varied by rotating the sample with respect to the magnetic poles.

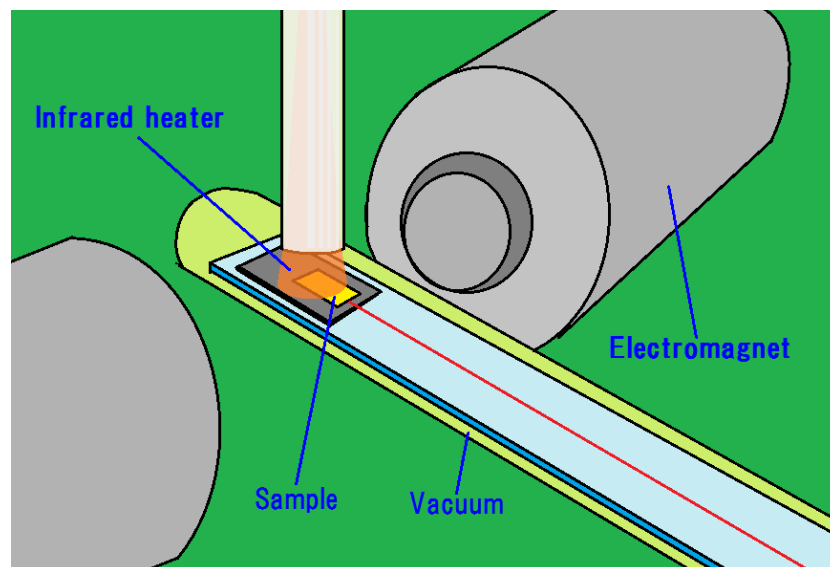


Fig. 2.1, Experimental setup used for magnetic annealing. The sample is placed on a carbon stage. A thermocouple wire (red) is placed close to the sample to note the temperature during the process.

Section 2.3. Deposition of coplanar waveguides (CPW) for ferromagnetic resonance (FMR) measurements

In order to perform FMR measurements of the magnetic thin films, we deposited 200 nm Au CPW onto patterned Sapphire substrates. Sapphire substrates were used for fabricating the CPW for FMR measurements because they allow less microwave dissipation compared to oxidized Si substrates. The signal line of the CPW used for FMR measurements was designed to be 50 μm wide. An oxide layer was deposited on the part of the CPW to provide insulation of the CPW and the magnetic thin films during FMR measurements. The oxide layer is not deposited on the open end of the CPW. This allows us to connect the microwave probe that serves as an input for microwave signals. The microwave current flowing in the CPW generates an AC microwave field that acts as the oscillating field required for FMR measurement. A typical CPW design has been shown in the Fig. 2.3a below.

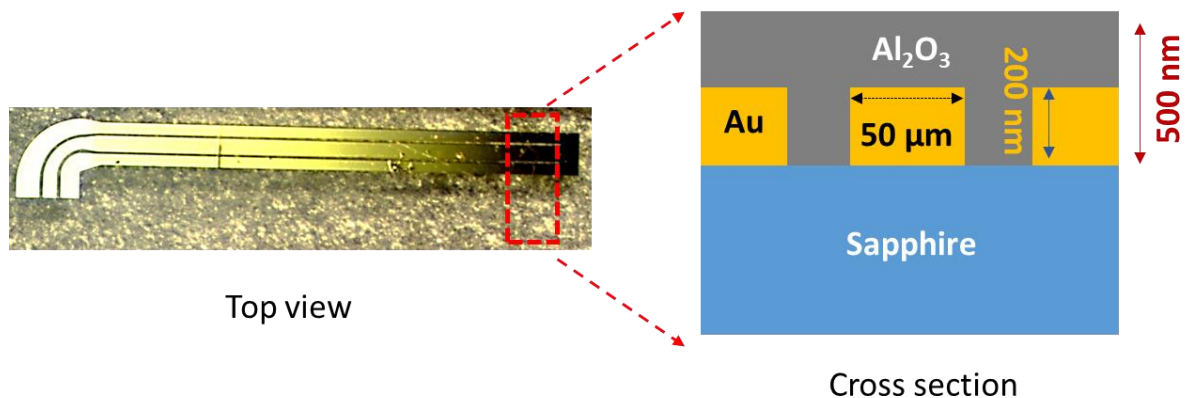


Figure 2.2, Optical image of a coplanar waveguide deposited on top of sapphire substrate. On the right is the cross sectional view of the area marked in red. Al₂O₃ is not deposited on the open end of the CPW which serves as the input port of microwave current.

Section 2.4. Fabrication of current and electric field controlled spin pumping devices

Two different types of devices were fabricated to study the electric-field effects. The first type of devices allowed us to study the effect of a DC voltage applied using the top (T) electrode while the FMR excitation is performed using Oersted fields generated from an AC current flowing in the CPW as shown in Fig. 2.3a. The second type was to study the microwave voltage effects as shown in Fig. 2.3b. Here FMR excitation was done using an electric-field applied across the top (T) and bottom (B) electrodes. Rectified voltages were detected across the Ta/Ru/Ta bottom (B) electrodes. The experimental set-ups are shown in Chapter 4. Both these devices were fabricated simultaneously on the same multilayer stack using the same steps for photolithography and etching techniques as will be explained in the next paragraph. This allows us to have the same magnetic properties in the devices which is essential while comparing the current and electric-field effects. We fabricated these devices for a wide range of multilayer stacks with CoFeB thicknesses ranging from 2.0 nm to 1.6 nm.

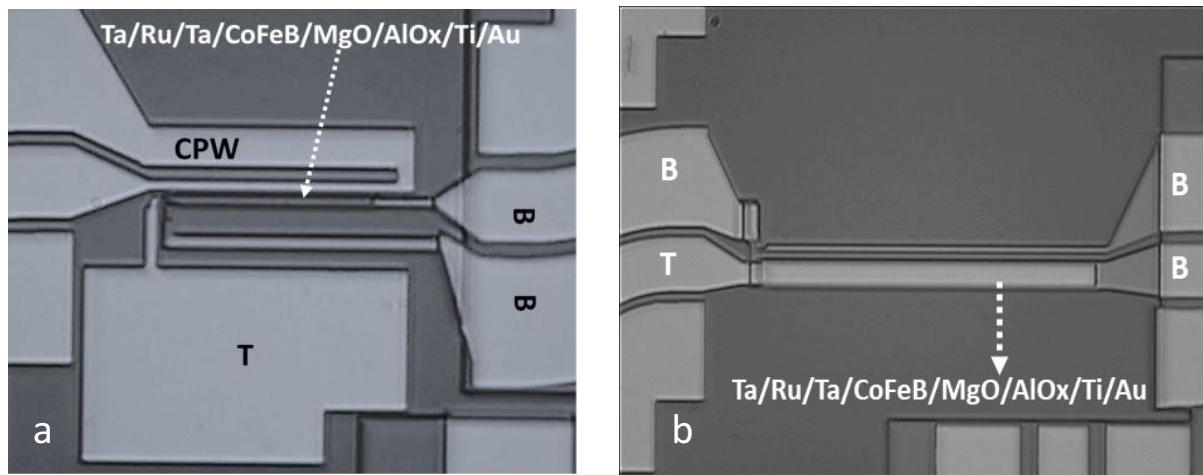


Figure 2.3a, Optical microscope image of the device used for electrical detection of FMR excited by microwave field generated by a current flowing in the coplanar waveguide (CPW). The top electrode (T) allows us to apply a DC bias voltage on the CoFeB/MgO junction. **b**, Optical microscope image of the device used for electrical detection of FMR excited by an AC electric field at the CoFeB/MgO junction. The AC electric field is applied between the top and bottom (B) electrodes. In both devices the rectified voltage is detected across the bottom electrodes.

The process of fabrication followed has been shown pictorially in the Fig. 2.4. In order to fabricate these devices, first process was to coat the multilayers with resist after proper cleaning. This is shown in the top left of Fig. 2.4. Cleaning was done by first washing the films in acetone for 15 minutes in a sonicator, followed by another 15 minutes in isopropyl alcohol and finally washed with clean water. The resist coating was done in the following steps: (a) deposit OAP (adhesion layer) using spin coater and bake at 80°C for 1 minute, (b) deposit AZ-1500 resist (positive resist) using spin coater and bake at 100°C for 1 minute. After resist coating, the first pattern was exposed onto the films using maskless photolithography. Following this, the samples are developed in NMD for 1 minute and washed in clean water for 1 minute. After confirming the correct formation of patterns, the multilayer stack was patterned into a rectangular shape of different dimensions by using Ar-ion milling. After milling, the sample was once again cleaned and the same process was repeated once again to fabricate the bottom electrodes.

Following this, we once again cleaned the samples and made the patterns using maskless photolithography for depositing an oxide layer that will serve as the insulating layer between the top and bottom electrodes. 80 nm Al_2O_3 was deposited as this insulating layer. This was once again followed by cleaning and resist coating. Finally, we make the pattern for depositing the top electrodes using maskless photolithography. Ti(10)/Au(200) was deposited as electrodes.

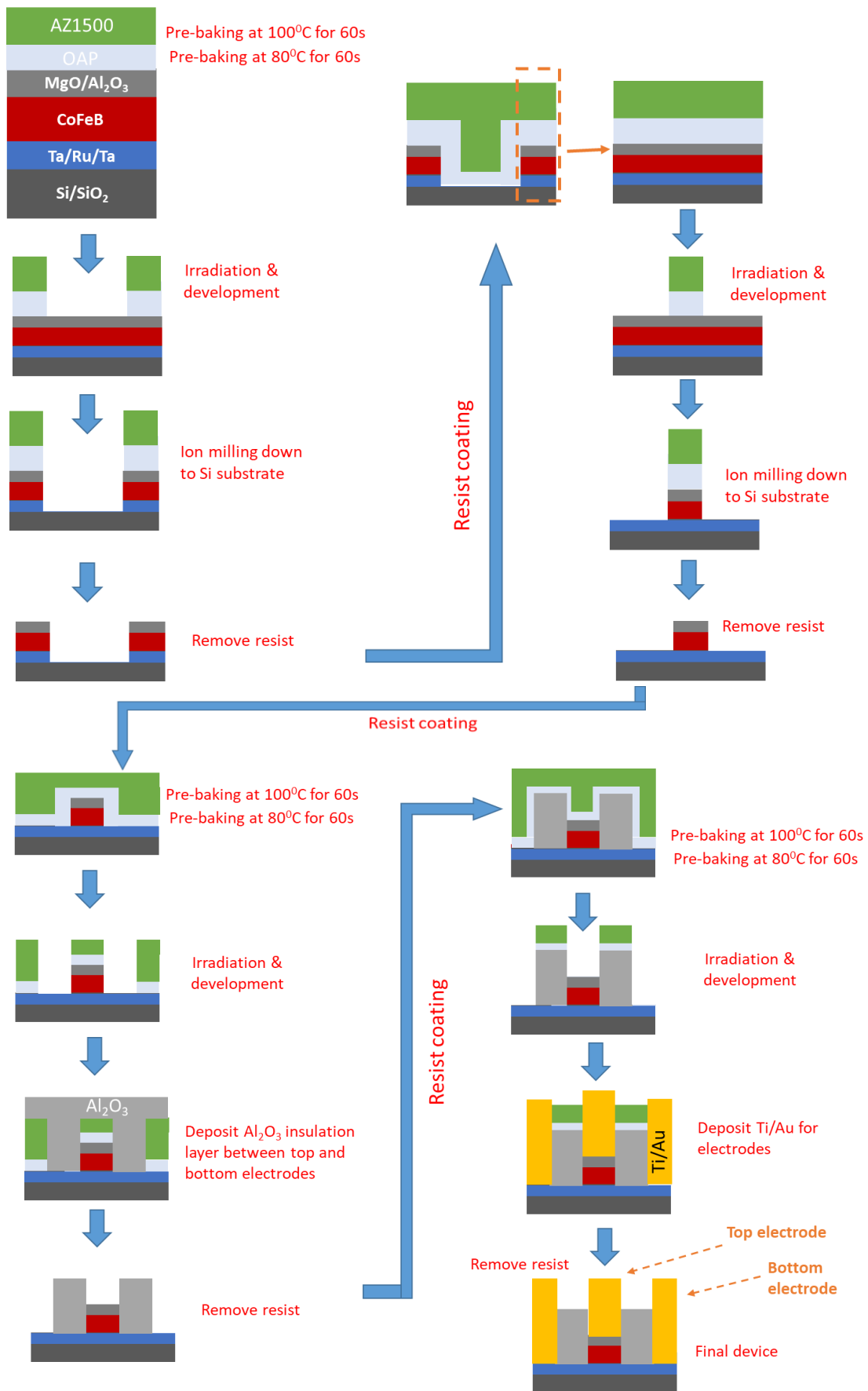


Figure 2.4, Flowchart of the process used to fabricate the spin pumping devices.

Section 2.5. Measurement techniques

2.5.1. FMR measurements

Ferromagnetic resonance spectra were recorded using a Agilent Vector Network Analyzer (VNA). The multilayer stacks used for FMR measurements were first cut into pieces of sizes $< 2 \times 2$ mm². These were then placed face down on a coplanar waveguide (CPW). The ends of the CPW was connected to the VNA which provided a microwave field of frequency f to the ferromagnetic layer via electromagnetic induction in the CPW. The VNA was calibrated using a Infinity CS5 calibration substrate by following the standard processes in the VNA Calibration wizard. FMR spectra were recorded using the S_{11} reflection coefficient in the field sweep mode. In this mode, the frequency is kept constant while sweeping the external field between -250 mT to +250 mT. A typical FMR measurement set up is shown in Fig. 2.5. The direction of the external magnetic field applied in the film plane could be varied by 360°. Such an in-plane rotation of external magnetic field is useful for estimating the magnetic anisotropy fields, as will be discussed in Chapter 3. For low temperature FMR measurements, the setup shown in Fig. 2.5 is placed inside a cryogenic probe station that uses a He compressor for reaching temperatures down from room temperature to 10 K.

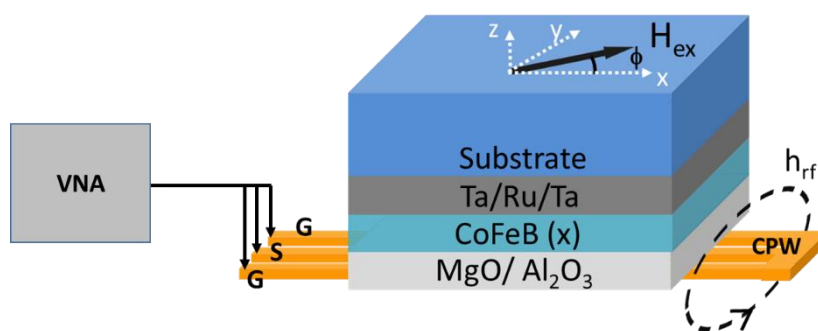


Figure 2.5, Schematic of the experimental setup used to detect FMR signal depicting the ground (G) and signal (S) terminals of the co-planar waveguide (CPW) and the direction of the applied microwave field h_{rf} . The open ends of the CPW are connected to a vector network analyzer (VNA) to measure the S_{11} reflection parameter as the external magnetic field H_{ex} a fixed frequency.

Section 2.6. Micromagnetic simulations

The micromagnetic simulations performed in throughout the thesis were performed using the Landau-Lifshutz-Gilbert (LLG) micromagnetic simulator developed by M.R. Sheinfein and E.A. Price [1]. The simulator package works by solving the standard LLG equation as shown below:

$$\frac{dM}{dt} = -\frac{\gamma}{1+\alpha^2}(M \times H_{eff}) - \frac{\gamma\alpha}{(1+\alpha^2)M_s}(M \times (M \times H_{eff})), \quad (2.1)$$

where, the term on the left represents the time t evolution of magnetization M , γ is the gyromagnetic ratio, α is the damping constant and H_{eff} is the effective field. The simulations that have been reported in this thesis can be broadly classified into the following sub-categories and have been elaborated therein.

2.6.1. Ferromagnetic resonance (FMR) simulations

FMR simulations for understanding the dependence of magnetization trajectories on perpendicular magnetic anisotropy were performed on samples of dimensions $100 \text{ nm} \times 100 \text{ nm} \times 1 \text{ nm}$. The saturation magnetization is taken as $\mu_0 M_s = 1500 \text{ mT}$. to match the M_s obtained for our multilayers (see Chapter 3). Additionally, the samples were assumed to be single domain ferromagnetic elements with damping constant $\alpha = 0.02$. Such a damping constant is chosen to match the damping constant values of our multilayer structures with similar CoFeB thicknesses and is close to that reported in literature. The perpendicular magnetic anisotropy during these simulations was varied from 0 to 1500 mT. FMR in the frequency sweep mode, was excited by applying a fixed static external field on the sample as the frequency of a microwave field was swept. The frequency of the rf-magnetic field is typically varied from 1 to 20 GHz in steps of 0.2 GHz. For exciting FMR in the field sweep mode, a microwave field of fixed frequency was applied in the sample while the field was swept. The analysis of the obtained simulation data will be explained in Chapter 5.

2.6.2. Magnetization switching simulations

Simulations were performed on samples of dimensions $100 \text{ nm} \times 100 \text{ nm} \times 1 \text{ nm}$. The saturation magnetization was kept fixed at $\mu_0 M_s = 1500 \text{ mT}$. The second order PMA energy corresponding to H_p is varied from $K_{u,2} = 1.0 \times 10^3 \text{ kJm}^{-3}$ to $1.8 \times 10^3 \text{ kJm}^{-3}$, while the fourth order PMA $K_{u,4}$ corresponding to $H_{p,2}$ is changed from 0 to $-4 \times 10^2 \text{ kJm}^{-3}$. Based on the demagnetizing field of the sample and a competition between the second and fourth order PMA terms, the samples relaxed to one of the in-plane, perpendicular or easy cone states. After entering these values, the samples were allowed to relax to its equilibrium condition. The equilibrium state or the easy axis is defined as the magnetization state after a time t when the change in unit magnetization vector Δm becomes less than 10^{-6} .

After estimating the easy axes, magnetization switching simulations were performed in order to understand the electric-field controlled switching of easy cone magnetized samples. The electric field effect can be modelled as a change in H_{eff} due to the presence of a z-axial field pulse H_z which is equivalent to the change in PMA in presence of an interfacial voltage. Before applying H_z , we apply a small bias field of 1 mT along x-axis to ensure that azimuthal angle $\phi = 0$ degree and let the sample relax to its equilibrium state which is determined by its effective anisotropy energy, as described in the previous section. Subsequently, a z-axial magnetic field pulse with a fixed duration of 10 ns and rise and fall times of 0.1 ns is applied at $t = 0$ ns and the resultant magnetization trajectory is observed. Switching condition of the samples are studied by varying the field pulse amplitudes. Switching time t_{swit} is taken as the time when the z-component of magnetization m_z crosses the equator defined by $m_z = 0$. H_{s0} , which is defined as the minimum amplitude of H_z required for switching the magnetization vector, was estimated as a function of PMA.

Section 2.7. COMSOL Multiphysics simulations

In order to understand the field distributions when microwave voltage is applied to our CoFeB junction, we calculated the Oersted field distribution in our devices by using the finite element method (FEM) with COMSOL Multiphysics simulator [2]. The main use of these simulations was for the analysis of the angular dependence of rectified voltages arising from the electric-field induced spin pumping measurements as will be discussed in Chapter 4. Although the actual experimental devices we fabricated using a Ta(5nm)/Ru(10nm)/Ta(5nm) buffer layer, for simplicity in the simulations, the entire buffer layer has been taken in the form of a single heavy metal layer of 20 nm Ta. The resistivity values were taken from the literature. The mesh grids were taken as triangular elements with a dimension of about 10 nm on a side after consulting the literature. However, such a mesh dimension depends on the size of samples studied. For example, while 10 nm mesh grids are necessary to get continuity in the field distributions while studying a $.1 \times 1 \mu\text{m}^2$ sample, higher mesh sizes could be successfully used when the sample sizes are increased. The top surface is taken as the input port and the bottom is grounded. The sample sides are insulated.

The input microwave signal of frequency f is applied on the upper Al_2O_3 surface while the bottom Ta surface is grounded. The applied power is scaled according to the simulated and the actual device size ratio. For example, while simulating the field distributions of an actual device of size $20 \mu\text{m} \times 200 \mu\text{m}$, we used a sample size of $0.1 \times 1 \mu\text{m}^2$. If the applied power during measurement is 100 mW, the simulations were performed at a power of 10 μW because the calculated sample size is 10^4 times smaller than the actual device. The COMSOL simulations were performed for a range of frequencies upto 20 GHz and input power that ranged from 0.1 μW to 1 W. Such a wide range of simulations are necessary to obtain conclusive results that can explain the field distributions in our devices.

References:

1. LLG Micromagnetics developed by M.R. Sheinfein and E.A. Price.
2. COMSOL Multiphysics Reference Manual, version 5.3, COMSOL, Inc, www.comsol.com
3. A. Deka, B. Rana, R. Anami, K. Miura, H. Takahashi, Y. Otani and Y. Fukuma; *Physical Review B* 101, 174405 (2020).
4. A. Deka, I. Tanaka, J. Mohan and Y. Fukuma; *IEEE Transactions on Magnetics* (2020).
5. A. Deka, K. Sato, I. Tanaka and Y. Fukuma; *IEEE Transactions on Magnetics* 56, 3 (2020).

Chapter 3

Control of interfacial magnetic anisotropy in CoFeB/MgO junctions using magnetic annealing

3.1. Introduction

Ferromagnetic materials exhibit a property wherein they tend to magnetize favorably in specific orientations. Such a property is called magnetic anisotropy, which has evolved to be of significant technological relevance in terms of spintronic device applications [1]. Magnetic anisotropy can be classified into magnetocrystalline anisotropy (MCA) which refers to the anisotropy based on crystallographic orientation and the shape anisotropy that arises due to the shape of the ferromagnet. Broadly speaking, magnetic anisotropy energy (MAE) has effects on the thermal stability and switching of the free layer of a magnetic tunnel junction to precession cone angles that determine spin pumping, spin wave excitation and nano-oscillator microwave emission efficiency [2-3]. Magnetic anisotropy, in general, has two major origins: (a) the dipole-dipole interactions and (b) spin-orbit coupling (SOC) [4].

The effect of magnetic dipolar interactions on MCA is negligible compared to the SOC. One of the most commonly observed consequence of dipolar interactions is the shape anisotropy in ferromagnetic thin films [4]. The dipole-dipole interactions give rise to the demagnetizing fields in ferromagnetic thin films that arises perpendicular to the thin film plane. This is a consequence of the reduced dimension along the growth direction of thin films as a result of which the dipole-dipole interactions are higher perpendicular to the film plane compared to the lateral directions. Typically, the demagnetizing field in a ferromagnet is given by $H_d = n_x M_x + n_y M_y + n_z M_z$ [5]. For thin films $n_x = n_y = 0$ and $n_z = 1$, due to which demagnetizing fields become equal to the saturation magnetization i.e. $H_d = M_s$. However, it should be noted that in nanostructures where the lateral dimensions are comparable to

the thicknesses, we can have $n_x \neq 0$, $n_y \neq 0$ and $n_z < 1$. In terms of device applications, such a phenomenon is still widely exploited in device designs to give rise to shape magnetic anisotropies by controlling the device dimensions [6].

SOC in ferromagnetic materials is the dominant origin of MCA. Such an effect indicates that the MAE is related to the crystal lattice because magnetic moments are coupled to the lattice via SOC. Typically, in cubic crystals (e.g. CoFeB), such an anisotropy is estimated to be negligible because of the symmetric ordering. However, as far back as in 1954, Neel proposed the concept of interfacial MCA (iMCA) arising due to SOC from the reduced symmetry of magnetic atoms at the interfaces i.e. interfacial magnetic anisotropy [7]. Such an interfacial anisotropy has become particularly important as we aim for higher density in memory and logic chips in ultrathin magnetic films, because perpendicular anisotropy materials have faster switching times and require lower switching currents [8,9].

Interfacial SOC is the origin for the second order PMA H_p in technologically relevant materials like CoFeB/MgO junctions, as discussed earlier in Chapter 1. More specifically, PMA in CoFeB/MgO junctions arises at the interface due to a hybridization between the $3d$ orbitals of the ferromagnetic atoms (Co and Fe) with the $2p$ orbitals of O at the interface [10]. Although both Co and Fe atoms have a possibility of bonding with the O atoms, theoretical studies predict that this hybridization is stronger for Fe compared to the Co atoms [11]. The resulting anisotropy field typically acts perpendicular to the film plane and therefore acts in a way to reduce the effective H_d . The effective demagnetizing field $H_{d,eff}$ then becomes $H_d - H_p$. PMA of CoFeB/MgO junctions which originates from the interfacial SOC, increases with a decrease in thickness of the CoFeB thin films and can be large enough to overcome the H_d [9-11]. Such a condition results in the shift of the in-plane easy axis of the ferromagnetic thin film junction into a perpendicular easy axis because the MAE becomes lower along the perpendicular direction to the film plane, as schematically shown in Fig. 3.1. The PMA in CoFeB/MgO junctions was recently demonstrated to be large enough to fabricate magnetic tunnel junctions that have both the free and fixed layers with perpendicular easy axis [15]. It was also shown in the same paper that PMA in

CoFeB/MgO junctions can be high enough to obtain a thermal stability factor of $\Delta \sim 40$ for devices with diameter less than 50 nm. Δ is a figure of merit for storage devices given by the relation $\frac{M_s H_{d,eff} V}{k_B T}$, where V is the volume of the device, k_B is the Boltzmann's constant and T is the temperature of operation. It can be seen that with a decrease in the device dimensions, higher value of $H_{d,eff}$ is required in order to maintain the thermal stability required for memory retention. It should be mentioned here that apart from H_p , a higher order PMA $H_{p,2}$, that arises from the 4th order PMA energy, is also found in CoFeB/MgO junctions. Although the exact origin is not known for $H_{p,2}$, theoretical investigations indicate that it might arise from interfacial inhomogeneties [18]. The overall PMA energy due to the presence of H_p and $H_{p,2}$ can be written as $E(\theta) = -K_{u,2} \cos^2 \theta - K_{u,4} \cos^4 \theta$ where, $K_{u,2}$ and $K_{u,4}$ are energies corresponding to H_p and $H_{p,2}$. But such a higher order PMA energy $K_{u,4}$ is found to be negligible in our samples. In addition, although 2nd order PMA can be modulated using electric-fields, $H_{p,2}$ cannot be controlled using voltages [10,11]. Given the purpose of our studies in this thesis, we focus only on the voltage controllable part of PMA i.e. H_p . In the following part of this thesis, PMA would unambiguously refer to the 2nd order perpendicular anisotropy, unless specifically mentioned otherwise.

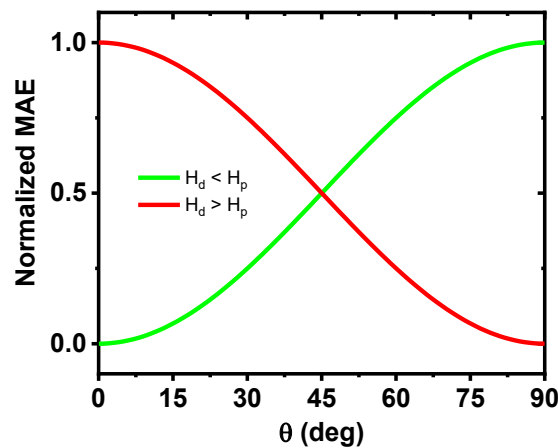


Figure 3.1 Schematic to illustrate the normalized magnetic anisotropy energy (MAE) as a function of the angle of the magnetization from the film normal θ for a thin film with an in-plane (red) and perpendicular (green) easy axes.

The saturation magnetization and magnetic anisotropies are always temperature dependent. Using a classical picture, a lattice site can be understood to be surrounded by other magnetic atoms with a short-range magnetic order. The origin of a temperature dependence can be understood to arise from thermal fluctuations of the local magnetizations of such regions. Using this assumption, Bloch derived the temperature dependence of saturation magnetization of a ferromagnet to follow

$$M_s(T) = M_s(0) \left(1 - \left(\frac{T}{T_C} \right)^\chi \right),$$

where T_C is the Curie temperature of the ferromagnet and the Bloch's coefficient $\chi = 1.5$ [19]. Subsequently, it was shown by Callen and Callen that the magnetic anisotropy

follows a power law of magnetization and is given by $\frac{K_{u\perp}(T)}{K_{u\perp}(0)} = \left(\frac{M_s(T)}{M_s(0)} \right)^\gamma$, where K_u is the magnetic

anisotropy energy and γ is a scaling exponent [20]. Although these relations have been proven to be valid in a wide range of ferromagnetic systems, recent experimental and theoretical advances in our understanding of magnetic properties in ultrathin films, have enabled us to observe that the temperature dependences of bulk and interfacial anisotropies have different temperature dependences. As will be discussed in Sec. 3.5 in detail, such a difference in the temperature dependences can be used as a tool to identify the origins of magnetic anisotropy fields in our CoFeB/MgO junctions.

In this chapter, we first establish the method used for estimation of in-plane and perpendicular magnetic anisotropy fields. Since the crystalline structure of a ferromagnet can be modified by temperature, we subsequently explain the effect of annealing on magnetization and anisotropy fields. Finally, we discuss the temperature dependence of saturation magnetization and anisotropy fields in ultrathin CoFeB films. The conclusions drawn from the experiments performed in this chapter will be used subsequently for our studies on electric-field induced magnetization dynamics.

3.2. Estimation of magnetic anisotropy fields using in-plane angular dependence of ferromagnetic resonance fields.

Given the importance of magnetic anisotropy of ferromagnetic systems, it is of utmost importance for us to first devise a method to accurately estimate the magnetic anisotropy fields. One of the more common methods to estimate in-plane H_k and perpendicular magnetic anisotropy fields H_p is from the fitting of the frequency f dependent resonance fields H_{res} to the Kittel formula given below:

$$f = \gamma \sqrt{(H_{res} + H_k - M_{eff})(H_{res} + H_k)}, \quad (3.1)$$

where γ is the gyromagnetic ratio and the effective demagnetizing field $M_{eff} = M_s - H_p$.

Due to the high value of H_p at lower CoFeB thicknesses, the M_{eff} in the above formula can vary from 1500 mT in CoFeB(20 nm)/MgO junctions to close to 0 mT in CoFeB(1.5 nm)/MgO junctions. This results in a high degree of error in estimating the in-plane anisotropy fields in CoFeB/MgO junctions, which are typically found to be of the order 10^0 mT.

One of the other techniques to estimate magnetic anisotropy fields is by solving the Smit-Beljers relation [21] for a specific magnetic system, using which we can estimate the relationship between a resonant magnetic field of FMR and an azimuthal angle of the magnetization for an in-plane magnetized film. Let us consider that the direction of the magnetization M and external magnetic field H_{ex} is given by (ϕ, θ) and (α, β) , respectively, where α and ϕ are the azimuthal angles and β and θ are the elevation angles from the film plane as schematically shown in Fig. 3.2.

The Smit Beljers relation in this ferromagnetic system is given as follows:

$$\left(\frac{f}{\gamma}\right)^2 = [M_s \cos\theta]^2 \left(\frac{\partial^2 F}{\partial \theta^2} \frac{\partial^2 F}{\partial \phi^2} - \left(\frac{\partial^2 F}{\partial \theta \partial \phi} \right)^2 \right), \quad (3.2)$$

where f is the frequency and γ is the gyromagnetic ratio.

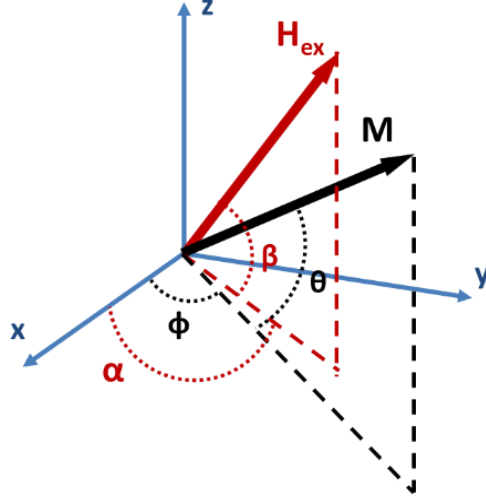


Figure 3.2: The elevation angle and azimuthal angle of M and H_{ex} are (θ, ϕ) and (β, α) respectively. The equations are derived for the case where M is parallel to H_{ex} in the film plane.

The magnetic free energy F can be expressed as a sum of the Zeeman energy, demagnetization energy and magnetic anisotropy energy as below:

$$F = \frac{\mu_0 M_s}{2} \begin{bmatrix} -2H_{ex} (\cos \theta \cos \beta \cos(\alpha - \phi) + \sin \theta \sin \beta) + (M_s - H_p) \sin^2 \theta \\ -H_k \cos^2 \phi \cos^2 \theta \end{bmatrix}, \quad (3.3)$$

where H_k is the in-plane anisotropy field directed along $\phi = \theta = 0^\circ$, H_p is the perpendicular magnetic anisotropy field along $\theta = 90^\circ$.

We can obtain the free energy differentials with respect to ϕ and θ as below:

$$\frac{\partial^2 F}{\partial \theta^2} = \mu_0 M_s \begin{bmatrix} -H_{ex} (-\sin \theta \sin \beta - \cos \beta \cos(\alpha - \phi) \cos \theta) - (M_s - H_p) \cos 2\theta \\ -H_k \cos^2 \phi \sin 2\theta \end{bmatrix}, \quad (3.4)$$

$$\frac{\partial^2 F}{\partial \phi^2} = \mu_0 M_s \left[H_{ex} (\cos \theta \cos \beta \cos(\alpha - \phi)) + H_k \cos^2 \theta \cos 2\phi \right], \quad (3.5)$$

$$\frac{\partial^2 F}{\partial \theta \partial \phi} = -\mu_0 M_s \left[H_{ex} (\sin \theta \cos \beta \sin(\alpha - \phi)) + \frac{H_k}{2} \sin 2\theta \sin 2\phi \right]. \quad (3.6)$$

For the estimation of H_p and H_k , FMR measurements were performed for in-plane magnetized films in the condition that M is parallel to H_{ex} . Using $\theta = \beta = 0^\circ$ and $\phi = \alpha$ in Eq. (3.4) ~ Eq. (3.6) and substituting the resulting expressions in Eq. (3.2), we obtain:

$$\left(\frac{f}{\gamma}\right)^2 = \frac{1}{M_s^2} \left((\mu_0 M_s H_{ex} + \mu_0 M_s (M_s - H_p) + \mu_0 M_s H_k \cos^2 \phi) (\mu_0 M_s H_{ex} + \mu_0 M_s H_k \cos 2\phi) \right). \quad (3.7)$$

Replacing H_{ex} with the term of resonant magnetic field H_{res} in Eq. (3.7), we obtain the relation between H_{res} and ϕ for estimating the values of H_p and H_k as below:

$$H_{res} = -H_k + \frac{3}{2} H_k \sin^2 \phi - \frac{(M_s - H_p)}{2} + \frac{1}{2} \left[\frac{H_k^2 \sin^4 \phi + (M_s - H_p)^2 + 2(M_s - H_p)H_k \sin^2 \phi}{+ 4 \left(\frac{f}{\mu_0 \gamma} \right)^2} \right]^{\frac{1}{2}}. \quad (3.8)$$

The advantage of this equation over the standard form of Kittel equation is that it poses an additional constraint in terms of ϕ . This reduces the error in determination of H_k which is typically of the order few mT. It is unlike H_p which is of the order $\sim 10^3$ mT for the range of thin films used in experiments performed for our study.

3.3. Annealing temperature dependence of saturation magnetization.

One of the characteristic magnetic properties of ferromagnetic materials is its saturation magnetization. As mentioned earlier in Sec. 3.1, it becomes especially important while studying magnetic anisotropies because M_s also determines the strength of demagnetizing fields of ferromagnetic thin films. The magnetization is strongly dependent on the kind of magnetic atoms that are present in the ferromagnetic material because it is determined by the isotropic exchange interactions between the magnetic atoms in the ferromagnet. Therefore, it can vary strongly depending on the composition of the ferromagnet. Throughout the entire thesis, we have used CoFeB thin films with a fixed composition ratio of Co:Fe:B as 20% : 60% : 20%, which are grown on top of a Ta/Ru/Ta underlayer as mentioned in Chapter 2. However, during to the process of annealing, it has been reported that B atoms tend to migrate into the Ta layer as it has an affinity towards Ta [13]. This might affect the saturation magnetization because reduction of B in the alloy could lead to a change in the composition of CoFeB [13,14].

Therefore, we estimated the M_s values of our samples as a function of the annealing temperature using superconducting quantum interference device (SQUID). A typical signal obtained from the SQUID measurement with the external field in the in-plane and perpendicular directions is shown in Fig. 3.3a and 3.3b respectively. The obtained magnetic moments are the sum of magnetizations of all the magnetic materials present in the multilayers namely, paramagnetic SiO_2 and ferromagnetic CoFeB. The magnetization vs magnetic field ($M-H$) plot of ferromagnetic CoFeB is extracted by subtracting the magnetization of SiO_2 from this signal, followed by dividing the magnetization with the volume of the ferromagnetic layer in the multilayer. Typical example of a refined signal after we subtract the paramagnetic signal from Fig. 3.3a and 3.3b is shown in Fig. 3.3c. It shows that the sample has an easy axis in the film plane as it is easier to magnetize the sample in the film plane compared to the perpendicular direction.

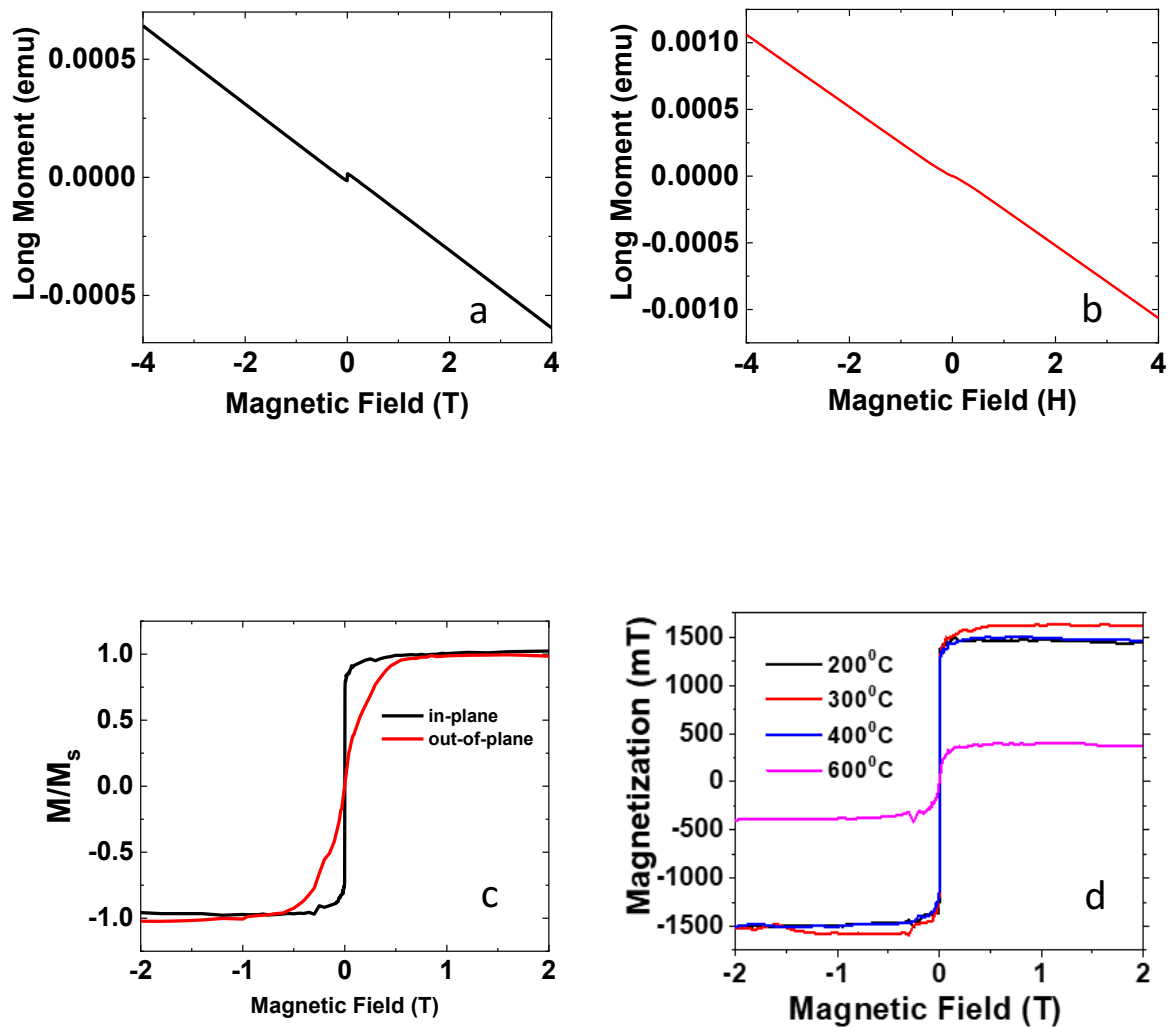


Figure 3.3 Magnetic moments obtained from SQUID measurements when the external magnetic field is applied in the **a**, in-plane and **b**, out-of-plane directions on the multilayer. **c**, Magnetization versus magnetic field ($M-H$) plots extracted from **a** and **b** after subtracting the paramagnetic signal are plotted together to show the magnetic easy axis in our samples. **d**, Magnetization vs in-plane field data are presented for multilayers with 2.0 nm thick CoFeB layers annealed at temperatures ranging from 200 °C to 600 °C. All the multilayer stacks in these figures have 2.0 nm thick CoFeB layers.

It should be noted that although SQUID is an excellent tool to measure magnetization, it is tough to extract accurate information about magnetic anisotropy in the samples. This is because our multilayers are grown on paramagnetic Si/SiO₂ substrates which gives rise to an additional background in addition to the signal obtained from the ferromagnetic layer. Typically, the field at which the magnetization saturates in the ferromagnetic hard axis gives us a measure of the effective demagnetizing field $H_{d,eff}$ in the sample and hence the perpendicular anisotropy field ($H_p = M_s - H_{d,eff}$). But because we need to subtract the paramagnetic signal in our samples, the accuracy of the field at which the magnetization saturates is not well defined. In addition, as mentioned in the previous section, the in-plane magnetic anisotropy for our samples are much less compared to H_p . Therefore, we need an alternative technique to estimate magnetic anisotropy accurately. A direct measurement technique is desirable that detects the ferromagnetic properties as a function of fields (instead of voltages that depend on magnetic flux in SQUID measurements). Such a condition is fulfilled by the ferromagnetic resonance measurements.

Nevertheless, we can extract the saturation magnetization of our samples to a good degree of accuracy from these measurements. Typical annealing temperature dependence of the $M-H$ plots for multilayers with a 2-nm-thick CoFeB layer is shown in Fig. 3.3d. Based on this measurement, we see that the M_s is roughly constant at 1500 mT for our thin films in the annealing range of 100 °C – 400 °C. At higher annealing temperatures like 600 °C, M_s reduces drastically. Such a drastic reduction of M_s at high annealing temperatures is due to the intermixing of the ferromagnetic and oxide layers [14]. A similar behavior of saturation magnetization is obtained for films with 5 nm CoFeB layers.

3.4. Estimation of magnetic anisotropy using ferromagnetic resonance.

In this section, the effect of annealing the CoFeB/MgO junctions in the presence of a bias magnetic field H_b on magnetic anisotropy will be discussed. Magnetic anisotropy of ferromagnetic thin films has been shown to be strongly enhanced by annealing conditions [13,22,23]. Temperature treatment enhances the crystallinity of CoFeB/MgO junctions that leads to an improvement in the lattice matching between the CoFeB/MgO layers. This strengthens the hybridization between Co (Fe) atoms in the ferromagnetic layer with the interfacial O atoms of the MgO layer. Since PMA originates from such a hybridization, it can be controlled by changing the annealing temperature as has been observed in several recent studies [13,14]. In addition, annealing in the presence of H_b has been shown to induce an anisotropy field along H_b [24-26], which is the main purpose of this section.

The magnetic anisotropy fields are estimated by ferromagnetic resonance (FMR) spectroscopic studies that is performed using a vector network analyzer (VNA) as discussed in the Chapter 2. An example of the real and imaginary parts of the S_{11} parameter recorded in the VNA based FMR measurement is shown along with the setup in Fig. 3.4a. The obtained data are fitted by:

$$S_{11} = \frac{L \times dH^2}{(H_{ex} - H_{res})^2 + dH^2} + \frac{D \times dH \times (H_{ex} - H_{res})}{(H_{ex} - H_{res})^2 + dH^2} + a \times H_{ex} + b, \quad (3.9)$$

where L and D are the weights of the Lorentzian and dispersive parts, respectively, dH is the half width at half maximum, a and b are constants. By fitting the data using Eq. 3.9, we can obtain the values of $H_{res} = 137.2$ mT and $dH = 3.6$ mT. We measured the FMR spectra as a function of the azimuthal angle to obtain the resonance fields. Figure 3.4b shows the azimuthal angle dependence of resonance fields for multilayers with a 2-nm-thick CoFeB layer prior to annealing. A sinusoidal behavior indicates the presence of an in-plane magnetic anisotropy IMA, in addition to PMA. Upon fitting the data using Eq. 3.8, we obtain $\mu_0 H_k$ as 1.2 mT while $\mu_0 H_p$ is estimated to be 966 mT. An *inherent* IMA typically appears in random directions during the deposition process. Magnetic annealing allows us to define the direction of IMA as will be discussed in the next paragraph.

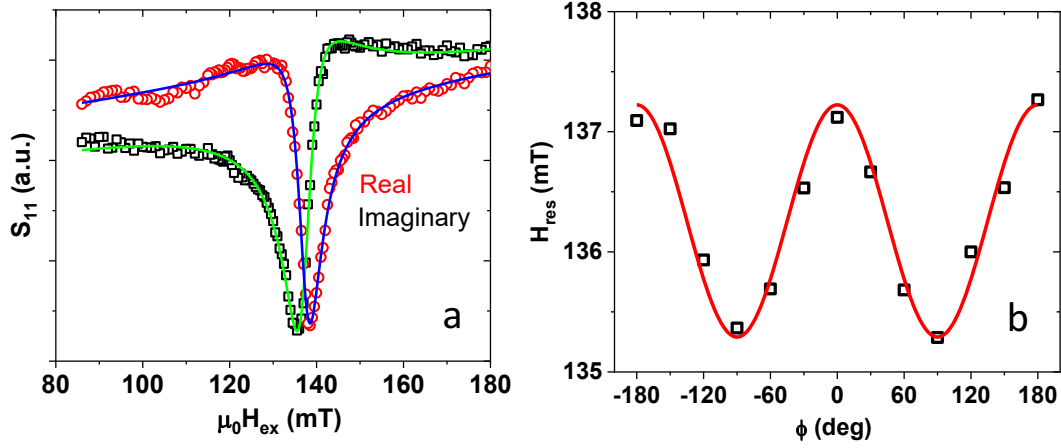


Figure 3.4a, A typical FMR spectra is shown that consists of imaginary and real parts of reflection parameter S_{11} (symbols) with fits (lines) to Eq. (3.9). **b**, In-plane angle ϕ dependence of the resonant field H_{res} (squares) at frequency $f = 9.0$ GHz for a multilayer with a 2.0-nm thick CoFeB layer prior to annealing. Line is fit using Eq. (3.8).

The bias magnetic field H_b applied during annealing is applied in three orthogonal directions to the multilayers as discussed in Chapter 2. Using Fig. 3.5, we discuss the effect of magnetic annealing in case of a multilayer with a 2-nm-thick CoFeB layer. When the film is annealed in the presence of H_b in an in-plane direction which is perpendicular to the *inherent* in-plane magnetic anisotropy (x-axis), we observe minima along $\phi = 0$ degree in the H_{res} vs ϕ plots as shown by the red symbols. On the other hand, if we anneal the film with H_b parallel to the *inherent* anisotropy of the films (y-axis), we can see a 90 degree phase difference between x- and y-axial annealing, accompanied by an increase in the sinusoidal amplitude. Meanwhile, if we anneal the film with H_b perpendicular to the sample plane (z-axis), the amplitude of the sinusoidal behavior for H_{res} vs ϕ is clearly suppressed (blue). Upon fitting the experimental data in Fig. 3.5b using Eq. 3.8, we can obtain $\mu_0 H_k$ and $\mu_0 H_p$ as 1.3 and 1083 mT, 1.8 and 1088 mT, 0.4 and 1096 mT for the x-, y-, z-axis magnetic annealing, respectively. The small in-plane component for perpendicular H_b and the different magnitude of the anisotropy field between x- and y- axis magnetic fields may be due to the misalignment in the experimental setup during annealing.

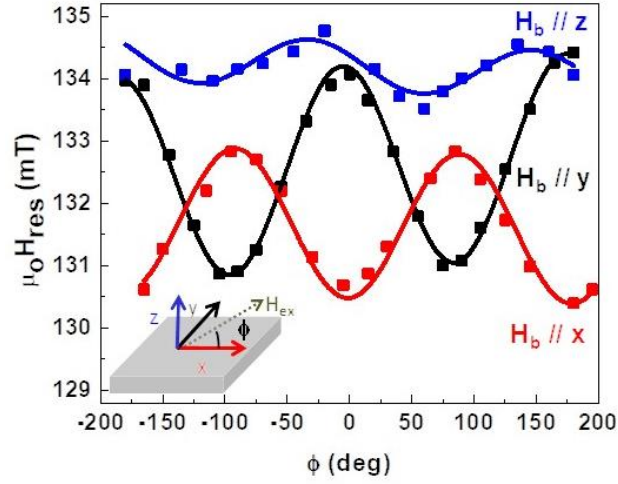


Figure 3.5: In-plane angle ϕ dependence of the resonant field H_{res} (squares) at frequency $f = 8.0$ GHz for a 2.0-nm thick CoFeB layer annealed at 200 °C in presence of a magnetic field H_b in three orthogonal directions (arrows of corresponding color on the block in inset). Lines are fits to Eq. (3.8).

In order to see the effect of annealing temperature on magnetic anisotropies, we measure the H_k and H_p as shown in Fig. 3.6a and 3.6b, respectively, for different CoFeB thicknesses of 1.5 nm, 1.8 nm and 2.0 nm. Please note that H_k in all the samples were induced by annealing. It is observed that H_k for all the thicknesses decrease with increasing annealing temperature. On the other hand, H_p increases with increasing annealing temperature, reaching to a maximum at around 300 °C, and then drastically decreases with the further increment of annealing temperature because of intermixing of the interface, as reported in previous studies.

There have been many experimental and theoretical studies on IMA induced by magnetic annealing for bulk samples [24-26]. The easy axis of the IMA is parallel to the direction of an external magnetic field during annealing. One plausible model to explain its mechanism in a cubic lattice such as NiFe and CoFe is directional ordering of atomic pairs: in alloys consisting of A and B atoms, an anisotropic distribution of different atom pairs such as AA, BB and AB yields a uniaxial anisotropy [5, 24-26]. In this study, H_k decreases with increasing annealing temperature because migration of atoms

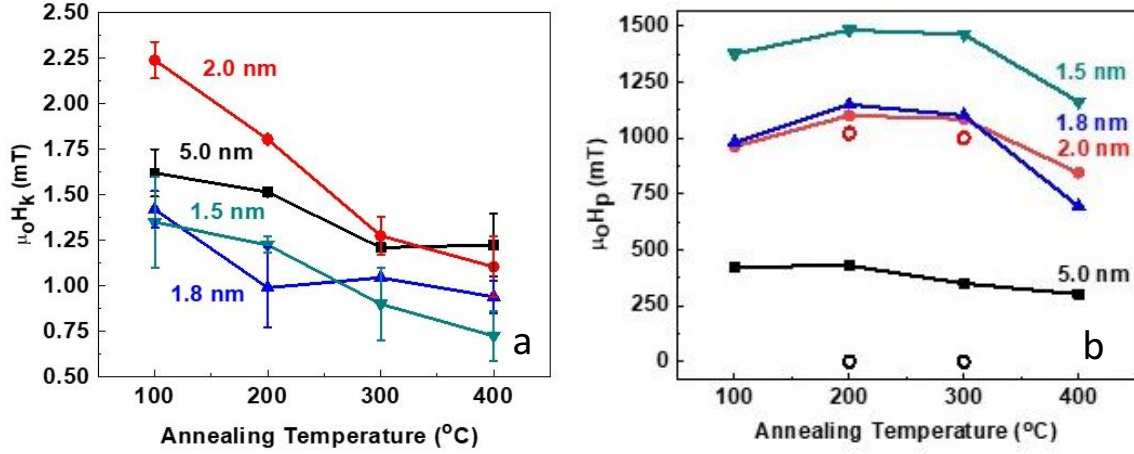


Figure 3.6a, In-plane magnetic anisotropy field H_k plotted (solid symbols) as a function of annealing temperature for CoFeB layers with thicknesses ranging from 1.5 nm to 2.0 nm. **b**, Corresponding perpendicular magnetic anisotropy H_p for the samples (solid symbols) measured from FMR measurements. Error bars represent the maximum deviation of the anisotropy fields obtained for different frequencies from the average value. H_p from SQUID measurements for multilayers with 2 nm and 5 nm thick CoFeB layers is shown as red and black circles respectively.

causes an isotropic distribution of atom pairs among Co, Fe and B. Higher temperature annealing leads to improved crystallinity as well as atomic order at CoFeB/MgO interface, and therefore H_p is enhanced.

It should be mentioned here that we have also measured the PMA of a multilayer stack that has a 5 nm CoFeB layer using SQUID and FMR. While the in-plane and perpendicular MH measurements give us $H_p = 0$ mT, FMR measurements gives us a value of $H_p \sim 500$ mT as shown in Fig. 3.6b. Although we mentioned that estimation of PMA from SQUID is not accurate due to reasons discussed previously, we note that such a high deviation from the FMR measurements cannot be expected. This can be understood from the comparable PMA obtained from FMR and SQUID measurements for 2 nm data in Fig. 3.6b. Although we do not know the precise reason for such a large deviation in the 5nm thick CoFeB films, we believe it could be due to measurement errors in the SQUID setup or non-uniformity of microwave during FMR measurements. Therefore, we have not considered the data for thicker films in our discussion. Nonetheless, H_k shows similar annealing temperature behavior as the rest of the films.

3.5. Temperature dependence of saturation magnetization and magnetic anisotropy

The temperature dependence of saturation magnetization $M_s(T)$ was measured using SQUID. The temperature dependent magnetization measurements were performed at a low magnetic field of 5 mT so as to minimize the paramagnetic contribution from SiO_2 . Owing to the low in-plane magnetic field required to saturate the multilayer stack with a 2.0-nm-thick CoFeB layer (see Fig. 3.3), the obtained magnetization can be attributed entirely to the ferromagnet. The corresponding data for the 2.0-nm-thick CoFeB layer annealed at 200 °C is shown in Fig. 3.7a. The monotonic change with respect to temperature implies that the annealing process does not give rise to any oxide interlayer in the CoFeB/MgO junctions [27]. A decrease in the saturation magnetization at higher temperatures is due to the increment of thermal fluctuations and excitation of spin wave modes that tends to destabilize the orientation of magnetic moments. The experimental data were fitted using the Bloch's law given below [19]:

$$M_s(T) = M_s(0) \left(1 - \left(\frac{T}{T_C} \right)^\chi \right), \quad (3.10)$$

where T_C is the Curie temperature and χ is the Bloch's exponent. In the empirical form of Bloch's law, the interactions between the excited spin wave modes was not considered and therefore $\chi = 1.5$ was obtained. In the low temperature range upto $T = 50$ K, the experimental data fits well to the Bloch's law using $T_C = 1150$ K and $\chi = 1.5$ as shown by the green line in Fig. 3.7. The data in the measurement range of 50 K to 300 K was fitted to the Bloch's law using $T_C = 1150$ K and $\chi = 1.8$ as shown by the red line in the same figure. Although such an assumption holds well for low temperatures, at higher temperatures the spin waves might also interact among themselves [28]. Thus, a difference in the exponents between lower and higher measurement temperatures can be expected due to the magnon-magnon scattering. We have also measured the data for multilayers with 5.0 nm CoFeB layers as shown in Fig. 3.7b. Upon fitting the data using Eq. (3.10), for $T < 50$ K, we obtain $\chi = 1.6$ while in higher temperatures $T > 50$, we obtain a much higher value of $\chi = 2.5$.

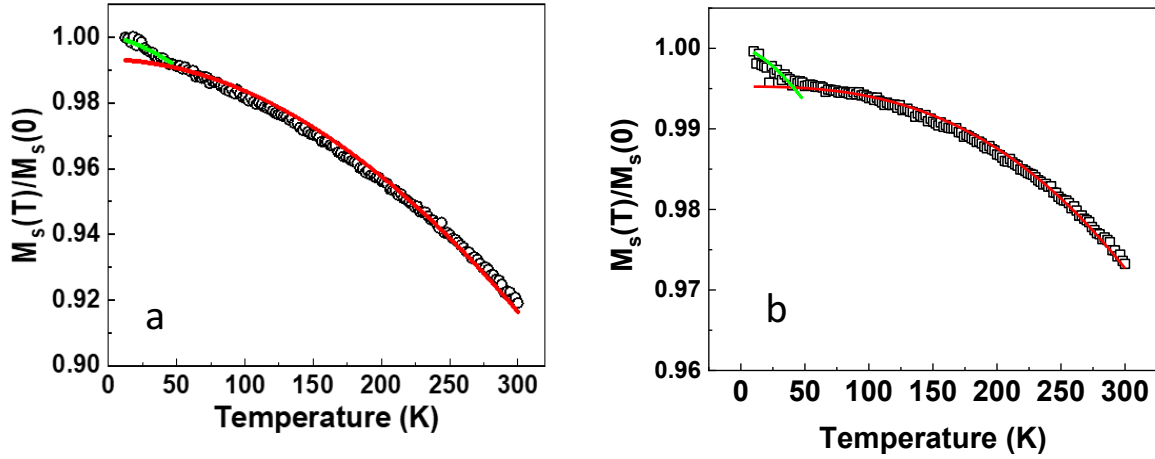


Figure 3.7a, Saturation magnetization M_s as a function of temperature. Upon fitting using Bloch's law (Eq. (3.10)), $T_C = 1150$ K and $\chi = 1.5$ is obtained for $T < 50$ K (green line) and $T_C = 1150$ K and $\chi = 1.8$ for $T > 50$ K (red line). **b**, The corresponding data for a multilayer with 5.0 nm thick CoFeB layer. We obtain $\chi = 1.6$ and 2.5 in low and high temperatures respectively (by fixing $T_C = 1150$ K during fitting) indicating a higher deviation from the Bloch's law.

The temperature dependence of anisotropy fields, H_p and H_k , of the corresponding sample were estimated using temperature dependent FMR measurements. Both H_p and H_k are found to be increased monotonically with decreasing temperature as shown in Fig. 3.8a. Figure 3.8b shows the temperature dependence of the corresponding magnetic anisotropy energies. Since the dominant contribution to PMA in CoFeB/MgO junctions comes from the interface between the two layers, we can approximately equate K_i/t , K_i being the interfacial PMA, to the energy corresponding to the PMA field

$$K_{u\perp}(T) = \frac{M_s(T)H_p(T)}{2}.$$

The experimental data are then fitted to the Callen-Callen power law of the magnetization [20]

which can be written as:

$$\frac{K_{u\perp}(T)}{K_{u\perp}(0)} = \left(\frac{M_s(T)}{M_s(0)} \right)^\gamma, \quad (3.11)$$

using scaling exponent $\gamma = 2.1$. According to the Callen-Callen model, the anisotropy energy scales as a function of temperature with $\gamma = 3$ for a ferromagnet, which has a single site origin of magnetic anisotropy. However, a scaling exponent of $\gamma \sim 2$ has been observed in VCMA systems with interfacial magnetic anisotropies like Ta/CoFeB/MgO [29,30] and Ru/Co₂FeAl/MgO [31]. Such a deviation from the Callen-Callen model is due to the presence of interfacial hybridization between the $3d$ orbitals of Fe and $2p$ orbitals of O atoms in the CoFeB/MgO junction. Callen-Callen law is derived assuming a uniform exchange interaction in the ferromagnet i.e. the x-, y- and z-components of the exchange interaction matrix are equal. Based on this model, it was shown using simulations that interfacial magnetic anisotropy scales as a power law of magnetization with an exponent of 3. However, due to the presence of interfacial hybridization in CoFeB/MgO junctions, the exchange interactions vary between the in-plane and perpendicular orientations. Due to this, simulations show that the exponent is lowered from 3 to 2.

Upon estimating the energy corresponding to IMA $K_{u//}$ using a similar relation, as shown in Fig. 3.8(b), we are able to fit the temperature dependence of the anisotropy energies to the power law of magnetization using $\gamma = 2.3$. We have measured the temperature dependences for different thicknesses as well. Similar dependence of PMA and IMA has been obtained for the films that have CoFeB layer with thickness close to 2.0 nm. Such a behavior has been shown in Fig. 3.8 using the data for a multilayer 2.2 nm thick CoFeB layer. This indicates that, in addition to PMA, even IMA can have interfacial origin in CoFeB/MgO junctions.

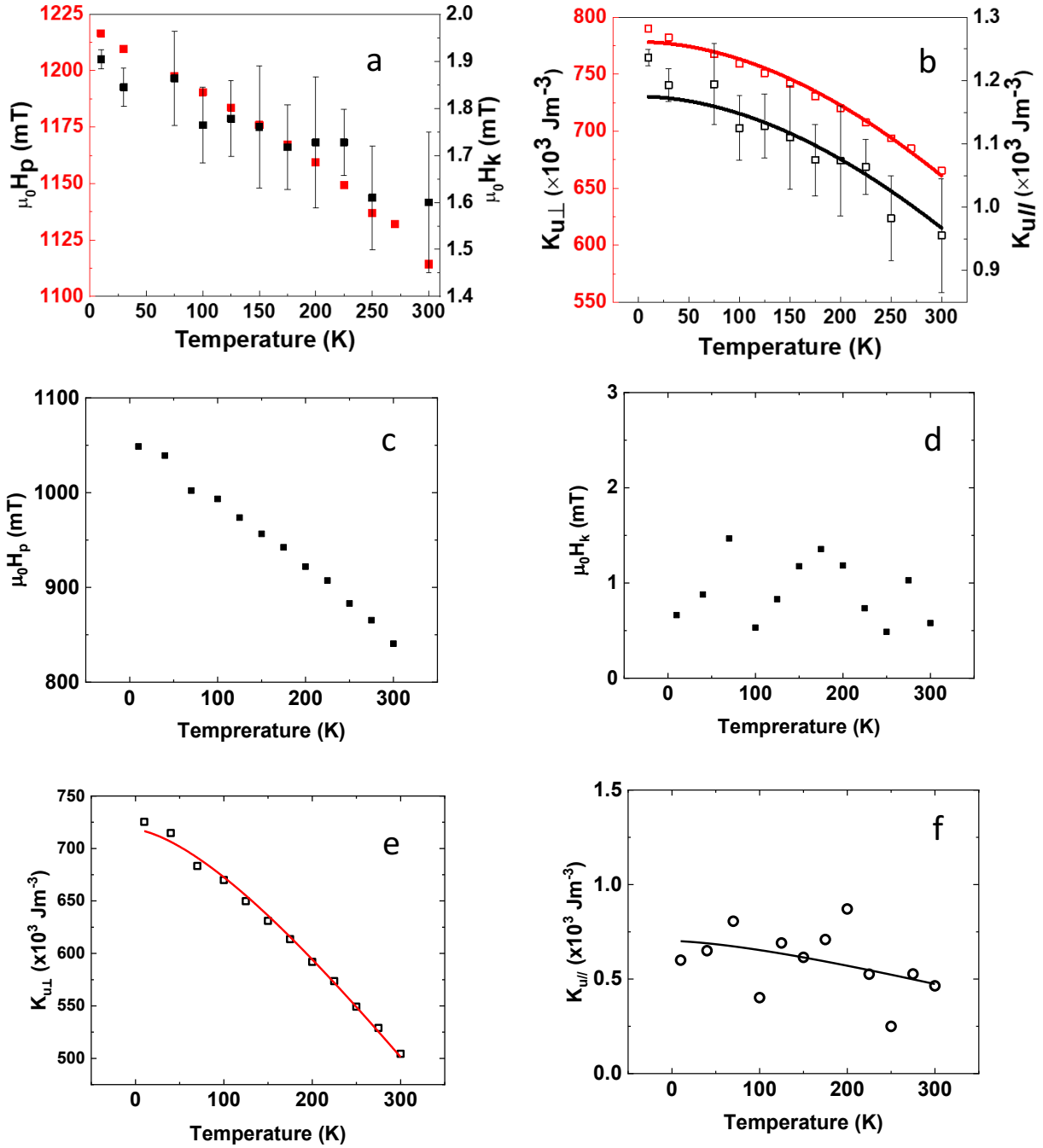


Figure 3.8a, Temperature dependence of anisotropy fields H_p (red squares) and H_k (black squares) for 2.0nm thick CoFeB layer. Corresponding data for a 2.2 nm thick CoFeB layer in **c** and **d** respectively. **b**, Anisotropy energies $K_{u\perp}$ (red squares) and $K_{u\parallel}$ (black squares) corresponding to H_p and H_k are plotted as a function of temperature corresponding to data in **a**. Lines are fits to power law of magnetization given by Eq. (3.13) with $\gamma = 2.1$ and 2.3 for $K_{u\perp}$ and $K_{u\parallel}$. Anisotropy energies **e**, $K_{u\perp}$ and **f**, $K_{u\parallel}$ corresponding to **c**, and **d**, respectively. Lines are fits to power law of magnetization given by Eq. (3.11) with $\gamma = 2.4$ and 2.5 for $K_{u\perp}$ and $K_{u\parallel}$.

3.6. Conclusion

In conclusion, a systematic study of magnetic annealing on the magnetic anisotropy of CoFeB/MgO junctions has been presented in this chapter based on the results obtained from simulations and experiments [32,33]. An expression to estimate the in-plane and perpendicular magnetic anisotropy fields has been derived from the Smit-Beljers' relation. Subsequently, the results of annealing effect on the saturation magnetization was presented, which shows that our multilayer structures maintain a roughly constant value of saturation magnetization upto 400°C. Following this, the results of magnetic annealing were presented. Magnetic annealing was found to induce a magnetic anisotropy along the direction of a bias field applied during the process of annealing. In addition, the annealing temperature effect was also found to significantly control the magnitudes of magnetic anisotropy fields. This effect was studied for CoFeB thicknesses ranging from 1.5 nm to 2.0 nm, all of which showed similar behaviour.

In the latter part of the chapter, we studied the measurement temperature effect on the magnetization and magnetic anisotropy fields. Saturation magnetization was found to follow the Bloch's law with different coefficients in low and high temperature ranges. Below 50 K, we obtain $\chi = 1.5$, while in the range of 50 K – 300 K, χ was estimated to be 1.8 for multilayers with a 2.0 nm thick CoFeB film. The in-plane and perpendicular magnetic anisotropies showed a monotonous decrease with increasing temperatures. Upon fitting the corresponding anisotropy energies to the Callen-Callen law, we obtain similar scaling exponents. This indicates they could have similar interfacial origins in ultrathin CoFeB/MgO junctions. Such a finding is especially interesting because it opens up avenues to control not just the perpendicular, but also the in-plane magnetic anisotropy using electric-fields as will be discussed in the following chapters.

References:

1. R. L. Stamps, S. Breitzkreutz, J. Akerman, A. V. Chumak, Y. Otani, G. E. W. Bauer, J.-U. Thiele, M. Bowen, S. A. Majetich, M. Klui, I. L. Prejbeanu, B. Dieny, N. M. Dempsey, and B. Hillebrands *J. Appl. Phys. D: Appl. Phys.* **47**, 333001 (2014)
2. J.S. Slonczewski, *J. Magn. Magn. Mater.* **159**, L1-L7 (1996).
3. L. Berger, *Phys. Rev. B* **54**, 9353-9358 (1996).
4. M. Farle, *Rep. Prog. Phys.* **61**, 775-826 (1998).
5. S. Chikazumi, *International series of monographs on physics 94: Physics of Ferromagnetism*. Oxford University Press (2009).
6. K. Watanabe, B. Jinnai, S. Fukami, H. Sato and H. Ohno, *Nat. Commun.* **9**, 663 (2018).
7. L. Neel, *J. Phys. Rad.* **15**, 225-239 (1954).
8. H. Meng and J.P. Wang, *Appl. Phys. Lett.* **88**, 172506 (2006).
9. T. Kishi, H. Yoda, T. Kai, T. Nagase, E. Kitagawa, M. Yoshikawa, K. Nishiyama, T. Daibou, M. Nagamine, M. Amano, S. Takahashi, M. Nakayama, N. Shimomura, H. Aikawa, S. Ikegawa, S. Yuasa, K. Yakushiji, H. Kubota, A. Fukushima, M. Oogane, T. Miyazaki and K. Ando, *IEDM Tech. Dig.* **309**, 312 (2008).
10. T. Maruyama, Y. Shiota, T. Nozaki, K. Ohta, N. Toda, M. Mizuguchi, A.A. Tulapurkar, T. Shinjo, M. Shiraishi, Y. Ando and Y. Suzuki, *Nat. Nanotechnol.* **4**, 158-161 (2009).
11. H.X. Yang, M. Chshiev, B. Dieny, J.H. Lee, A. Manchon and K.H. Shin, *Phys. Rev. B* **84**, 054401 (2011).
12. J. M. Shaw, H.T. Nembach, M. Weiler, T.J. Silva, M. Schoen, J.Z. Sun and D.C. Worledge, *IEEE Magn. Lett.* **6**, 1-4 (2015).
13. W. X. Wang, Y. Yang and H. Naganuma, Y. Ando, R.C. Yu, X.F. Han, *Appl. Phys. Lett.* **99**, 012502 (2011).
14. W. Skowronski, T. Nozaki, D.D. Lam, Y. Shiota, K. Yakushiji, H. Kubota, A. Fukushima, S. Yuasa and Y. Suzuki, *Phys. Rev. B* **91**, 184410 (2015).
15. S. Ikeda, K. Miura, H. Yamamoto, K. Mizunuma, H.D. Gan, M. Endo, S. Kanai, J. Hayakawa, F. Matsukura and H. Ohno, *Nat. Mater.* **9**, 721-724 (2010).
16. Y. Fu, I. Barkukov, J. Li, A.M. Goncalves, C.C. Kuo, M. Farle and I.N. Krivorotov, *Appl. Phys. Lett.* **108**, 142403 (2016).
17. A. A. Timopheev, R. Sousa, M. Chshiev, H. T. Nguyen, and B. Dieny, *Sci. Rep.* **6**, 26877 (2016).
18. J.B. Mohammadi, K. Cole, T. Mewes and C.K.A. Mewes, *Phys. Rev. B* **97**, 014434 (2018).
19. F. Bloch, *Z. Physik* **61**, 206 (1930); **74**, 295 (1932).
20. H.B. Callen and E. Callen, *J. Phys. Chem. Solids* **27**, 1271 (1966).
21. J. Smit and H.G. Beljers, *Philips Res. Repts.* **10**, 113-130 (1955).

22. H. Meng, W. H. Lum, R. Sbiaa, S. Y. H. Lua, and H. K. Tan, *J. Appl. Phys.* **110**, 033904 (2011).
23. M. Vázquez, J. González and A. Hernando, *J. Magn. Magn. Mater.* **53**, 4, 323-329 (1986).
24. S. Taniguchi, *Sci. Rep. Res. Inst. Tohoku Univ.* **A7**, 269-281 (1955).
25. S. Chikazumi and T. Oomura, *J. Phys. Soc. Japan.* **10**, -849 (1955).
26. L. Neel, *J. Appl. Phys* **30**, 3S (1959).
27. I. Barsukov, Y. Fu, C. Safranski, Y.-J. Chen, B. Youngblood, A.M. Goncalves, M. Spasova, M. Farle, J.A. Katine, C.C. Kuo and I.N. Krivorotov, *Appl. Phys. Lett.* **106**, 192407 (2015).
28. F.M. Dyson, *Phys. Rev.* **102**, 5 (1956).
29. J. G. Alzate, P.K. Amiri, G. Yu, P. Upadhyaya, J.A. Katine, J. Langer, B. Ocker, I.L. Krivorotov and K.L. Wang, *Appl. Phys. Lett.* **104**, 112410 (2014).
30. H. Sato, P. Chureemart, F. Matsukura, R.W. Chantrell, H. Ohno and R.F.L. Evans, *Phys. Rev. B* **98**, 214428 (2018).
31. Z. Wen, H. Sukegawa, T. Seki, T. Kubota, K. Takanashi and S. Mitani, *Sci. Rep.* **7**, 45026 (2017).
32. A. Deka, K. Sato, I. Tanaka and Y. Fukuma, *IEEE Trans. Mag.* **56**, 3(2020).
33. A. Deka, B. Rana, R. Anami, K. Miura, H. Takahashi, Y. Otani and Y. Fukuma, *Phys. Rev. B* **101**, 174405 (2020).

Chapter 4

Micromagnetic simulations on the effect of magnetic anisotropy on switching of an easy cone magnetized free layer

4.1. Introduction

Magnetic tunnel junction (MTJ) based magnetoresistive random access memory (MRAM) have emerged as a promising candidate for high performance non-volatile storage devices. As mentioned earlier in Chapter 1, magnetization direction in the free layer of the MTJs can be controlled by magnetic fields [1], spin transfer torques [1, 2] and spin orbit torques [3,4], all of which require a flow of charge current in close proximity or inside the device. As a result, when the device sizes are scaled down, the need to remove unwanted Joule heating caused by the flow of charge currents becomes very important in order to maintain the device performance. Typically, in MRAMs, the the Oersted fields generated around a current carrying wire is used to switch the free layer of an MTJ that is placed near to it. But since these Oersted fields are spatially dispersed, there is a possibility of affecting neighboring memory elements. Thus a localized excitation mechanism is required. STT, being a localized mechanism, promises to address this issue but the requirement of an overlapping read and write current paths in the device architecture leads to switching of the memory element during the read process. This makes the process of device miniaturization difficult beyond a certain limit. SOT promises to overcome this issue via reduced current densities and possibility for a new MRAM circuit design where the read and write current paths are separated. However, current densities required are typically over 10^{10} Am⁻² which can give rise to significant Joule heating. Recently the effect of magneto-electric coupling through selective electron-hole doping in interfacial bonding states of ferromagnetic metal-oxide interfaces by application of voltage was demonstrated [5]. The advantage of such a control of magnetization via voltage in metallic ferromagnets is that it has the potential to eliminate

the charge currents required for magnetization switching and in turn help in development of ultralow power MRAMs. This motivates us to understand the switching process of a MTJ free layer element using micromagnetic simulations.

The first MTJs that were developed had two ferromagnetic layers with in-plane easy axes and separated by a thin tunnel barrier. Soon materials with perpendicular easy axes were developed which allowed us to have the option for perpendicular magnetized fixed and free layers too. Therefore, typical MTJs have a free layer that has either an in-plane or out-of-plane magnetic easy axis. However, the torque exerted by electric field on magnetization being a function of $\sin\theta\cos\theta$, is zero for an in-plane and out-of-plane magnetized film [6,7]. Therefore, an external bias magnetic field is typically used to tilt the magnetization away from the film plane or the normal during dynamical magnetization control via AC electric fields [8] – [10]. One of the potential solution to overcome the need for this bias magnetic field is by substituting the free layer of the MTJs with a ferromagnetic layer that has an easy cone state of magnetization [11, 12,13]. This easy cone state arises out of the competition between the second and fourth order PMA [11]. CoFeB/MgO junctions can also exhibit an easy cone state due to a 4th order PMA $H_{p,2}$, whose corresponding anisotropy energy $K_{u,4}$ is reported to vary from $-0.4\times 10^5 \text{ Jm}^{-3}$ to $1.0\times 10^5 \text{ Jm}^{-3}$ [11]. In this chapter, we present our results about the investigation on the transition of a ferromagnetic thin film from an out-of-plane easy axis into an easy cone state due to PMA. Such an easy cone can only be possible when the 2nd order PMA field H_p is higher than the demagnetizing field H_d . Subsequently, we discuss about the thermal stability of the same samples as a function of the PMA. Finally, the magnetization switching mechanism is studied. A comparison of the switching fields and times as a function of inclination angle from the film normal θ of the easy cone state is made.

4.2. Easy cone state and thermal stability

The process of estimating the stable state of magnetization is mentioned in Chapter 2. If we take into account the fourth order PMA $K_{u,4}$, the effective magnetic anisotropy of a ferromagnet can be written as:

$$E(\theta) = -K_{u,eff} \cos^2 \theta - K_{u,4} \cos^4 \theta, \quad (4.1)$$

where, the first term $K_{u,eff} = K_{u,d} - K_{u,2}$ and $K_{u,d}$ is the demagnetization energy.

In the absence of $K_{u,4}$, the magnetic easy axis is determined by the competition between $K_{u,d}$ and $K_{u,2}$, both of which have a $\cos^2\theta$ dependence. As a result, easy axis is possible either in the in-plane or out-of-plane directions, as shown in Fig. 4.1a and 4.1b respectively. When H_p , the field corresponding to second order PMA, overcomes the field corresponding to the demagnetizing energy, the minimum of E is along the normal to the film plane ($\theta = 0$ degree) which gives rise to a perpendicular easy axis. In this state, when a negative $K_{u,4}$ is introduced, a special kind of minimum for Eq. (4.1) is possible wherein it lies at a value of θ between 0 and 90 degree because $K_{u,4}$ has a $\cos^4\theta$ dependence. This state is called the easy cone state because the easy axis forms a cone of angle θ around the film normal as shown in Fig. 4.1c.

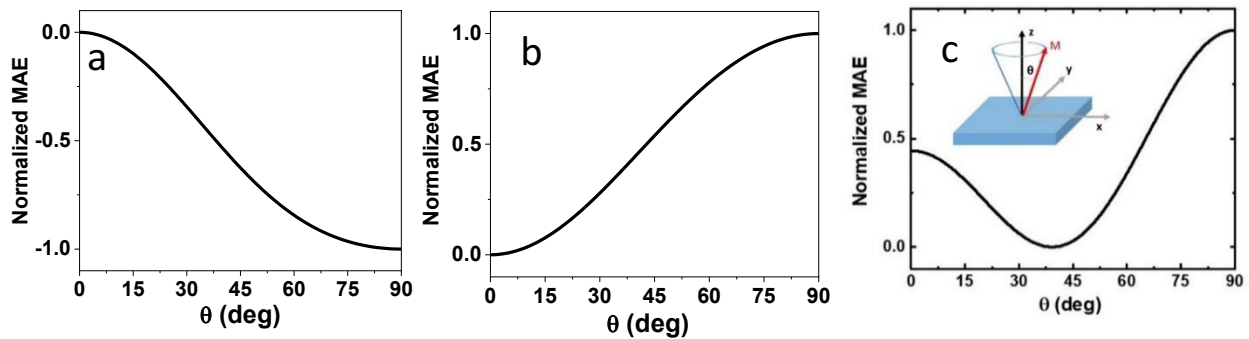


Figure 4.1a, MAE as a function of θ for a film with an **a**, in-plane easy axis **b**, out-of-plane easy axis and **c**, easy cone state. Inset in **(c)** showing the coordinate axes.

We estimated the equilibrium state of magnetization as a function of PMA and the evolution of the easy axis from a perpendicular to an easy cone state is shown by the dependence of θ with PMA in Fig. 4.2a. The value of θ can be analytically estimated by minimizing Eq. (4.1) to be of the form:

$$\theta = \cos^{-1} \sqrt{\frac{K_{u,eff}}{2K_{u,4}}} . \quad (4.2)$$

Upon fitting the values of θ obtained from the simulations as a function of PMA to (4.2), we can obtain a good accuracy with theory as shown by the lines in Fig. 4.1b. It can be seen from (4.2) that the out-of-plane easy axis state ($\theta = 0$ degree) transitions into an easy cone state when $K_{u,4} \geq K_{u,eff}/2$.

Subsequently the thermal stability factor Δ which gives a measure of the energy barrier separating the easy cone state from the in-plane hard axis can be estimated as follows [14]:

$$\Delta = \frac{E(90 \text{ deg}) - E(\theta)}{k_B T} A, \quad (4.3)$$

where A is the volume of the device, k_B is the Boltzmann's constant and T is the temperature of operation which is taken as 300 K. During calculation of Δ for the easy cone state, we initialized our simulation with the magnetization in the film plane and allow the magnetization vector to relax to the nearest lowest energy state. The difference in the energies between the initial and final states gives us: $E(90 \text{ deg}) - E(\theta)$. Substituting this value in Eq. (4.3), we obtain the value of Δ as shown in Fig. 4.2a. It can be seen from (1) that a negative $K_{u,4}$, can also result in a decrease in E which in turn reduces the thermal stability factor that is a key parameter of memory devices. Typically, for the condition of non-volatility in memory devices, $\Delta = 60$ is required for a retention period of about 10 years. Therefore, during the discussion of magnetization switching conditions for easy cone magnetized samples in the subsequent section, we ensured that the samples have $\Delta \geq 60$.

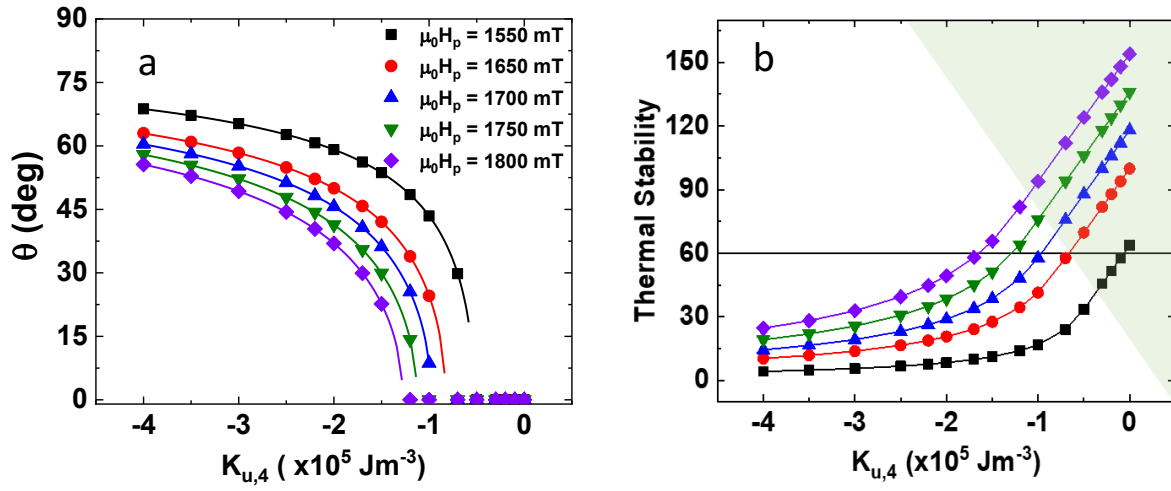


Figure 4.2 Evolution of **a**, easy axis from the perpendicular easy axis ($\theta = 0$ degree) to an easy cone state as a function of PMA. **b**, Thermal stability Δ as a function of 2nd and 4th order PMA. Highlighted area (green) in **b** refers to an in-plane easy axis.

4.3. Magnetization switching using electric-fields

Whenever the effective magnetic field H_{eff} in a ferromagnet changes, the magnetization M precesses around the new H_{eff} and aligns parallel to it to reach the new energy minima. This process is well defined by a sum of precessional and damping torques given by Eq. (2.1). In the presence of an electric field at the interface of the ferromagnet, PMA can be modified by the change of electron occupancies in its interfacial $3d$ orbitals [6]. Such an effect is typically quantified by the voltage controlled magnetic anisotropy (VCMA) coefficient ζ which represents the change in magnetic anisotropy energy per unit electric field at the interface of the ferromagnet. The application of a voltage results in a change of effective magnetic anisotropy energy. As a result, H_{eff} , which can be estimated from the derivative of the magnetic free energy (see Sec. 5.3) with respect to the magnetization vector m , changes and the magnetization precesses to the new minimum. If ζ of the ferromagnet is sufficient enough, so that during this precession M crosses the equatorial film plane, the magnetization can be switched from the upper (lower) cone to the other side by turning off the voltage. Typical reported values of ζ for second order PMA range from about $0.01 \text{ pJV}^{-1}\text{m}^{-1}$ for CoFeB/MgO junctions [14] upto about $0.25 \text{ pJV}^{-1}\text{m}^{-1}$ for FePt/MgO junctions [15]. Based on this, corresponding voltage induced change in the second order PMA field of up to 150 mT can be expected in such materials.

Since our micromagnetic simulator does not allow us to apply electric fields, the electric field effect can be modelled as a z-axial field pulse H_z which is equivalent to the change in PMA in presence of an interfacial voltage. Switching condition of the samples are studied by varying the field pulse amplitudes. Switching time t_{swit} is taken as the time when the z-component of magnetization m_z crosses the equator defined by $m_z = 0$. H_{s0} , which is defined as the minimum amplitude of H_z required for switching the magnetization vector, was estimated as a function of PMA. As shown in Fig. 4.2b, it is observed that the H_{s0} decreases with a decrease in $K_{u,2}$ and $K_{u,4}$. This can be understood in terms of a reduced potential barrier

between the easy and hard axes. Also, as can be seen in the same figure, it is possible for samples with different combinations of $K_{u,2}$ and $K_{u,4}$ to have equal values of H_{s0} . Therefore, for discussing the magnetization switching times, we selected samples S-1 to S-5 that have an equal value of $\mu_0 H_{s0} = 104$ mT. The values of $K_{u,2}$ and $K_{u,4}$ for these samples, as given in Table 1, are such that they have equal Δ and corresponding $\theta = 4, 19, 29, 34$ and 41 degrees respectively. This enables us to make a comparison of the magnetization switching dynamics as a function of θ .

Figure 4.2c shows estimated t_{swit} as a function of H_z for S-1 to S-5. Switching times decreased with increasing amplitude of the field pulse and inclination angle. The reduction in switching times with increasing fields can be understood in terms of a higher torque on magnetization given by $M \times H_{\text{eff}}$. In order to explain the switching behavior as a function of the inclination angle of the easy cone state, we plot the time dependence of the magnetization components of S-3 and S-5 in Fig. 4.2d – 4.2f. Interestingly, even though all the samples have the same $\mu_0 H_{s0} = 104$ mT, for any fixed field amplitude, the switching process depends on the inclination angles of the easy cone state. While the switching time at H_{s0} is lowest for S-5 that has $\theta = 41$ degree, it increases as θ decreases. This points towards an increase in torque on magnetization when θ is increased. Such an increase is confirmed from a faster magnetization precession for S-5 compared to S-3, as shown in the time evolution of m_x and m_y in Fig. 4.2e and 4.2f respectively. The torque on m is applied in the film plane because H_{eff} is perpendicular to the film. For a fixed damping factor, an increase in the torque will consequently increase the Gilbert damping torque that is orthogonal to the torque. This in turn gives rise to a lower switching time as the inclination angles are increased. In this way we can explain the phenomenon of magnetization switching using electric-fields in an MTJ that has a easy cone magnetized free layer.

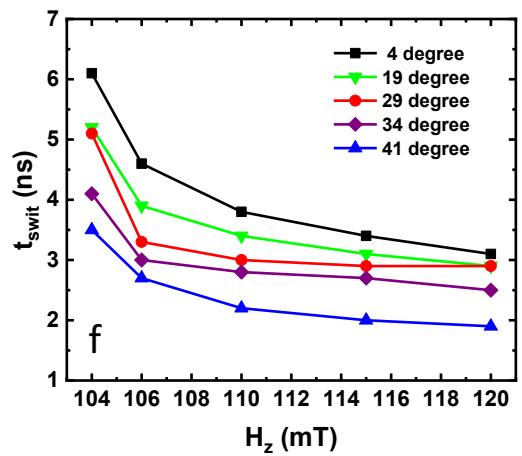
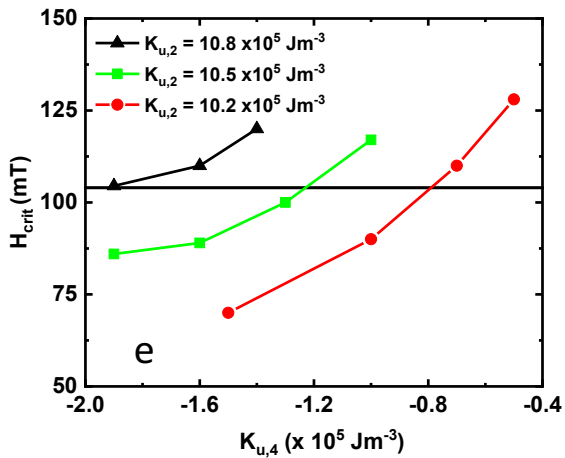
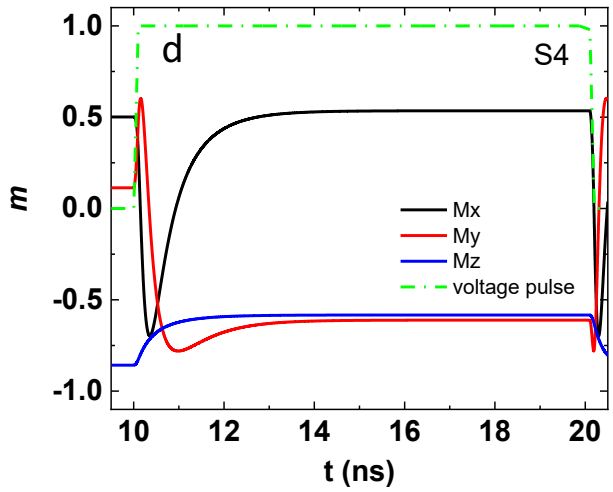
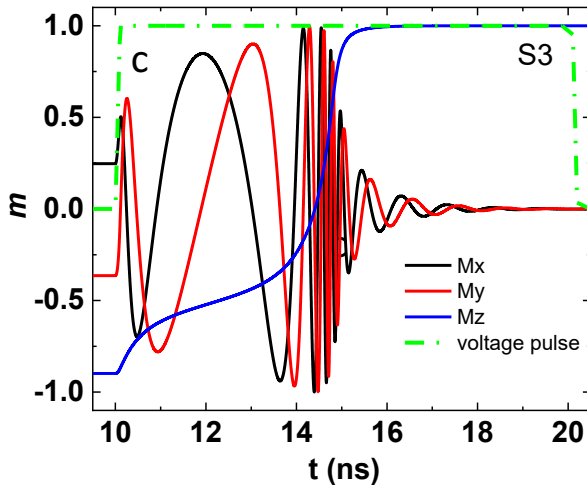
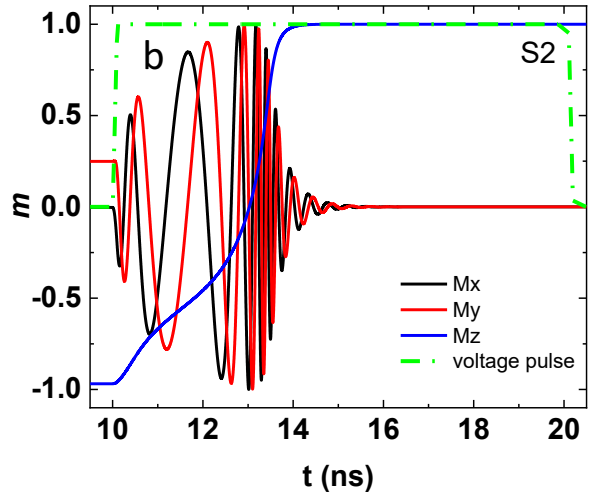
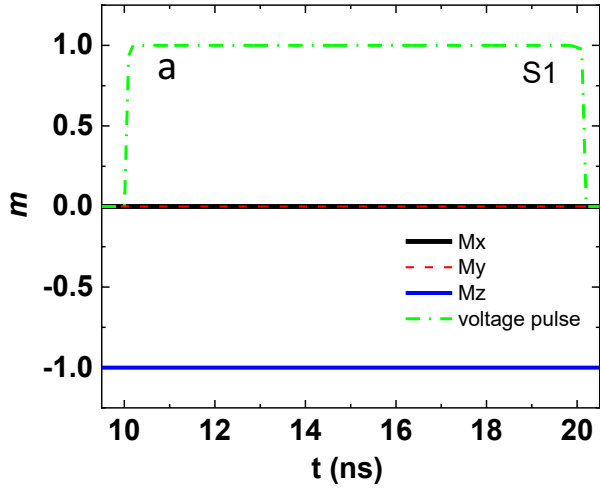


Figure 4.3a-d, Time evolution of the magnetization components when a magnetic field pulse of 100 mT is applied. The field amplitude is equivalent to the change in PMA change due to voltage is applied and so it is depicted in the figures **a**, to **d**, as voltage pulse (green). The cases shown correspond to a film with **a**, perpendicular easy axis and easy cone state stabilized films with easy cone angles of **b**, 10 degrees, **c**, 20 degree and **d**, 30 degrees. The change of **e**, critical switching fields with respect to PMA and **f**, switching times as a function of pulse amplitude and inclination angle of the easy cone state.

4.4. Conclusions

The dependence of the magnetic state on perpendicular magnetic anisotropy was investigated. VCMA of PMA can't be used to excite magnetization dynamics when the samples are aligned in the in-plane or perpendicular directions. Such a constraint makes it necessary for us to use a bias magnetic field to tilt the magnetization during voltage controlled switching processes in storage devices. But an MTJ free layer magnetized in the easy cone state can be used to overcome this requirement. It showed that a competition between the second and fourth order PMA can give rise to an easy cone state of magnetization which is due to differences in angular dependences of the second and fourth order PMA. Thermal stability was found to decrease with decreasing effective anisotropy due to a decrease in the energy barrier separating the easy cone state from the in-plane direction. Upon comparison of samples with equal values of minimum switching fields but different θ , varying from 4 to 41 degrees, switching time was found to be lowest for the sample with an easy cone angle of 41 degrees. This could be understood in terms of an increase in the torque with an increase of the inclination of the easy cone state with respect to the film normal. It should however be mentioned here that the values of $K_{u,2}$ and $K_{u,4}$ required for these processes to ensure both an easy cone state and $\Delta = 60$ for memory applications is beyond those typically reported for CoFeB/MgO junctions. Therefore, although theoretically it is possible to use them for magnetic-field free switching applications, magnetic anisotropy and electric-field effects in the easy cone state of a CoFeB/MgO junction are not sufficient for storage devices. This calls for alternative mechanisms to explore the possibility of a magnetic-field free control of magnetization in ferromagnetic metals. We will show our experimental and simulation results towards this goal in the next final two chapters of this thesis.

References

1. J. Slonczewski, *J. Magn. Magn. Mater.* **159**, L1 (1996).
2. L. Berger, *Phys. Rev. B* **54**, 9353 (1996).
3. I. M. Miron, K. Garello, G. Gaudin, P.-J. Zermatten, M. V. Costache, S. Auffret, S. Bandiera, B. Rodmacq, A. Schuhl and P. Gambardella, *Nature* **476**, 189-193 (2011).
4. L. Liu, C.-F. Pai, Y. Li, H.W. Tseng, D.C. Ralph and R.A. Buhrman, *Science* **336**, 555 (2012).
5. T. Maruyama, Y. Shiota, T. Nozaki, K. Ohta, N. Toda, M. Mizuguchi, A.A. Tulapurkar, T. Shinjo, M. Shiraishi, Y. Ando and Y. Suzuki, *Nat. Nanotechnol.* **4**, 158-161 (2009).
6. T. Nozaki, Y. Shiota, S. Miwa, S. Murakami, F. Bonell, S. Ishibashi, H. Kubota, K. Yakushiji, T. Saruya, A. Fukushima, S. Yuasa, T. Shinjo and Y. Suzuki, *Nat. Phys.* **8**, 491–496 (2012).
7. J. Zhu, J.A. Katine, G. E. Rowlands, Y.-J. Chen, Z. Duan, J.G. Alzate, P. Upadhyaya, J. Langer, P.K. Amiri, K.L. Wang and I.N. Krivorotov, *Phys. Rev. Lett.* **108**, 197203 (2012).
8. S. Kanai, F. Matsukura and H. Ohno, *Appl. Phys. Lett.* **108**, 192406 (2016).
9. K. Miura, S. Yabuuchi, M. Yamada, M. Ichimura, B. Rana, S. Ogawa, H. Takahashi, Y. Fukuma and Y. Otani, *Sci. Rep.* **7**, 42511 (2017).
10. B. Rana, Y. Fukuma, K. Miura, H. Takahashi and Y.C. Otani, *Appl. Phys. Lett.* **111**, 052404 (2017).
11. J. M. Shaw, H.T. Nembach, M. Weiler, T.J. Silva, M. Schoen, J.Z. Sun and D.C. Worledge, *IEEE Magn. Lett.* **6**, 1-4 (2015).
12. R. Matsumoto, T. Nozaki, S. Yuasa and H. Imamura, *Phys. Rev. Appl.* **9**, 014026 (2018).
13. A. A. Timopheev, R. Sousa, M. Chshiev, H. T. Nguyen and B. Dieny, *Sci. Rep.* **6**, 26877 (2016).
14. J. G. Alzate, P.K. Amiri, G. Yu, P. Upadhyaya, J.A. Katine, J. Langer, B. Ocker, I.L. Krivorotov and K.L. Wang, *Appl. Phys. Lett.* **104**, 112410 (2014).
15. S. Miwa, M. Suzuki, M. Tsujikawa, K. Matsuda, T. Nozaki, K. Tanaka, T. Tsukahara, K. Nawaoka, M. Goto, Y. Kotani, T. Ohkubo, F. Bonell, E. Tamura, K. Hono, T. Nakamura, M. Shirai, S. Yuasa and Y. Suzuki, *Nat. Commun.* **8**, 15848 (2017).
16. A. Deka, K. Sato, I. Tanaka and Y. Fukuma; *IEEE Trans. Mag.* **56**, 3 (2020).

Chapter 5

Electric-field induced magnetization dynamics in an in-plane magnetized CoFeB/MgO junction

5.1. Introduction

In the previous chapter, magnetization switching was investigated as a function of PMA using which we could observe that the benefits of VCMA in the storage technology is limited by the low VCMA coefficients reported so far. This motivates us to explore the benefits of VCMA in other spintronics devices such as in the field of spin current and spin wave generation. Recent discoveries such as spin-transfer torque, spin-orbit torque and electric-field torque provide a new strategy for designing future spintronic devices which require power efficient excitation of magnetization dynamics. In this regard, spin-transfer torque has been mainly utilized for exciting the magnetization dynamics in magnetic nano-structures [1,2]. However, there is an inevitable effect of Joule heating because of a high charge current density of $\sim 10^{11}$ A/m² in the devices. Spin-orbit torques generated at an interface between non-magnetic metals with strong spin-orbit interaction and ferromagnetic metals could be a promising approach for energy-efficient manipulation [3,4], yet recently reported charge current densities required for magnetization switching or exciting spin waves remain too large to be ignored [5,6]. Further significant reduction of power consumption is envisaged by electric-field control of magnetization [7]. Although magneto-electric effects have been realized through several mechanisms such as piezoelectricity [4] and reversible oxidation [5], voltage controlled magnetic anisotropy (VCMA) is particularly interesting because it allows us to excite magnetization in the sub-nanosecond regime.

As discussed in Chapter 1, the effect of an electric-field on magnetic properties has been reported for various systems, such as magnetic semiconductors, multiferroic materials and magnetic metal/oxide

bilayers [8]. The demonstration of modulation of coercive fields of FePt using electric fields by Weisheit et al. in 2008 generated lot of interest in the electric-field control of magnetization in ferromagnetic metals [9]. In particular, CoFeB/MgO junctions have emerged as an attractive system for studying VCMA related phenomena because of its great potential to realize ultra-low power spintronic nanodevices, thanks to its giant tunneling magnetoresistance [10,11] and strong perpendicular magnetic anisotropy (PMA) [12]. The magneto-electric coupling at the CoFeB/MgO interface allows us to control magnetization dynamics by using electric-fields. Based on this, a variety of dynamical magnetization phenomena such as ferromagnetic resonance (FMR) excitation, magnetization switching and spin wave excitation have been demonstrated [7,13-18].

One mechanism to explain the electric-field effect is that magnetic anisotropy energy is changed by selective electron-hole doping into $3d$ orbitals of the interfacial ferromagnetic atoms through spin-orbit interaction [19,20]. This interfacial PMA shows uniaxial symmetry where its energy is expressed in the form of $K_{u\perp}\sin^2\theta$, with $K_{u\perp}$ being the uniaxial PMA energy and θ being the elevation angle of the magnetization from the film plane. The energy density contour arising due to such an uniaxial PMA is shown in Fig. 5.1a. The corresponding electric-field torque caused by VCMA is estimated to be a function of $\sin\theta\cos\theta$ obtained from the derivative of the energy terms. Therefore, VCMA experiments have so far used an external magnetic field for titling the magnetization direction because electric-field torque is zero in the in-plane ($\theta = 0$ degree) or out-of-plane ($\theta = 90$ degree) magnetized samples [7]. This makes it necessary for VCMA experiments to have a bias magnetic field in order to tilt the magnetization away from the easy direction to initiate magnetization dynamics [6-9]. Although non-linear magnetization dynamics such as spin waves have been predicted to be possible using electric-field induced parametric processes in perpendicular and in-plane magnetized ferromagnetic metal-oxide junctions, it should be noted that they are threshold processes which limits the feature of power efficiency [21-23]. Thus, there is a need for alternative avenues to excite purely electric-field induced magnetization dynamics in the linear regime.

In Chapter 3, it was shown that both perpendicular and in-plane magnetic anisotropy, i.e. PMA and IMA respectively, can follow the power law of magnetization with comparable scaling exponents, which indicated their interfacial origin. In this chapter, experiments on the electric-field control of interfacial magnetic anisotropy using a DC bias voltage are presented. We demonstrate that it is possible to control both PMA and IMA using electric-fields in CoFeB/MgO junctions. The presence of both PMA and IMA significantly modified the energy contour as shown schematically in Fig. 5.1b. In addition, a non-zero electric-field torque is expected for the in-plane magnetized films if the interfacial magnetic anisotropy has an in-plane uniaxial component $K_{u//}$, which is expressed in the form $K_{u//}\cos^2\theta\cos^2\phi$, ϕ being the azimuthal angle. Such a modification of the electric-field torque offers an interesting opportunity to explore purely voltage-controlled spintronic devices. Subsequently, a phenomenological model for the angular dependence of the torques arising out of VCMA of both in-plane and perpendicular magnetic anisotropy fields is developed. Such a torque is then fitted to the spin pumping model to obtain the angular dependences of the rectified voltage arising from spin pumping and inverse spin Hall effect measurements. Finally, experimental results on the excitation of ferromagnetic resonance using electric-fields in an in-plane magnetized CoFeB/MgO junction are presented which fits well with the phenomenological model to prove that VCMA of H_k indeed plays a role in excitation of FMR using electric-fields.

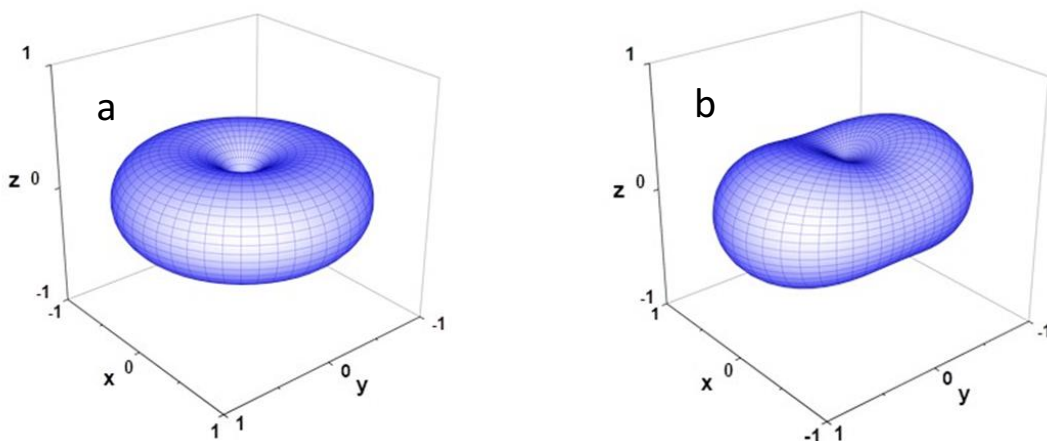


Figure 5.1 a, Anisotropy energy contour arising from uniaxial perpendicular magnetic anisotropy H_p . **b**, Schematic to illustrate the resulting anisotropy energy contour when, in addition to H_p , an in-plane magnetic anisotropy H_k is present along x-axis. Such an anisotropy has been demonstrated to be induced by magnetic annealing in Chapter 3.

5.2. Modulation of magnetic anisotropy using a DC bias voltage

In this section, the effect of a DC electric-field on H_k and H_p of the CoFeB/MgO junction via spin pumping and ISHE measurements is presented. The fabrication process of devices for this purpose was explained in Chapter 2. A typical schematic of the experimental set up used in this process of electrical detection of FMR is shown in Fig. 5.2a. In this setup, the microwave magnetic field $h_{rf,z}$ was applied perpendicular to the CoFeB layer from a nearby CPW. Figure 5.2b shows the detected rectified voltage signal as a function of an external magnetic field H_{ex} for frequency $f = 3.0$ GHz when $\phi = 0$ degree. The rectified voltage is fitted to the following equation to characterize its lineshape:

$$V = \frac{L \times dH^2}{(H_{ex} - H_{res})^2 + dH^2} + \frac{D \times dH \times (H_{ex} - H_{res})}{(H_{ex} - H_{res})^2 + dH^2}, \quad (5.1)$$

where, L and D are the weights of the Lorentzian and dispersive parts, respectively, dH is the half width at half maximum (HWHM). From the fitting of the data using Eq. (5.1) we obtain $L = -2.42 \times 10^{-6} \mu\text{V}$ and $D = 3.13 \times 10^{-8} \mu\text{V}$ in the positive field direction, indicating that the lineshape is highly symmetric. Upon fitting the data in the negative field direction using Eq. (5.1), we obtain $L = 2.45 \times 10^{-6} \mu\text{V}$ and $D = 5.15 \times 10^{-8} \mu\text{V}$. This shows that when the field direction is reversed, the symmetric voltage signal is reversed. Such a lineshape indicates the origin of this rectified voltage could be spin pumping and subsequent conversion to charge current via spin Hall effect.

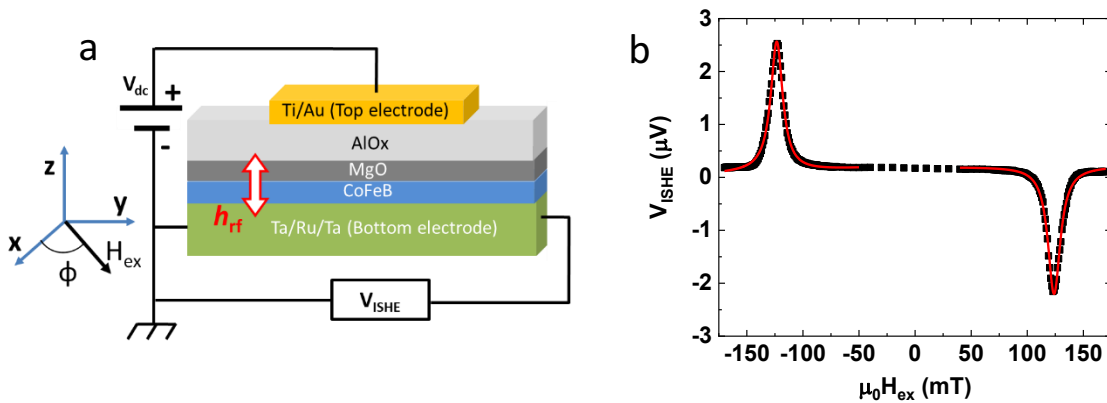


Figure 5.2 a, Schematic of the experimental setup used to detect FMR signal electrically via spin pumping and inverse spin Hall effect (ISHE). **b**, V_{ISHE} spectra for h_{rf} frequency of 3.0 GHz when $\phi = 0$ degree.

It is reported that the lineshape of the rectification voltage in spin pumping measurements strongly depends upon the microwave magnetic field distribution in the sample and contributions from anomalous Hall effect (AHE) or anisotropic magnetoresistance (AMR) [24]. According to Harder *et al.*, in this setup, AHE and AMR of the ferromagnet shows dispersive and Lorentzian lineshape, respectively, and ISHE shows Lorentzian lineshape. However, the AMR and ISHE spectra amplitudes show angular dependent behavior of the types $\sin 2\phi$ and $\sin\phi$ respectively. Therefore, an angular dependent measurement of the electrical detection of FMR was performed to investigate its origin. Figure 5.3a shows the rectified voltage when $\phi = 80$ degree, which is highly symmetrical (like Fig. 5.2b). The Lorentzian and dispersive components are plotted as a function of ϕ in Fig. 5.3b. The data fits well to the function of $\sin\phi$. This confirms that the rectified voltage originates from inverse spin Hall effect where the FMR is excited by a z-axial microwave field.

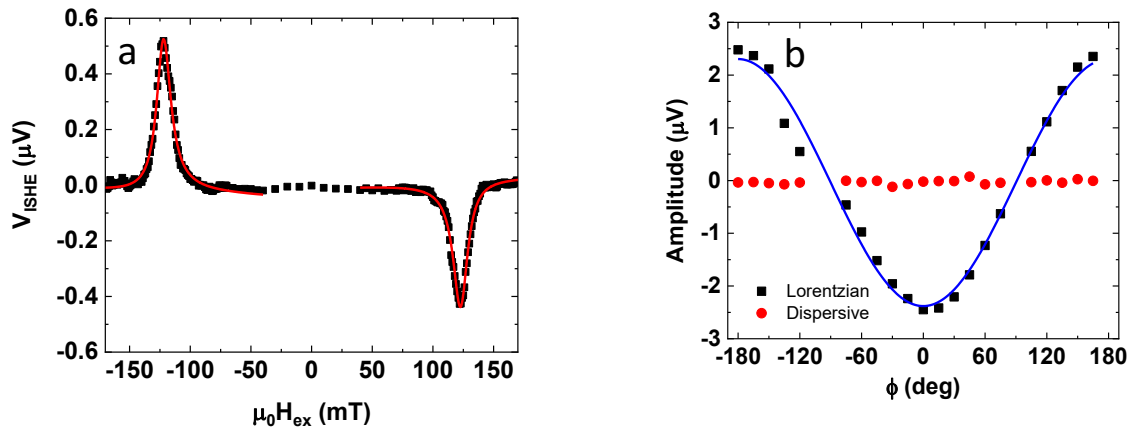


Figure 5.3 **a**, V_{ISHE} spectra for h_{rf} frequency of 3.0 GHz when $\phi = 80$ degree. **b**, In-plane angle ϕ dependence of the Lorentzian and dispersive amplitudes (symbols) of the rectified voltage V_{ISHE} lineshapes. Line is fitted for a $\sin\phi$ dependence.

The rectified voltages are recorded for frequencies ranging from 1.0 GHz to 5.0 GHz as shown in Fig. 5.4a. The magnitude of the rectification voltage in the spectra increases with increasing frequency up to 3.0 GHz, and then starts to decrease with the further increase of frequency. This behavior is due to the fact that the spin current increases with increasing frequency for the spin pumping mechanism, but the increase of H_{ex} during FMR decreases the cone angle of magnetization precession, and therefore the generation of the spin current is suppressed at high frequencies [25]. The dependence of V_{ISHE} on the microwave frequency and H_{ex} is plotted as a color map in Fig. 5.4b. The increase of resonant magnetic field monotonically with frequency is consistent with Kittel formula.

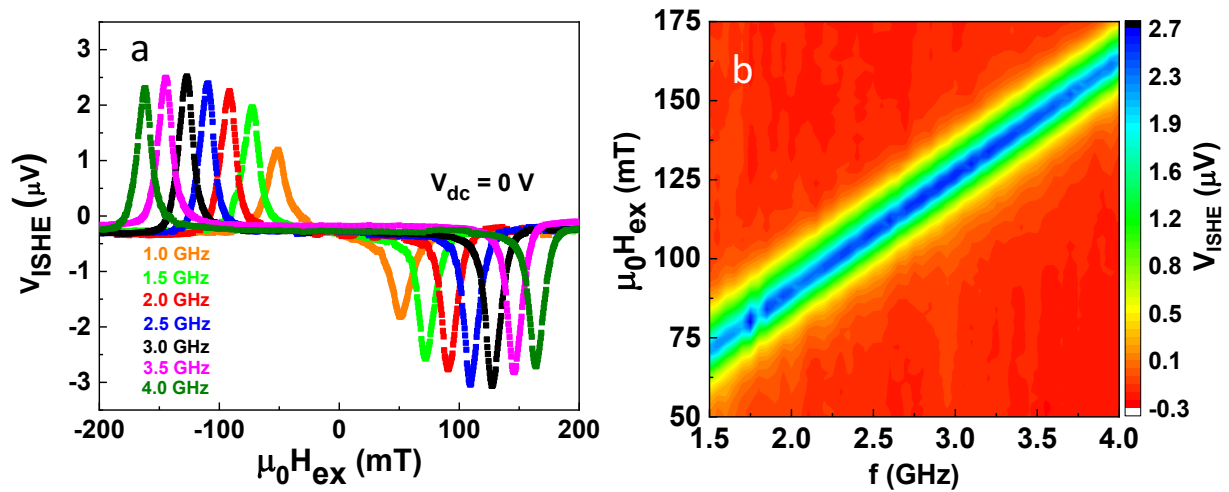


Figure 5.4 a, External magnetic field H_{ex} dependence of V_{ISHE} at different frequencies. **b**, Color-coded V_{ISHE} spectra. Measurements were performed at an input power of 15 dBm and the bias voltage at the gate electrode was zero.

DC bias voltage V_{dc} is applied in the sample, as shown in Fig. 5.2a. The effect of V_{dc} on the ISHE spectra is plotted in Fig. 5.5a. The resonant field $\mu_0 H_{res}$ is monotonically changed from 80 mT to 94 mT by applying V_{dc} . In order to understand the origin of the change of H_{res} on V_{dc} , firstly, the gyromagnetic ratio γ in Eq. (3.1) is estimated. We used a process similar to a method described by Shaw *et al.* [26], which shows that the error in simultaneous estimation of the effective magnetization M_{eff} and gyromagnetic ratio from the Kittel equation can be minimized by recording the FMR spectra up to H_{ex} well above the M_{eff} . The FMR spectra was detected electrically with an in-plane $\mu_0 H_{ex}$ up to 800 mT along $\varphi = 0$ degree. H_{res} obtained are plotted as a function of frequency as shown in Fig. 5.5b. In case of $\varphi = 0$ degree, Eq. (3.8) reduces to the typical form of Kittel equation Eq. (3.1). The in-plane anisotropy can be assumed to be absent in this process since its effect was found to be negligible for our purposes. We obtain $M_{eff} = 50$ mT and $\gamma = 0.0298$ GHz/mT from the fitting. Furthermore, we could not detect any effect of electric-field on the gyromagnetic ratio in the applied bias voltage range.

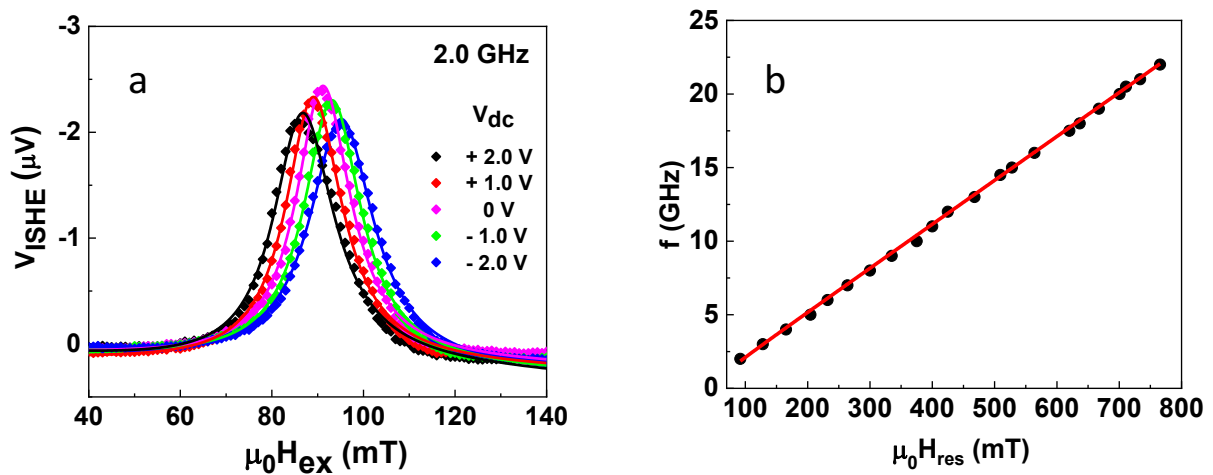


Figure 5.5 a, Dependence of V_{ISHE} spectra on bias voltage V_{dc} at $f = 2.0$ GHz (symbols). The lines are fits to experimental data by using Eq. (5.1). **b**, Resonance fields H_{res} as a function of f (symbols) with fits to Eq. (3.1).

Since the gyromagnetic ratio is found to be invariant with V_{dc} , secondly, the change of H_p and H_k on the application of V_{dc} is estimated. The V_{ISHE} spectra were measured as a function of in-plane magnetic field angle ϕ at different bias voltages, as discussed in the previous paragraph. Surprisingly, the sinusoidal amplitude in the ϕ dependence of H_{res} , as shown in Fig. 5.6a, is strongly modulated by applying V_{dc} , implying voltage-control for H_k . Upon fitting the experimental data using Eq. (3.8), it can be observed that H_p and H_k are controlled by bias voltage with a mutually opposite dependence on V_{dc} . Figure 5.6b shows the change of the anisotropy fields and the corresponding anisotropy energies on the left and right axes respectively, as a function of V_{dc} with respect to the unbiased condition ($V_{dc} = 0$ V) for frequencies from 1.0 GHz to 3.0 GHz. When the top electrode is at a lower potential than the bottom CoFeB electrode (negative bias voltage), H_p is observed to increase, whereas H_k remains almost unchanged. On the other hand, a positive bias voltage decreases H_p and increases H_k .

The penetration depths of the electric-field in metallic ferromagnets is about 0.1 nm and therefore the change of H_p and H_k with bias voltage suggests that PMA and IMA of the CoFeB/MgO junction are of interfacial origin. VCMA in ferromagnetic metal/oxide interface is understood by a relative change in electron density for the in-plane and out-of-plane oriented $3d$ orbitals of the interfacial ferromagnetic atoms in the presence of an electric-field [27]. The electron filling factor in the d_{z^2} orbital is reduced by applying a negative voltage, which leads to increase in PMA. On the other hand, when a positive voltage is applied, the electron filling factors in the out-of plane and in-plane oriented $3d$ orbitals are enhanced and suppressed respectively, leading to a decrease in PMA, accompanied by an increase in IMA. The asymmetric trend of VCMA with respect to the sign of voltage in the samples is predicted for buffer layer/ferromagnetic metal/oxide multilayers which lack spatial inversion symmetry perpendicular to the film plane [28].

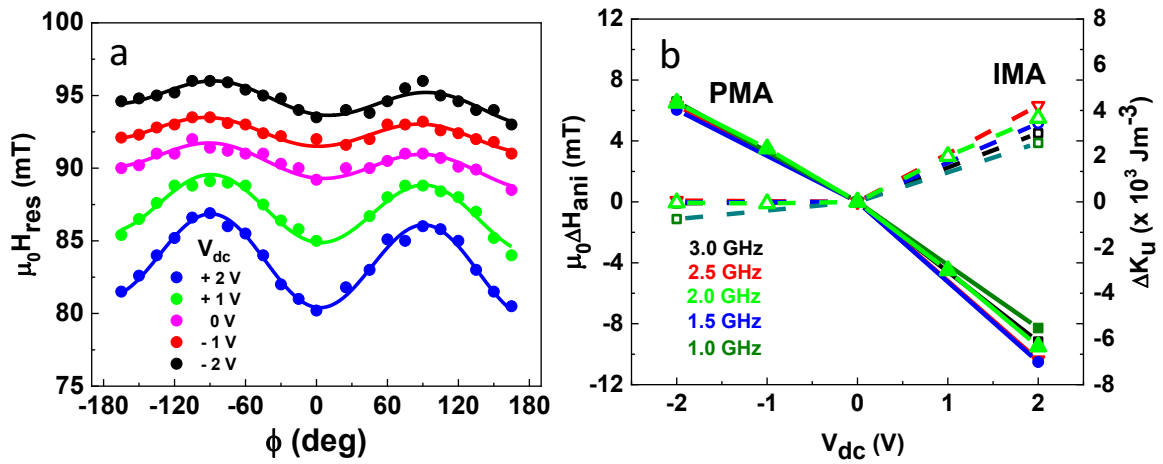


Figure 5.6 a, In plane angle ϕ dependence of H_{res} at different V_{dc} at $f = 2.0$ GHz. The lines are fits to experimental data using Eq. (3.8). **b**, The change of anisotropy fields $\mu_0 \Delta H_{ani}$ (symbols with lines) with respect to V_{dc} is shown on the left while the corresponding change in energies ΔK_u is shown on the right axis. PMA and IMA refer to perpendicular and in-plane magnetic anisotropy respectively.

5.3. Angular dependence of torque on magnetization and rectified voltages from spin pumping

As discussed in Section 5.1, an ability to control the in-plane component of magnetic anisotropy could enable us to have a non-zero torque without the need to tilt the magnetization direction from its easy state. With this purpose, we derive the expression for the torque arising from VCMA of both H_p and H_k in this section. In order to gain a comparative picture, the torques from x-, y- and z- axial microwave fields are also estimated. Subsequently, we fit these torque expressions in the spin pumping model to obtain the angular dependence of rectified voltages arising from spin pumping and inverse spin Hall effect experiments.

The torque on the unit magnetization vector m can be estimated using the following relation:

$$\tau \propto \hat{m} \times H_{eff}, \quad (5.2)$$

where \hat{m} has the components $(\cos\theta\cos\phi, \cos\theta\sin\phi, \sin\theta)$ and H_{eff} is the effective magnetic field given by the differential of magnetic free energy F as follows:

$$H_{eff} = \frac{1}{\mu_0 M} \frac{\partial F}{\partial \hat{m}}. \quad (5.3)$$

The generalized expression of F can be written as the sum of Zeeman, demagnetizing and anisotropy energies.

$$F = \frac{\mu_0 M_s}{2} \left[-2H_{ex} (\cos\theta \cos\beta \cos(\alpha - \phi) + \sin\theta \sin\beta) + (M_s - H_p) \sin^2 \theta \right] - H_k \cos^2 \phi \cos^2 \theta, \quad (5.4)$$

For the sake of simplicity, let us consider only the terms that have a time dependent characteristic as follows:

$$F = \frac{\mu_0 M}{2} \left[-\frac{\partial H_p}{\partial V} V_{rf} m_z^2 - \frac{\partial H_k}{\partial V} V_{rf} m_x^2 + h_{rf,x} m_x + h_{rf,y} m_y + h_{rf,z} m_z \right], \quad (5.5)$$

where $\frac{\partial H_p}{\partial V} V_{rf}$ and $\frac{\partial H_k}{\partial V} V_{rf}$ are the voltage modulated parts of H_p and H_k respectively, $h_{rf,x}$, $h_{rf,y}$ and $h_{rf,z}$ are the x-, y- and z-axial microwave fields and m_x , m_y and m_z are the x-, y- and z-components of \hat{m} . Due to the electric-field effect on the anisotropy fields, we can assume the anisotropy fields as the sum of $H_{ani} = (H_{ani})_{V=0} + \frac{\partial H_{ani}}{\partial V} V_{rf}$, where the first term is the anisotropy in the unbiased condition i.e $V = 0$, while the second term accounts for the voltage modulated increase or decrease of H_p or H_k due to a microwave voltage of amplitude V_{rf} . Using Eq. (5.3) and the VCMA terms of Eq. (5.5), we can estimate the torque arising from VCMA of both H_p and H_k from Eq. (5.2) as:

$$\tau_{VCMA} \propto \begin{bmatrix} -\frac{\partial H_p}{\partial V} V_{rf} \sin \phi \sin \theta \cos \theta \\ \left(\frac{\partial H_p}{\partial V} - \frac{\partial H_k}{\partial V}\right) V_{rf} \cos \phi \sin \theta \cos \theta \\ \frac{\partial H_k}{\partial V} V_{rf} \sin \phi \cos \phi \cos^2 \theta \end{bmatrix}. \quad (5.6)$$

Following a similar process for the third, fourth and fifth terms of Eq. (5.5), we can obtain the following relations for torques arising from x-, y- and z-axial microwave fields:

$$\tau \propto \frac{h_{rf,x}}{2} \begin{bmatrix} 0 \\ \sin \theta \\ -\cos \theta \sin \phi \end{bmatrix}, \quad (5.7)$$

$$\tau \propto \frac{h_{rf,y}}{2} \begin{bmatrix} -\sin \theta \\ 0 \\ \cos \theta \cos \phi \end{bmatrix}, \quad (5.8)$$

$$\tau \propto \frac{h_{rf,z}}{2} \begin{bmatrix} -\cos \theta \sin \phi \\ \cos \theta \cos \phi \\ 0 \end{bmatrix}, \quad (5.9)$$

The Eqs. (5.6) – (5.9) have been plotted as three dimensional colour maps in Fig. 5.7.

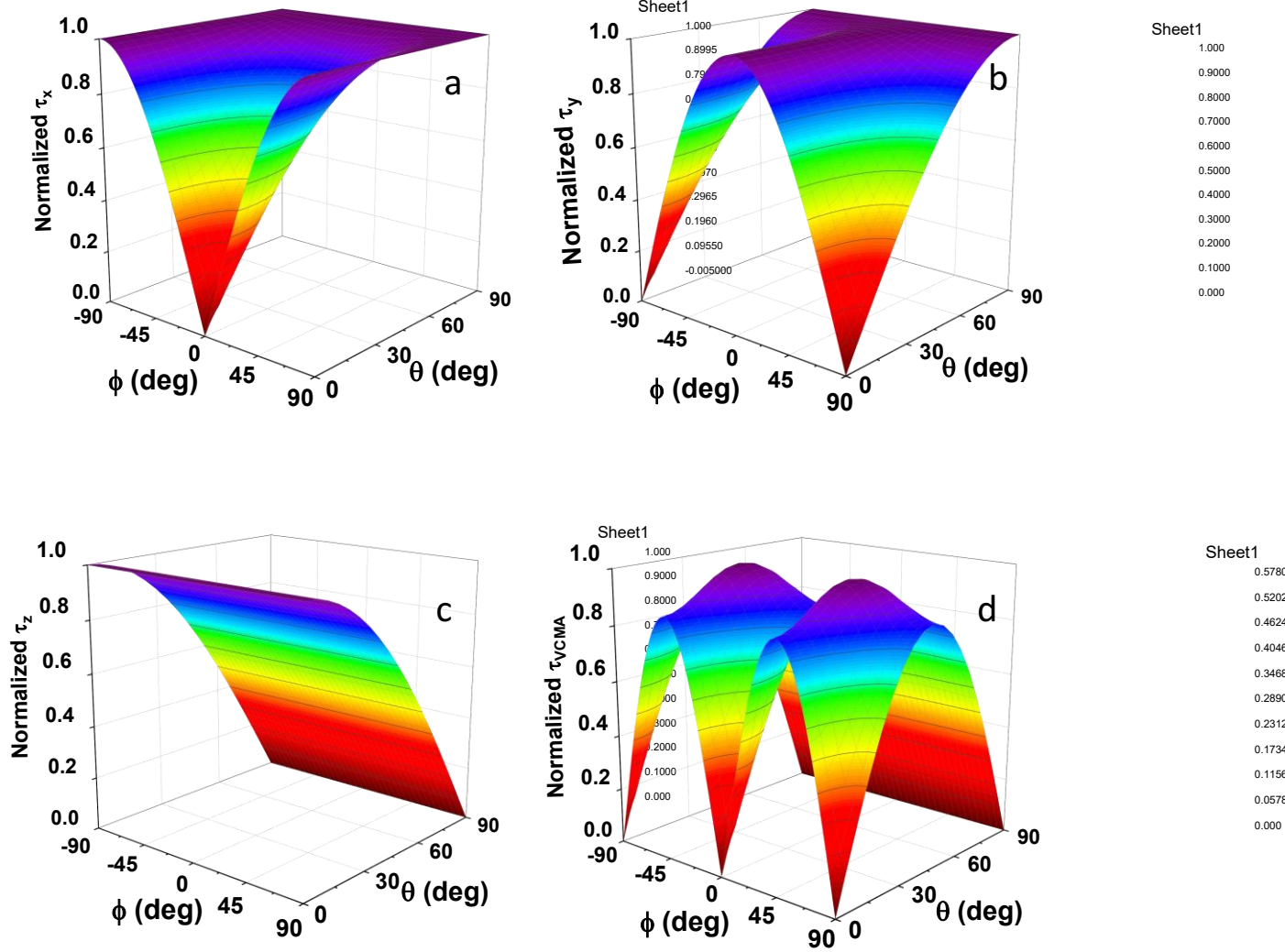


Figure 5.7 The angular dependence of normalized torque τ arising from **a**, $h_{rf,x}$ **b**, $h_{rf,y}$ **c**, $h_{rf,z}$ and **d**, voltage controlled magnetic anisotropy (VCMA) of H_p and H_k . Equations used for simulating the plots are Eqs. (5.7), (5.8), (5.9) and (5.6) respectively.

From the theory of spin pumping, DC component of inverse spin Hall effect voltage V_{ISHE} in our device geometries is given by $V_{\text{ISHE}} = A\theta_c^2 \cos\phi \cos\theta$ [29]. Here, θ_c is the precession cone angle and

$$A = -\frac{\theta_{\text{SH}} e f \lambda_{\text{sd}} L_{\text{Ta}} g^{\uparrow\downarrow}}{\sigma_{\text{Ta}} t_{\text{Ta}}} \tanh\left(\frac{t_{\text{Ta}}}{2\lambda_{\text{sd}}}\right),$$

e being the charge of electron, f is frequency of applied microwave signal, $g^{\uparrow\downarrow}$ is the spin mixing conductance of CoFeB/Ta interface, λ_{sd} , σ_{Ta} , t_{Ta} and L_{Ta} are spin diffusion length, conductance, thickness and length of Ta strip. The expression for A assumes a circular precession of magnetization which is possible in the low excitation power regime. Precession cone angles are strongly dependent on the torque on magnetization. Assuming a linear relationship between the two in the linear excitation regime, i.e. $\theta_c = \eta \tau$, we can obtain the following expression for the angular dependent behavior if V_{ISHE} originates from electric-field induced FMR $V_{\text{ISHE,VCMA}}$:

$$V_{\text{ISHE,VCMA}} = AV_{\text{rf}}^2 \left(\left(\frac{\partial H_p}{\partial V} \sin\phi \sin\theta \right)^2 + \left(\left(\frac{\partial H_p}{\partial V} - \frac{\partial H_k}{\partial V} \right) \cos\phi \sin\theta \right)^2 + \left(\frac{\partial H_k}{\partial V} \sin\phi \cos\phi \cos\theta \right)^2 \right) \cos\phi \cos^3\theta. \quad (5.10)$$

Following a similar process, we can obtain the corresponding relations for V_{ISHE} arising out $h_{\text{rf,x}}$, $h_{\text{rf,y}}$ and $h_{\text{rf,z}}$ as follows:

$$V_{\text{ISHE,hx}} = A \frac{h^2}{4} (\sin^2\theta + \cos^2\theta \sin^2\phi) \cos\phi \cos\theta, \quad (5.11)$$

$$V_{\text{ISHE,hy}} = A \frac{h^2}{4} (\sin^2\theta + \cos^2\theta \cos^2\phi) \cos\phi \cos\theta, \quad (5.12)$$

$$V_{\text{ISHE,hz}} = A \frac{h^2}{4} \cos\phi \cos^3\theta. \quad (5.13)$$

The normalized angular dependences of V_{ISHE} arising out of the equations derived above have been plotted in Fig. 5.8. One of the most interesting aspects observed in Fig. 5.8d is that the VCMA of H_k can give rise to a non-zero V_{ISHE} , which is not possible with the voltage modulation of only H_p .

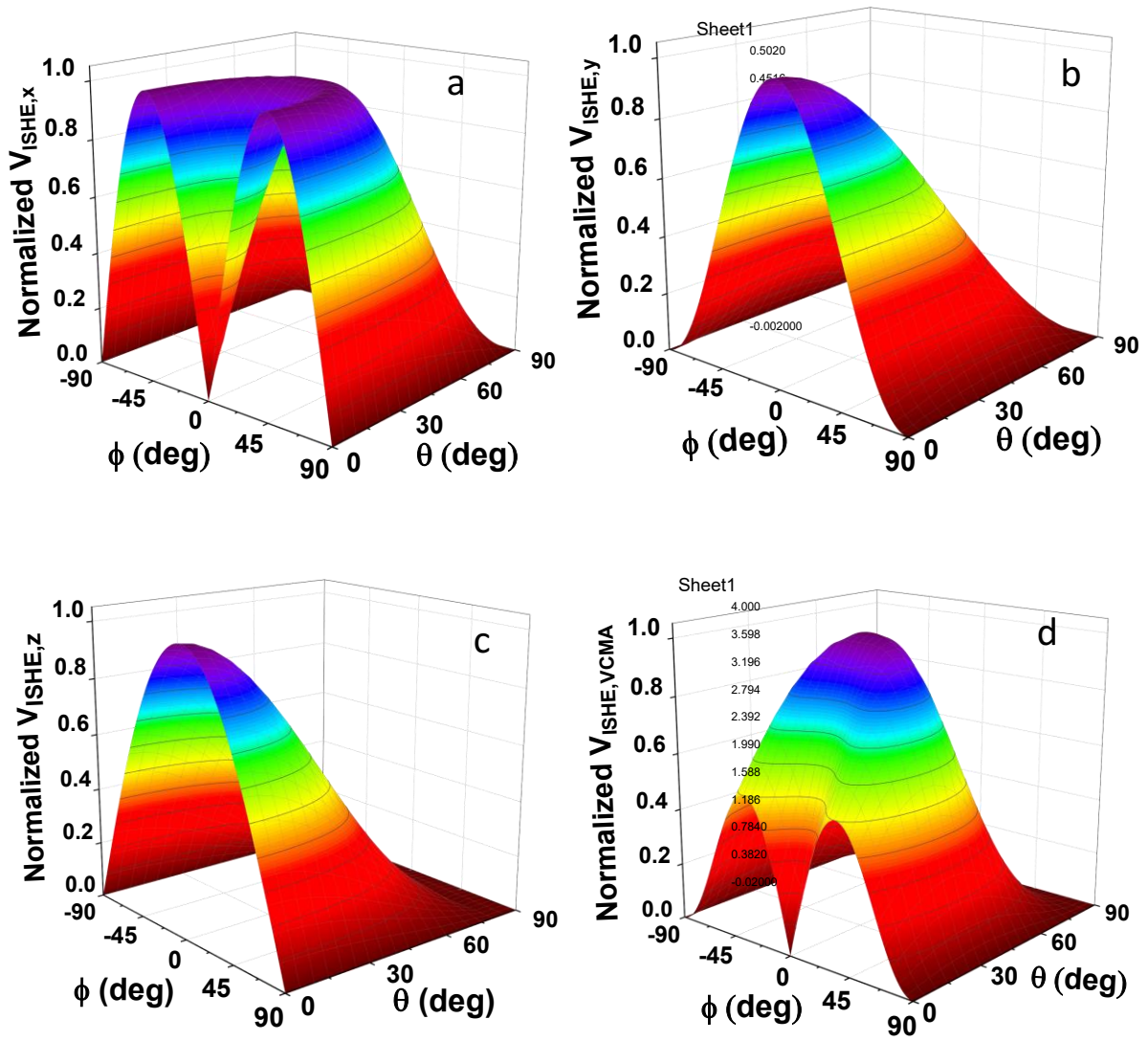


Figure 5.8 The angular dependence of normalized inverse spin Hall effect voltages V_{ISHE} expected from **a**, $h_{rf,x}$ **b**, $h_{rf,y}$ **c**, $h_{rf,z}$ and **d**, voltage controlled magnetic anisotropy (VCMA) of H_p and H_k . Equations used for simulating the plots are Eqs. (5.11), (5.12), (5.13) and (5.10) respectively.

5.4. Field distribution in CoFeB/MgO junctions due to microwave voltages

Microwave electric-fields ferromagnetic metal/oxide junctions can also give rise to additional Oersted fields as has been observed in earlier studies [14]. Therefore, we performed finite element method (FEM) analysis using COMSOL Multiphysics simulator [30] in order to understand the field distributions of our device structures, upon the application of a microwave electric-field at the CoFeB/MgO interface. As described in Section 2.6, the multilayer structure used is Ta/CoFeB/MgO/Al₂O₃, similar to the experimental device multilayer structure. Figure 5.9a shows the typical structure used for the simulation purposes, where the sample is divided in mesh of dimension 10 nm. Figure 5.9b shows the corresponding electric-field distribution as a function of thickness when a microwave power is applied across the junction. It shows that the electric-field is restricted to the CoFeB/MgO interface and is zero inside the Ta/CoFeB metallic layers. As shown by the arrows in the same figure, it also reveals the presence of x- and y-axial Oersted field contributions arising from the microwave electric-fields, while the z-axial Oersted fields are zero. Such magnetic fields should be taken into account, in addition to voltage controlled magnetic anisotropy, in order to completely understand the rectified voltages arising from electric-field induced magnetization dynamics in devices. As further shown in Fig. 5.9c-e, we see that the ratio of the x- and y-axial microwave fields are strongly dependent on the dimension of the devices. For the devices used in the experiments reported in the following section for electric-field induced magnetization dynamics, we use a device which has $l:w = 12:1$, the Oersted fields along the shorter in-plane dimension are very small compared to those oriented along the longer one i.e. $h_{rf,x} \ll h_{rf,y}$.

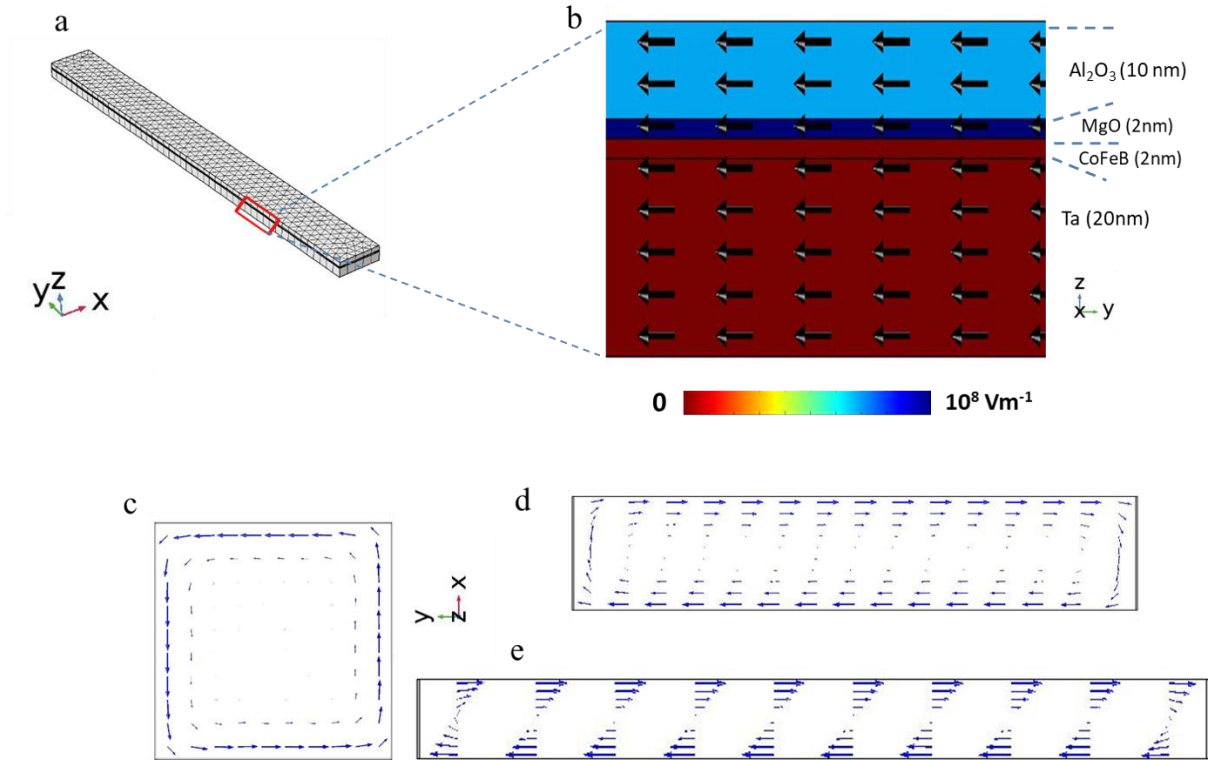


Figure 5.9 **a**, 20 nm Ta/ 2 nm CoFeB/ 2 nm MgO/ 10 nm Al₂O₃ multilayer structure of size $1 \times 0.1 \mu\text{m}^2$ discretized into triangular mesh elements of size around 10 nm. **b**, Electric-field distribution in the multilayer structure when a power of $10 \mu\text{W}$ is applied on the top surface is color coded as a function of the thickness while the corresponding magnetic field induced due to the applied power is shown as arrows. Normalized Oersted field distribution (arrows) is shown for samples with $l:w =$ **c**, 1:1 **d**, 1:5 and **e**, 1:10.

In addition, the effect of input power on the magnetic and electric field distributions were also investigated. Such a study is especially important in order to understand the dynamical non-linear magnetization processes because, microwave signals can induce magnetic fields which can significantly affect the process of spin pumping. Figure 5.10 shows the effect of an input power on the magnetic field distributions in the CoFeB layer, when the frequency is fixed at 3 GHz. An increase in the $h_{rf,y}$ is observed which can be expected because the corresponding current density induced in the CoFeB layer due to the microwave signal increases.

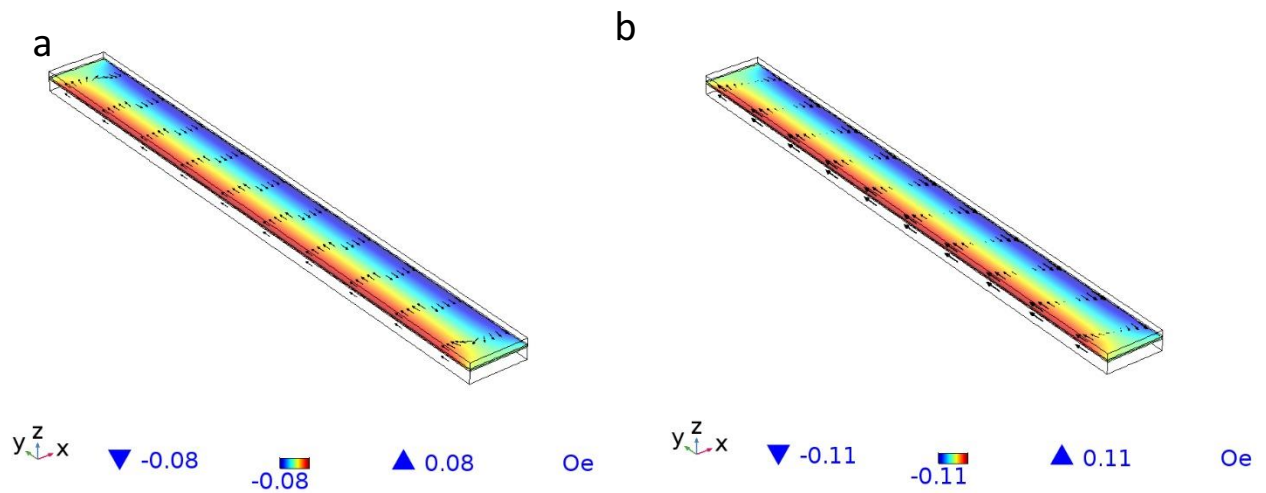


Figure 5.10 Oersted field distribution shown by the arrows for an input frequency of 3 GHz **a**, 0.025 mW and **b**, 0.05 mW. The cross section of y-axis Oersted field in the CoFeB layer is shown as a color map with the maximum values indicated in the color scale below.

Following this, we investigated the effect of an input frequency on the magnetic field distributions. Figure 5.11 shows that the strength of $h_{rf,y}$ increases with increasing frequency. This can be attributed to an increase in the current densities with frequency owing to a reduction in the impedance of the device structure. It should be noted that in both Fig. 5.10 and 5.11, the maximum values are shown only to indicate the increase or decrease with power and frequency respectively. They are not same as the absolute values in the devices.

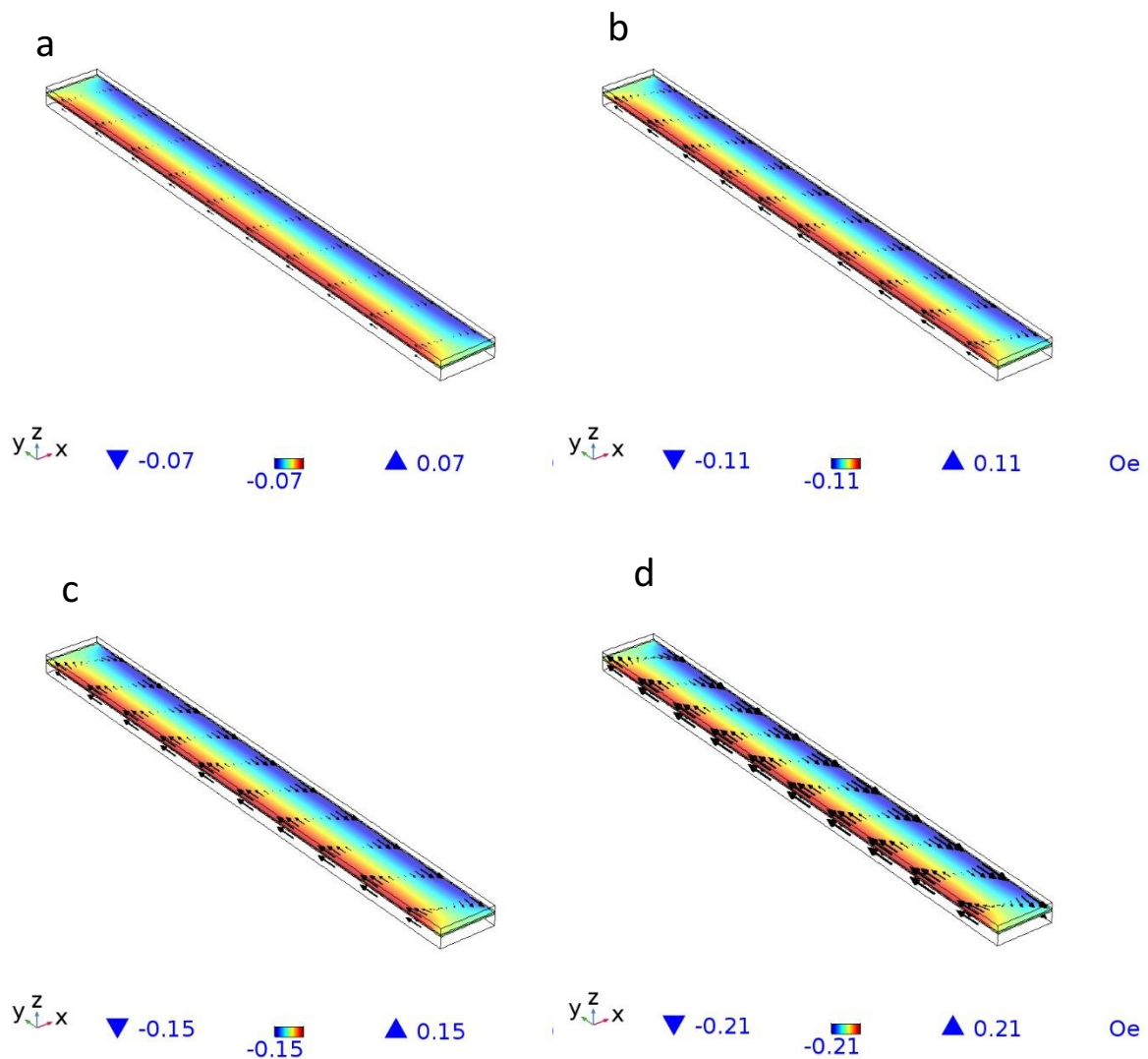


Figure 5.11 Oersted field distribution shown by the arrows for an input power of 0.05 mW for frequencies **a**, 1 GHz **b**, 3 GHz **c**, 5 GHz and **d**, 10 GHz. The cross section of y-axial Oersted field in the CoFeB layer is shown as a color map with the maximum values indicated in the color scale below.

5.5. Excitation of magnetization dynamics using electric-fields

For the excitation of FMR using electric-fields and subsequent detection, a microwave voltage V_{ac} was applied in the CoFeB/MgO junction, while an in-plane magnetic field was swept from -250 mT to $+250$ mT. The corresponding experimental setup is shown in Fig. 5.12a. The microwave voltage V_{ac} modulates the magnetic free energy of the system, which acts as an oscillating field in the subnanosecond regime. This gives rise to FMR, thereby giving us a non-zero rectified voltage that is detected across the Ta/Ru/Ta underlayer, as shown in Fig. 5.12b. In order to obtain the resonance field H_{res} , the rectified voltage is fitted using Eq. (5.1). The monotonous increase of H_{res} with increasing frequency in Fig. 5.12b, is consistent with the Kittel formula. Following our analysis in Section 5.2, we can ignore the effect of AMR and AHE in this thin film stack. This allows us to attribute the origin of this rectified voltage to SP-ISHE. During FMR excitation spin current J_s is pumped from the CoFeB layer into the Ta layer. Due to the spin Hall effect of Ta, this spin current is converted into charge current J_c that gives us a non-zero rectified voltage V_{ISHE} .

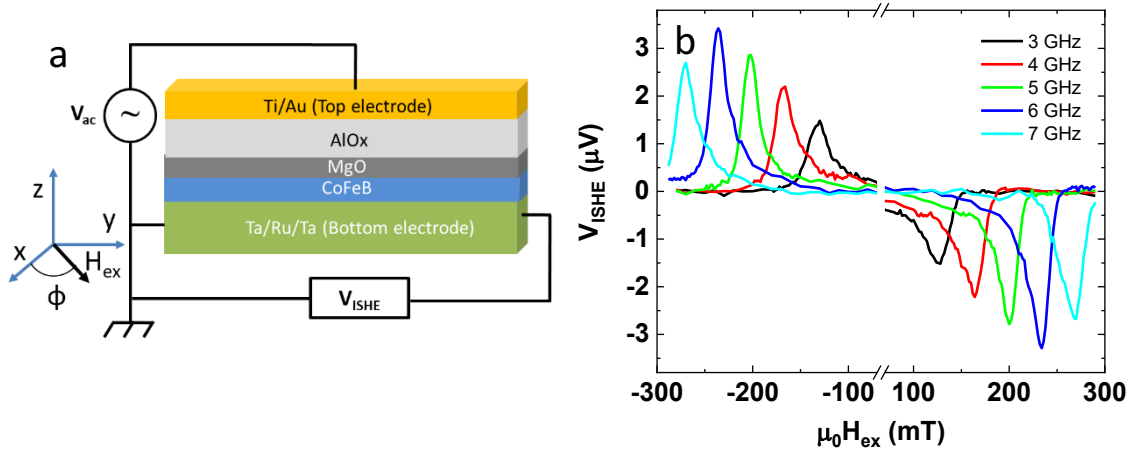


Figure 5.12 a, Experimental set up showing the multilayer structure and application of microwave voltage V_{ac} across top and bottom electrodes. V_{ISHE} is detected across the the Ta/Ru/Ta underlayer i.e. bottom electrodes. **b**, V_{ISHE} obtained from the electric-field controlled devices as a function of the frequency of V_{ac} .

In order to determine the origin of the underlying FMR in the process of electric-field induced spin pumping, we perform an angular dependent study of the V_{ISHE} amplitudes. Figure 5.13a shows the in-plane angle dependence of the normalized V_{ISHE} when FMR is excited using electric-fields in our devices. One interesting feature of this angular dependence is that although the V_{ISHE} is maximum around $\phi = 35$ degree, it is not zero for $\phi = 0$ degree as is expected from the VCMA of H_k shown previously in Fig. 5.8d. A non-zero voltage along $\theta = \phi = 0$ degree can arise from y- and z- axial Oersted fields contribution in our device as can be understood from Fig. 5.8b and 5.8c. In the previous section finite element method (FEM) analysis using COMSOL Multiphysics simulator were presented to show the field distributions of our device structures. It reveals the presence of x- and y-axial Oersted field contributions arising from the microwave electric-fields, while the z-axial Oersted fields are zero. This shows that the non-zero voltage along $\theta = \phi = 0$ degree is due to $h_{\text{rf},y}$. We see that for our devices which have $l:w = 12:1$, the Oersted fields along the shorter in-plane dimension are very small compared to those oriented along the longer one i.e. $h_{\text{rf},x} \ll h_{\text{rf},y}$. Additionally it also indicates that the ϕ dependence of the V_{ISHE} amplitudes arises either from a combined effect of $h_{\text{rf},x}$ and $h_{\text{rf},y}$ or a combination of VCMA of H_k and $h_{\text{rf},y}$. The in-plane angle dependence of each of these cases can be obtained from Eq. (5.7)-Eq. (5.10) as follows:

$$V_{\text{ISHE},\phi} = A \left(h_{\text{rf},x}^2 \sin^2 \phi \cos \phi + h_{\text{rf},y}^2 \cos^3 \phi \right), \quad (5.14)$$

$$V_{\text{ISHE},\phi} = A \left(4 \left(\frac{\partial H_k}{\partial V} V_{\text{rf}} \right)^2 \sin^2 \phi + h_{\text{rf},y}^2 \right) \cos^3 \phi. \quad (5.15)$$

Equation (5.14) can give us the observed angular dependence only if $Ah_{\text{rf},x}^2 > Ah_{\text{rf},y}^2$. However, from the FEM analysis, we can see that such a condition is not possible for our device geometry because $h_{\text{rf},x} \ll h_{\text{rf},y}$. The data in Fig. 5.13a are fitted using Eq. (5.15) with the values $4A \left(\frac{\partial H_k}{\partial V} V_{\text{rf}} \right)^2 = 2$ and $Ah_{\text{rf},y}^2 = 0.8$. The elevation angle dependence of V_{ISHE} amplitudes is also studied to further confirm this observation. Figure 5.13b shows the normalized V_{ISHE} as a function of θ when $\phi = 0$ degree. Since we

had estimated $h_{rf,x} \ll h_{rf,y}$, we can once again eliminate the possibility of $h_{rf,x}$ contribution. Using Eq.(5.10) and (5.12) we can obtain the following elevation angle dependence when $\phi = 0$ degree:

$$V_{ISHE,\theta} = A \left(4 \left(\frac{\partial H_p}{\partial V} - \frac{\partial H_k}{\partial V} \right)^2 V_{rf}^2 \sin^2 \theta \cos^2 \theta + h_{rf,y}^2 \right) \cos \theta. \quad (5.16)$$

The data in Fig. 5.13b are fitted to this Eq.(5.16) using the values $4A \left(\frac{\partial H_p}{\partial V} - \frac{\partial H_k}{\partial V} \right)^2 V_{rf}^2 = 2.1$ and $Ah_{rf,y}^2 = 0.8$. Based on this analysis we can conclude that the observed electric-field induced FMR in our devices is due to a combination of VCMA and Oersted fields generated from the microwave electric-fields. More importantly, it shows that the in-plane magnetic anisotropy can be modulated by an AC voltage, which in turn contributes towards excitation of magnetization dynamics in an in-plane magnetized CoFeB/MgO junction.

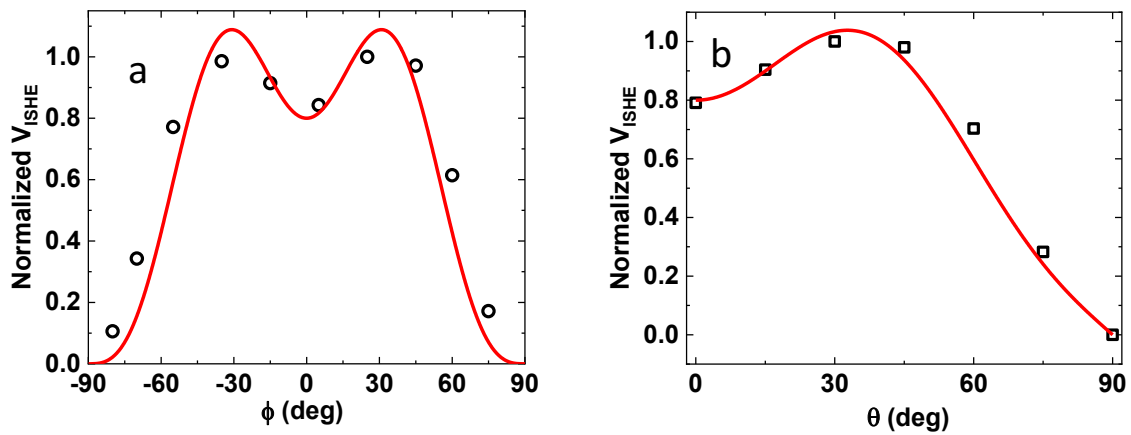


Figure 5.13 Dependence of normalized V_{ISHE} on **a**, azimuthal angle ϕ and **b**, elevation angle θ . Lines are fits using Eqs. (5.15) and (5.16) respectively.

5.6. Conclusion:

To summarize this chapter, spin pumping measurements were performed on Ta/Ru/Ta/CoFeB/MgO multilayers which was detected using inverse spin Hall effect of Ta. Electric-field can modulate the resonant field. Since the gyromagnetic ratio was found to be constant in our measurement range, we can attribute this change to voltage controlled magnetic anisotropy. We have shown that in addition to interfacial perpendicular magnetic anisotropy, an in-plane magnetic anisotropy can also be modulated by a DC gate voltage [31]. The negative bias voltage increases perpendicular magnetic anisotropy, on the other hand, the positive bias voltage decreases perpendicular magnetic anisotropy and increases the in-plane induced uniaxial magnetic anisotropy. This behavior is understood by a change of electron density for the in-plane and out-of-plane $3d$ orbitals of the ferromagnetic metal in the presence of electric-field at the CoFeB/MgO junction.

So far, magnetization switching and excitation are reported for magnetization direction tilted with the application of magnetic field which is not in-plane and out-of-plane direction of the sample. However, we demonstrate that ferromagnetic resonance and spin pumping can be induced by electric-field modulation of H_k and H_p in an in-plane magnetized CoFeB layer in the GHz frequency regime. We believe that such a control of symmetry of the magnetic anisotropy by magnetic annealing and its control by gate voltage is a crucial development towards realizing purely voltage-controlled spintronic devices with ultralow power consumption.

References

1. J. S. Slonczewski, *J. Magn. Magn. Mater.* **159**, L1-L7 (1996).
2. L. Berger, *Phys. Rev. B* **54**, 9353-9358 (1996).
3. I. M. Miron, K. Garello, G. Gaudin, P.-J. Zermatten, M. V. Costache, S. Auffret, S. Bandiera, B. Rodmacq, A. Schuhl and P. Gambardella, *Nature* **476**, 189-193 (2011).
4. L. Liu, T. Moriyama, D.C. Ralph and R.A. Burhman, *Phys. Rev. Lett.* **106**, 036601 (2011).
5. S. Fukami, T. Anekawa, C. Zhang and H. Ohno, *Nat. Nanotechnol.* **11**, 621-625 (2016).
6. H. Fulara, M. Zahedinejad, R. Khymyn, A.A. Awad, S. Muralidhar, M. Dvornik and J. Akerman, *Science Advances* **5**, 9, eaax8467 (2019).
7. T. Nozaki, Y. Shiota, S. Miwa, S. Murakami, F. Bonell, S. Ishibashi, H. Kubota, K. Yakushiji, T. Saruya, A. Fukushima, S. Yuasa, T. Shinjo and Y. Suzuki, *Nat. Phys.* **8**, 491-496 (2012).
8. F. Matsukura, Y. Tokura and H. Ohno, *Nat. Nanotechnol.* **10**, 209-220 (2015).
9. M. Weisheit, S. Fahler, A. Marty, Y. Souche, C. Poinignon and D. Givord, *Science* **315**, 349-351 (2007).
10. S. S. P. Parkin, C. Kaiser, A. Panchula, P.M. Rice, B. Hughes, M. Samant and S-H. Yang, *Nat. Mater.* **3**, 862-867 (2004).
11. S. Yuasa, T. Nagahama, A. Fukushima, Y. Suzuki and K. Ando, *Nat. Mater.* **3**, 868-871 (2004).
12. S. Ikeda, K. Miura, H. Yamamoto, K. Mizunuma, H.D. Gan, M. Endo, S. Kanai, J. Hayakawa, F. Matsukura and H. Ohno, *Nat. Mater.* **9**, 721-724 (2010).
13. Y. Shiota, T. Nozaki, F. Bonell, S. Murakami, T. Shinjo and Y. Suzuki, *Nat. Mater.* **11**, 39-43 (2012).
14. J. Zhu, J.A. Katine, G. E. Rowlands, Y.-J. Chen, Z. Duan, J.G. Alzate, P. Upadhyaya, J. Langer, P.K. Amiri, K.L. Wang and I.N. Krivorotov, *Phys. Rev. Lett.* **108**, 197203 (2012).
15. C. Grezes, F. Ebrahimi, J.G. Alzate, X. Cai, J.A. Katine, J. Langer, B. Ocker, P.K. Amiri and K.L. Wang, *Appl. Phys. Lett.* **108**, 012403 (2016).
16. S. Kanai, F. Matsukura and H. Ohno, *Appl. Phys. Lett.* **108**, 192406 (2016).
17. K. Miura, S. Yabuuchi, M. Yamada, M. Ichimura, B. Rana, S. Ogawa, H. Takahashi, Y. Fukuma and Y. Otani, *Sci. Rep.* **7**, 42511 (2017).
18. B. Rana, Y. Fukuma, K. Miura, H. Takahashi and Y. Otani, *Appl. Phys. Lett.* **111**, 052404 (2017).
19. P. Bruno, *Phys. Rev. B* **39**, 865 (1989).
20. H.X. Yang, M. Chshiev, B. Dieny, J.H. Lee, A. Manchon and K.H. Shin, *Phys. Rev. B* **84**, 054401 (2011).
21. R. Verba, V. Tiberkevich, I. Krivorotov and A. Slavin, *Phys. Rev. Appl.* **1**, 044006 (2014).
22. Y.-J. Chen, H. K. Lee, R. Verba, J. A. Katine, I. Barsukov, V. Tiberkevich, J. Q. Xiao, A. N. Slavin, and I. N. Krivorotov, *Nano Lett.* **17**, 572 (2017).

23. R. Verba, M. Carpentieri, G. Finocchio, V. Tiberkevich and A. Slavin, *Phys. Rev. Appl.* **7**, 064023 (2017).
24. M. Harder, Y. Gui, and C.-M. Hu, *Phys. Rep.* **661**, 1-59 (2016).
25. S. Gupta, R. Medwal, D. Kodama, K. Kondou, Y. Otani and Y. Fukuma, *Appl. Phys. Lett.* **110**, 022404 (2017).
26. J.M. Shaw, H.T. Nembach, T.J. Silva and C.T. Boone, *J. Appl. Phys.* **114**, 243906 (2013).
27. T. Maruyama, Y. Shiota, T. Nozaki, K. Ohta, N. Toda, M. Mizuguchi, A.A. Tulapurkar, T. Shinjo, M. Shiraishi, Y. Ando and Y. Suzuki, *Nat. Nanotechnol.* **4**, 158-161 (2009).
28. R. Shimabukuro, K. Nakamura, T. Akiyama and T. Ito, *Phys. E* **42**, 1014-1017 (2010).
29. H. Zhou, X. Fan, L. Ma, Q. Zhang, L. Cui, S. Zhou, Y.S. Gui, C.-M. Hu and D. Xue, *Phys. Rev. B* **94**, 134421 (2016).
30. COMSOL Multiphysics Reference Manual, version 5.3", COMSOL, Inc, www.comsol.com
31. A. Deka, B. Rana, R. Anami, K. Miura, H. Takahashi, Y. Otani and Y. Fukuma, *Phys. Rev. B* **101**, 174405 (2020).

Chapter 6

Efficient generation of spin current and excitation of parametric resonance using electric fields.

6.1. Introduction

In the previous chapter, the electric-field induced control of magnetization was discussed where using the voltage control of magnetic anisotropy (VCMA), magnetization dynamics was shown to be excited in CoFeB/MgO junctions. Of particular importance was the demonstration of ferromagnetic resonance (FMR) in an in-plane magnetized junction which was achieved using VCMA of in-plane magnetic anisotropy (IMA). Such a control of magnetization has immense potential in the realization of magnetic field free control of magnetization which is one of the most researched avenues towards power efficient spintronic logic devices. The basic mechanism of such an FMR excitation technique using VCMA is illustrated in Figure 6.1 below.

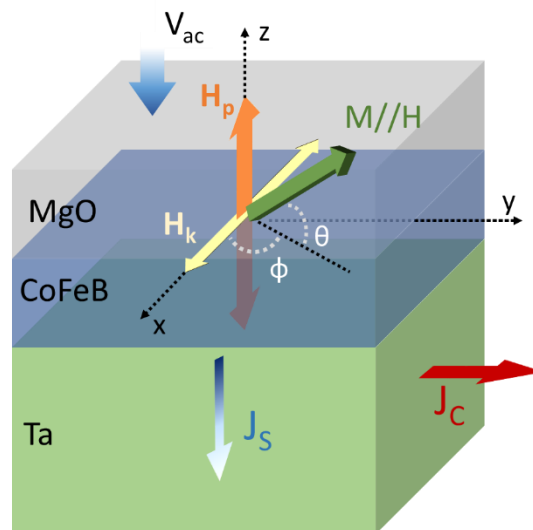


Figure 6.1, Schematic of the orientation of the perpendicular magnetic anisotropy H_p , in-plane magnetic anisotropy H_k , elevation angle θ , azimuthal angle ϕ , spin current generated due to spin pumping from CoFeB J_s and charge current generated due to inverse spin Hall effect (ISHE) of Ta J_c .

Efficient generation of spin current, which is the flow of spin angular momentum of electrons, is a crucial area of research in the field of spintronics because effect of Joule heating increases due to large charge current density in the nano-dimensions. Generation of spin current has been targeted from various mechanisms such as spin Hall effect [1] or non-local spin injection technique [2]. Additionally, it was demonstrated that temperature gradients in ferromagnets can be used to generate spin currents via spin Seebeck effect [3]. Yet another technique to generate spin current is via spin pumping wherein magnetization dynamics inside a ferromagnet can be used to emit spin current [4]. The advantage of spin pumping is that the excitation of magnetization dynamics can be achieved using electric-fields in ferromagnetic metal-oxide junctions [5-7]. Such a feature of spin pumping promises to make it a low power alternative for efficient spin current generation.

In addition, to spin currents, the ability to excite spin waves using electric-fields also has a great potential in the field of ultralow power spintronic devices [8-10]. Spin wave are collective excitation of magnetic moments, known quantum mechanically as magnons. Such excitations can also be utilized to overcome the need for flowing electronic charge during information transfer [11]. The advantage of spin waves over spin currents lies in their larger decay lengths. Spin waves in metallic ferromagnets, on the other hand, have been shown to exist up to distances over several micrometers and in insulators upto several millimeters [12-13]. The larger decay lengths of spin wave in insulators is attributed to the lack of scattering of the magnons by conducting electrons. Conventionally propagating spin wave modes in ferromagnetic thin films have been mostly realized by localized magnetization excitations using charge currents and, more recently, electric-fields [14-15,7]. However, a major limitation of such excitations lies in the fact that wavelengths are strongly limited by the size of the excitation area used in the processes. Typically, the corresponding wavelengths generated from such processes can be tuned down to the μm regime, which corresponds to the dipole-exchange wavelength spectra. Therefore, for applications in the field of nanoscale devices, it becomes imperative for us to find alternative techniques for exciting magnons with shorter wavelengths. In this regard, parametric excitation of ferromagnetic resonance has emerged to be a potential solution for exciting spin waves with wavelengths down to the exchange interaction length scales [17-20].

Parametric resonance modes have been typically excited using Oersted fields and have been more extensively studied in magnetic insulators such as YIG than the metallic ferromagnets. This is partially because of the relatively higher damping in metallic ferromagnets compared to their insulating counterparts, which in turn increases the threshold power required for parametric FMR mode excitation in the former [21]. Additionally, the need for higher excitation power gives rise to Joule heating, which is associated with the flow of charge currents needed to generate the Oersted fields. Therefore, just as electric-fields can be used for generating spin currents via spin pumping, it can also be an alternative technique to excite parametric resonance.

In Chapter 5, we discussed the electric-field induced magnetization dynamics. This chapter deals with efficiency of electric-field induced magnetization dynamics, more precisely, spin pumping and excitation of parametric resonance. Intrinsic properties like resistivity of Ta has been shown to be dominant in determining the spin to charge interconversion via spin Hall effect [22]. Additionally, interface engineering by MgO insertion between NiFe and Ag layers was shown to greatly improve spin current generation in lateral spin valves [23]. Such studies demonstrate that in addition to the factors such as external field and applied power, internal parameters are just as important in determining efficiency of spin current generation from ferromagnetic nanostructures. As is evident from the mechanism of spin pumping, trajectories during excitation of magnetization dynamics play an important role in determining the amount of spin current generated during the process. In addition to spin pumping, the trajectories also determine the excitation efficiency of spin waves and emission power of spin torque oscillators. Although magnetization trajectories can be controlled to a great extent by the amplitudes of static and oscillating fields [24-26], two major internal factors that limit the dynamical magnetization components are the demagnetizing and magnetic anisotropy fields. As discussed in the previous chapter, electric-fields can control the effective demagnetizing fields in metallic ferromagnets via voltage controlled magnetic anisotropy (VCMA) [27].

In the first part of this chapter, the effect of PMA on dynamical magnetization trajectories during FMR is presented. The magnetization trajectories are estimated using micromagnetic simulations. It is

found that when the demagnetizing field is almost overcome by the PMA, the area under the magnetization trajectory is found to be maximum. The corresponding easy axis is in the film plane and the ellipticity of the magnetization trajectory is ~ 0.5 . Since the spin current generation is the transfer of spin angular momentum from the ferromagnet, its generation efficiency depends on this area of magnetization trajectory. So following the results of our simulations, we fabricated devices with comparable effective demagnetizing field like the simulations. Spin current densities upto $\sim 1.5 \times 10^9$ Am⁻² is found to be generated in our electric-field controlled devices. Interestingly, the corresponding J_s for current controlled devices of equal dimensions are over 2 orders smaller. The rectified voltage spectra are studied as a function of input power. It showed significant change of the V_{ISHE} spectra in the non-linear regime. Most importantly, it was seen that parametric resonance peak emerged at higher excitation powers. Using a combination of lineshape analysis at high excitation powers and angular dependent behavior of parametric resonance amplitude, we can attribute the origin of such a parametric resonance excitation to the VCMA of IMA. Finally, in the concluding section, we will discuss about the importance of these findings and how they address the motivation behind this thesis in terms of potential spintronic devices in future.

6.2. Dependence of magnetization trajectories on perpendicular magnetic anisotropy.

As discussed in the Section 6.1, magnetization trajectories play an important role in determining the efficient generation of spin current or parametric resonance excitation. This motivates us to study the dynamical magnetization trajectories during FMR excitation as a function of PMA using LLG micromagnetic simulator [29]. These simulations were performed using LLG micromagnetic simulator on samples of dimensions $100 \text{ nm} \times 100 \text{ nm} \times 1 \text{ nm}$ under the assumption of a macrospin model. Damping constant was taken as $\alpha = 0.02$. In order to excite FMR using frequency sweep mode, we apply an rf-magnetic field along the x-direction $\mu_0 h_{rf,x} = 0.1 \text{ mT}$ and a static external field $H_{ex,y}$ to pin the magnetization direction along the y-axis as shown in Fig. 6.2a. The frequency of the rf-magnetic field is varied from 1 to 20 GHz in steps of 0.2 GHz. For exciting FMR in the field sweep mode, a fixed frequency of 0.1 mT amplitude was applied in the x-direction while the field was swept from 0 to 400 mT in the y-direction. For the field sweep FMR simulation results presented in this paper, we have used a frequency of 9 GHz. The saturation magnetization of the sample was taken as $M_s = 1500 \text{ mT}$, while the PMA energy $K_{u,2}$ was varied from 0 to $9 \times 10^5 \text{ Jm}^{-3}$, in order to match typically reported values for CoFeB/MgO junctions [30]. Using the relation $K_{u,2} = \frac{M_s H_p}{2}$, we can estimate that the corresponding PMA fields H_p are varied from 0 to 1500 mT.

Figure 6.2b shows the resulting real and imaginary parts of the FMR spectra obtained from frequency sweep mode simulations when $K_{u,2} = 0$ and $\mu_0 H_{ex,y} = 100 \text{ mT}$. We can obtain the resonance frequency f_{res} by fitting the data using:

$$I_{FMR} = \frac{L \times df^2}{(f - f_{res})^2 + df^2} + \frac{D \times df \times (f - f_{res})}{(f - f_{res})^2 + df^2}, \quad (6.1)$$

where L and D are the Lorentzian and dispersive parts of the spectra, f_{res} is the resonance frequency and df is the linewidth of the FMR signal. Upon fitting the FMR spectra for the range of $K_{u,2}$ studied, we notice that the f_{res} varies from 11 GHz to 1 GHz as $\mu_0 H_p$ is increased from 0 to 1500 mT as shown in

Fig. 6.2c. From the H_p dependence of f_{res} , we can estimate the out-of-plane demagnetizing field for our sample as $\mu_0 H_d = 1400$ mT, using the simple form of Kittel equation:

$$f_{\text{res}} = \gamma \sqrt{(H_d - H_p + H_{\text{ex},y}) H_{\text{ex},y}}, \quad (6.2)$$

where $\gamma = 0.0298$ GHz.mT⁻¹. Ideally for thin films where the x- and y- dimensions are infinite compared to the thickness along z-axis, we have demagnetizing components $(\eta_x, \eta_y, \eta_z) = (0,0,1)$. This results in the demagnetizing field to be equal to the saturation magnetization i.e. $H_d = \eta_z M_s = M_s$ [31]. However, in nanostructures where the lateral dimensions are comparable to the thicknesses, we can have $\eta_x \neq 0$ and $\eta_y \neq 0$. Since the components of demagnetizing tensor are related by $\eta_x^2 + \eta_y^2 + \eta_z^2 = 1$, we will have $\eta_z < 1$. This can explain our observation of $\mu_0 H_d < 1500$ mT.

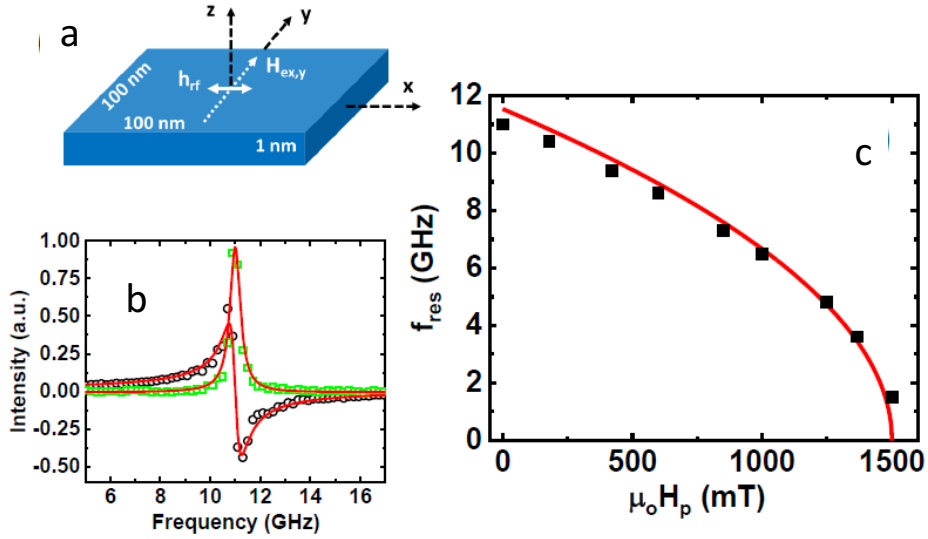


Figure 6.2 **a**, Schematic of the sample along with dimensions and directions of microwave field h_{rf} and static external field $H_{\text{ex},y}$ used for simulations. A single domain model was assumed throughout and damping constant is taken as $\alpha = 0.02$. FMR simulations are performed in frequency sweep mode. **b**, Typical FMR spectra obtained in the frequency sweep mode simulations for $\mu_0 H_{\text{ex},y} = 100$ mT, microwave amplitude $\mu_0 h_{\text{rf},x} = 0.1$ mT and perpendicular magnetic anisotropy field $\mu_0 H_p = 0$ mT. Lines are fits using Eq. (6.1). **c**, Resonance frequencies f_{res} as a function of H_p along with fit using Eq. (6.2).

Magnetic free energy of a ferromagnetic thin film is given by the sum of Zeeman, demagnetizing and anisotropy energy terms. A frequency dependent FMR study helps us to fix the Zeeman energy of the ferromagnetic system, during our investigation of the effect of PMA on the magnetization trajectories. Figure 6.3 shows the corresponding three dimensional plots when PMA is varied from $\mu_0 H_p = 0$ to $\mu_0 H_p = 1500$ mT. One of the major characteristics that we can observe from Fig. 6.3a, where $\mu_0 H_p = 0$, is that the trajectory is elliptical as seen from the x-z plane projections in the same figure. This is due to the presence of a strong effective demagnetizing field of magnitude $\mu_0 H_{d,\text{eff}} = \mu_0 H_d = 1400$ mT. Such a field restricts the movement of the magnetization in the out-of-plane direction as a result of which we obtain an elliptical trajectory with $M_z < M_x$.

The presence of PMA enables us to reduce $H_{d,\text{eff}}$ in the sample which is given by the difference of H_d and H_p . In CoFeB/MgO junctions, PMA arises due to hybridization between the $3d$ orbitals of Fe and $2p$ orbitals of O atoms at the interface [32]. Such a PMA in CoFeB/MgO junctions can be large enough to overcome H_d so that $H_{d,\text{eff}}$ becomes negative and the easy axis shifts from the in-plane to the out-of-plane direction. Figure 6.3b and 6.3c shows the trajectories when the sample has $\mu_0 H_p = 1200$ mT, 1365 mT. We can see that as the $\mu_0 H_{d,\text{eff}}$ is reduced, the z-component of the magnetization during precession increases compared to Fig. 6.3a. The increase in the z-component can be understood in terms of a reduced demagnetizing field which allows the magnetization to precess more freely around the external magnetic field. When the H_p overcomes the H_d i.e. when the easy axis of the sample is perpendicular to the film plane, the magnetization motion would be restricted in the in-plane direction. Therefore, we observe that the long axis of the ellipse changes from the in-plane direction to the out-of plane when $\mu_0 H_p = 1500$ mT as shown in Fig. 6.3d.

Magnetization components are constrained by the relation $M_x^2 + M_y^2 + M_z^2 = M_s^2$, due to which the tip of the elliptical magnetization trajectory lies on the surface of a sphere, also known as the Bloch's sphere. This results in a time dependent component of magnetization parallel to the external magnetic field M_y whose frequency is twice of the transverse magnetization components M_x and M_z , as shown in

Fig. 6.4a. It is worth mentioning here that such a component of magnetization that oscillates at twice the resonance frequency can be utilized for non-linear parametric FMR excitation. However, such effects can be neglected since our simulations are performed using a small oscillating field of 0.1 mT. The extrema of magnetization components during FMR are plotted as a function of PMA in Fig. 6.4b. The maximum deviation of magnetization in the y-axis is negligible as seen from the values of $M_{y,\min} \sim 1500$ mT in Fig. 6.4b. Therefore, the area of the elliptical trajectory on the Bloch's sphere can be assumed to be equal to that of the projection on the x-z plane. We define the ellipticity $A = m_z/m_x$ and the area of the trajectory as $\pi m_x m_z$, where m_x and m_z are the normalized values of maximum values of M_x and M_z with respect to M_s .

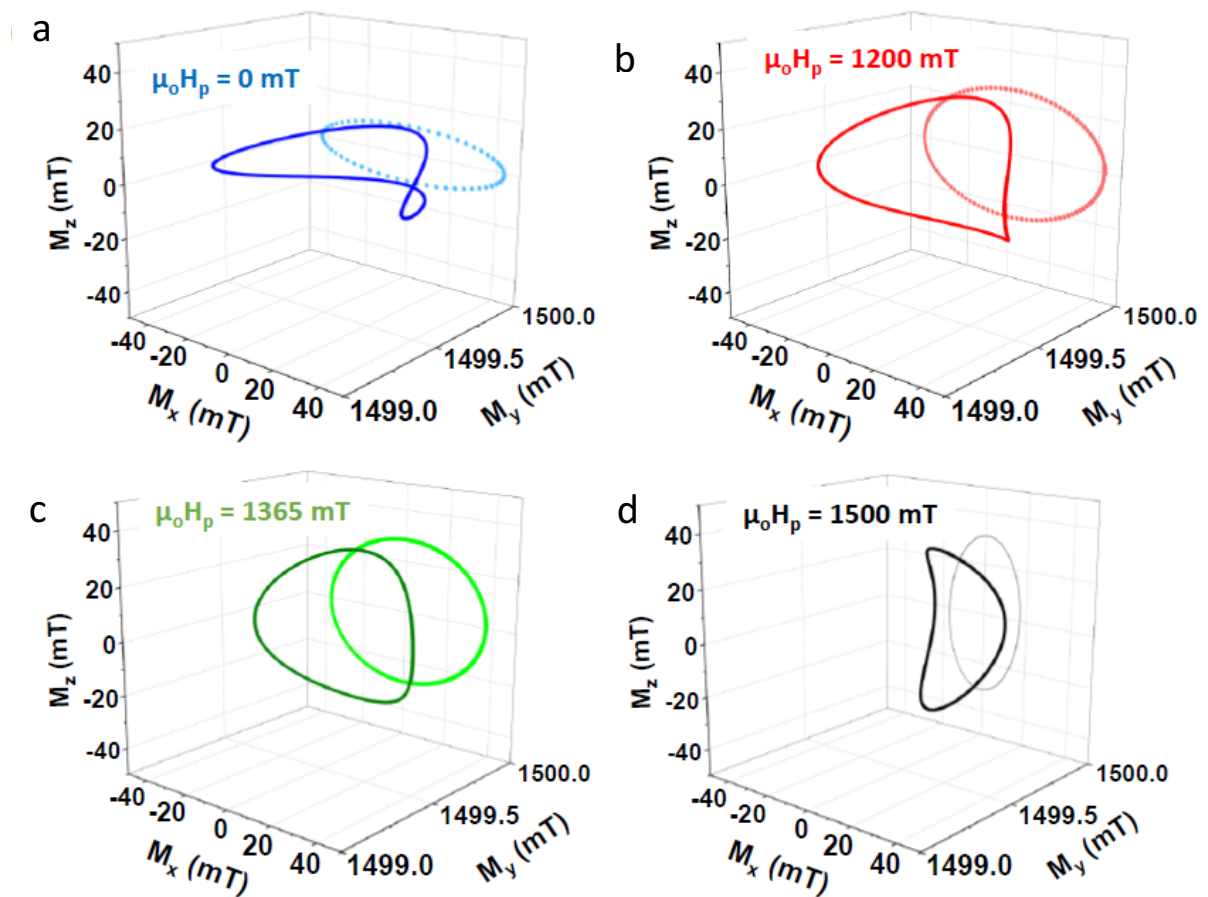


Figure 6.3 a – d, Magnetization precession trajectories for $\mu_0 H_p = 0$ mT to 1500 mT during FMR. Simulations are performed in a frequency sweep mode at $\mu_0 H_{ex,y} = 100$ mT and microwave amplitude $\mu_0 h_{rf,x} = 0.1$ mT.

Figure 6.4c shows the change of ellipticity with respect to PMA in the sample $\mu_0 H_{ex,y} = 100$ mT to 150 mT. The ellipticity approaches 1 as the H_p is increases upto the point where the $H_{d,eff} = 0$, while further increase in H_p results in $A > 1$ because $M_z > M_x$. The corresponding areas of precession trajectories are plotted as a function of PMA for different values of $H_{ex,y}$ in Fig. 6.4d, which shows that it increases upto $\mu_0 H_p \sim 1000$ mT and then gradually decreases for $\mu_0 H_p > 1150$ mT. Such a behavior can be explained by the fact that while M_z increases monotonically with increasing PMA, M_x increases upto $\mu_0 H_p \sim 1000$ mT. Beyond this M_x starts to decrease, until it falls below M_z when $H_p > H_d$ as shown in Fig. 6.4b. From this analysis, we see that the ellipticity and the area of precession can be controlled significantly by the PMA. The spin current generated during such a precession is dependent on the magnitudes of the magnetization components which are transverse to the direction of external magnetic field, i.e., M_x and M_z . It was shown that spin pumping efficiency is directly proportional to the area of the elliptical trajectory [24,25]. From our simulations we can see that this area, and hence the pumping efficiency, is strongly dependent on the PMA. The results presented in Fig. 6.4 show that the pumping efficiency during FMR in an in-plane magnetized CoFeB/MgO junction can be expected to be maximum for $H_p < H_d$, just before the transition of its easy axis from in-plane to perpendicular direction. In terms of spin wave excitation, larger precession cone angles are desirable for improving the spin wave amplitudes [7]. The cone angles which are proportional to the values of M_x and M_z are dependent on the PMA. In CoFeB/MgO junctions, PMA is inversely proportional to the CoFeB thicknesses. Therefore, spin wave amplitudes can be controlled by selecting the CoFeB layer thickness accordingly.

Spin pumping efficiency has been shown to be strongly determined by the ellipticity of a precession trajectory [24,25]. From Fig. 6.4, it can be seen that the ellipticity $A \sim 0.50$ for the case of $1000 \text{ mT} < \mu_0 H_p < 1150 \text{ mT}$, where the area of precession is found to be maximum. In order to check the validity of this result, simulations were performed at different amplitudes of microwave field. Figure 6.5a shows the magnetization precession trajectories during resonance as a function of the excitation amplitude when $\mu_0 H_p = 0$ mT. The ellipticities are found to be independent of the amplitudes of microwave fields as shown in Fig. 6.5b. The corresponding areas of trajectory as a function of PMA are plotted in Fig. 6.5c. It shows that for the range of the applied microwave amplitudes, the area of precession trajectory

always has a maximum close to the value of PMA for which $A \sim 0.5$. It should be noted that the error in estimating the area of trajectory on the Bloch's sphere from its projection on the x-z plane is highest around $\mu_0 H_p = 1000$ mT because the oscillation amplitude of M_y is maximum (Fig. 6.4b). Due to this, at higher microwave amplitudes, area is underestimated around $\mu_0 H_p = 1000$ mT and as a result the PMA dependence of area appears to be relatively flatter as microwave amplitudes increase in Fig. 6.5c.

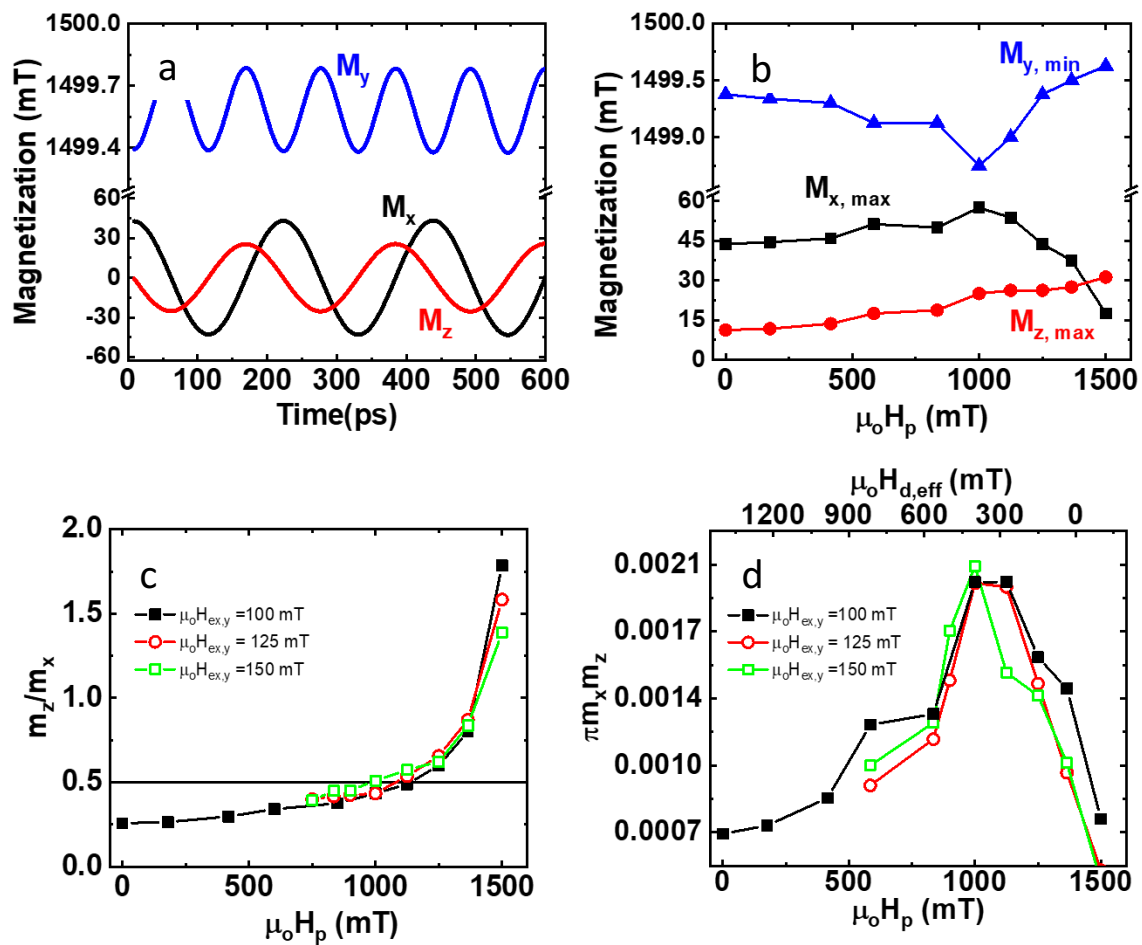


Figure 6.4 **a**, Magnetization components M_x , M_y and M_z as a function of time during FMR for a sample with $\mu_0 H_p = 1250$ mT. **b**, Dependence of the maximum values of M_x and M_z and minimum value of M_y as a function of perpendicular magnetic anisotropy. Simulations are performed in a frequency sweep mode at $\mu_0 H_{ex,y} = 100$ mT. **c**, Effect of H_p on the ellipticity of the magnetization trajectories during FMR. **d**, The corresponding area as a function of H_p . The effective demagnetization field $H_{d, \text{eff}}$ corresponding to the PMA field are shown in the top x-axis. Simulations are performed in a frequency sweep mode at $\mu_0 H_{ex,y} = 100$ mT, 125 mT and 150 mT and microwave amplitude $\mu_0 h_{rf,x} = 0.1$ mT.

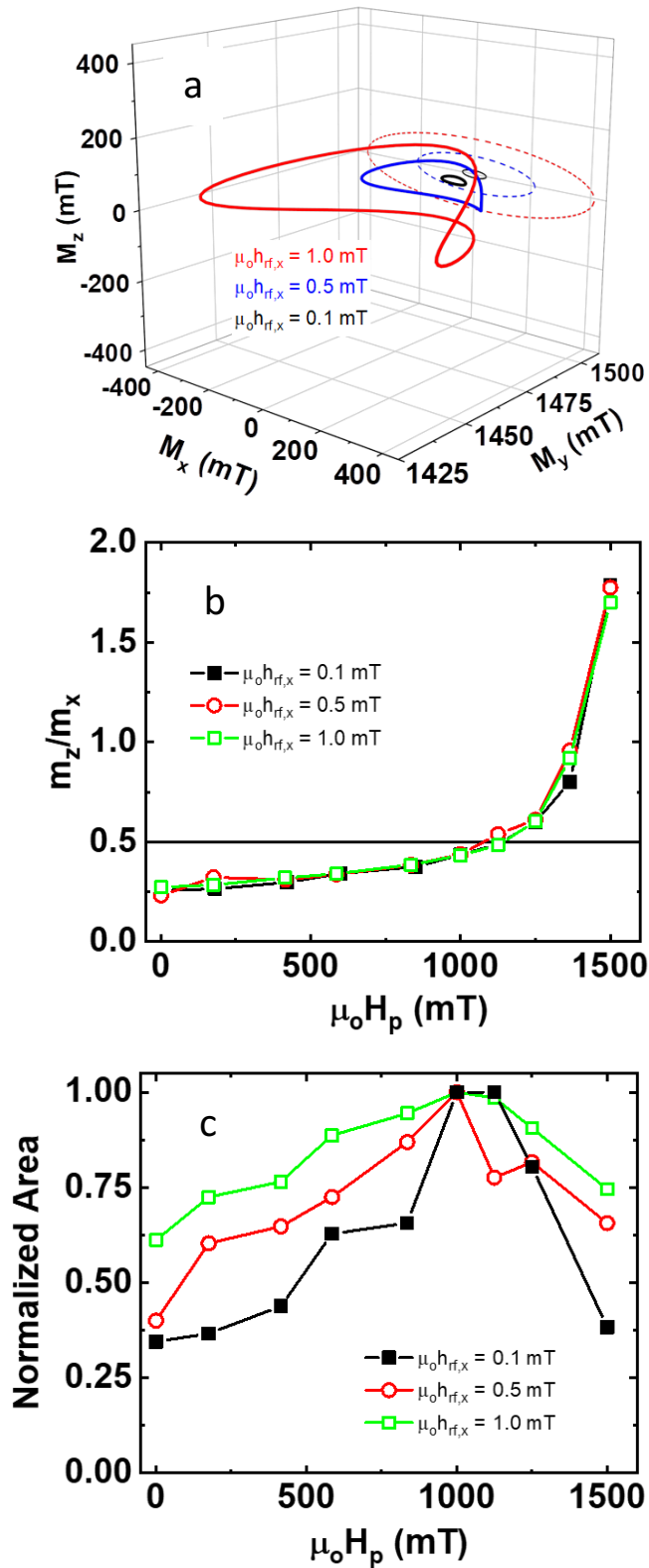


Figure 6.5 a, Magnetization trajectories during FMR at different microwave amplitudes $h_{rf,x}$ at a fixed $\mu_0 H_p = 0 \text{ mT}$ and $\mu_0 H_{ex,y} = 100 \text{ mT}$. **b**, Ellipticity and **c**, area of magnetization precession trajectories as a function of H_p at different $h_{rf,x}$. The areas are normalized with respect to the maximum value obtained for each $h_{rf,x}$.

6.3. Enhanced spin pumping using electric fields

Following the findings of Section 6.2, we investigated if the spin pumping efficiency could be enhanced when the effective demagnetizing field of the CoFeB/MgO junction fulfils the conditions obtained from simulations. For this purpose, we fabricated devices similar to the one described in Section 5.5. As observed in Section 6.2, spin pumping can be expected to be maximum for a sample with an in-plane easy axis, where the demagnetizing field is almost compensated by the PMA field. Therefore, we chose a multilayer stack with CoFeB thickness of 1.9 nm for fabricating spin pumping devices as described earlier in Section 2.4. Typical rectified voltage V_{ISHE} spectra obtained from the electric-field excitation device at frequencies 2 – 8 GHz applied at a power 15 dBm is shown in Fig. 6.6a. Upon fitting using Eq. 5.1, we can obtain the resonance fields corresponding to the particular frequency of applied microwave voltage. Figure 6.7a shows the resonance fields as a function of frequency. We obtain an $M_{\text{eff}} \sim 90$ mT by fitting the data using Eq. 3.3. This shows that the easy axis of the sample is in the film plane and that the PMA field almost compensates the demagnetizing field.

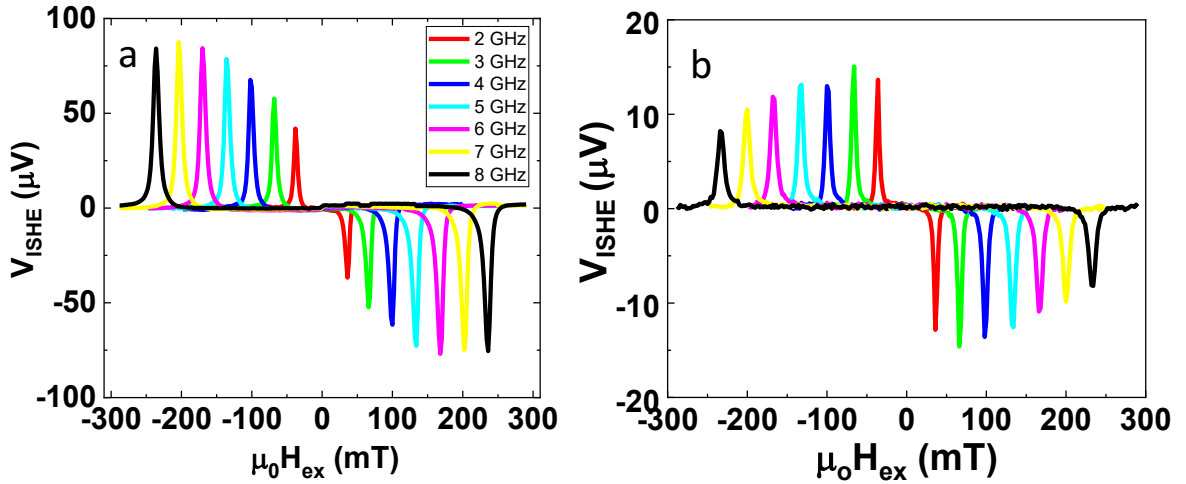


Figure 6.6. Inverse spin Hall effect voltages (V_{ISHE}) from uniform resonance modes for **a**, electric-field and **b**, current controlled device at input frequencies $f = 2$ GHz to 8 GHz applied at 22 dBm.

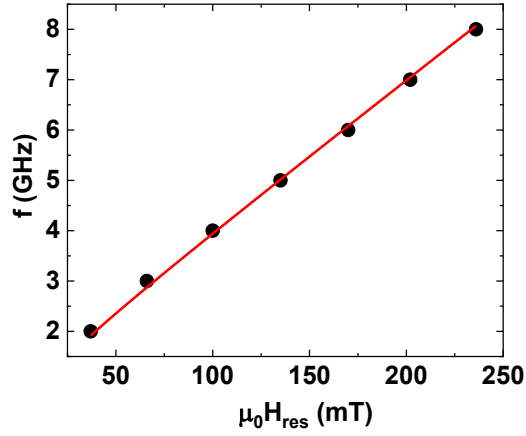


Figure 6.7 Resonance fields H_{res} as a function of frequency f along with fit (line) using Eq. (3.1).

The effect of input power on the amplitude of the rectified voltage spectra is shown for an input microwave signal of 3 GHz in Fig. 6.8a. It can be seen that the amplitude of the rectified voltage increases linearly with the input power upto about 56 mW (17.5 dBm), beyond which it deviates from the linear behaviour and the rectified voltage saturated at about 75 μV . The corresponding data for 7 GHz is also plotted in the same figure which showed the highest rectified voltage in Fig. 6.6a and it also exhibits a similar behaviour as V_{ISHE} for 3 GHz. Rectified voltage obtained from inverse spin Hall effect V_{ISHE} is directly related to the spin current J_s generation by the following relation:

$$V_{\text{ISHE}} = \theta_{\text{SH}} J_s \frac{\lambda_{\text{sd}} L_{\text{NM}}}{\sigma_{\text{NM}} t_{\text{NM}}} \tanh\left(\frac{t_{\text{NM}}}{2\lambda_{\text{sd}}}\right), \quad (6.3)$$

where the conductivity of the Ta(5)/Ru(10)/Ta(5) was estimated to be $\sigma_{\text{NM}} = 4.3 \times 10^6 \Omega^{-1} \text{m}^{-1}$, while its thickness and length are $t_{\text{NM}} = 20 \text{ nm}$ and $L_{\text{NM}} = 250 \text{ um}$ respectively. Spin diffusion length λ_{sd} is taken as 1.4 nm, which is equivalent to that of Ta. In order to estimate the spin Hall angle of the Ta underlayer, we fabricated spin torque ferromagnetic devices (ST-FMR) [33]. The spin Hall angle is estimated to be $\theta_{\text{SH}} \sim 4.5\%$ from the ST-FMR devices. Using these values, we estimated the spin current densities as shown in Fig. 6.8b. For the frequency of 3 GHz, we can see that spin current densities increase linearly

up to $\sim 0.5 \times 10^9 \text{ Am}^{-2}$, beyond which it saturates. The spin current density for 7 GHz was found to reach up to $1.5 \times 10^9 \text{ Am}^{-2}$.

Subsequently, we compared the rectified voltages between electric-field and current controlled devices. For this purpose, we fabricated devices using the same multilayer stack with equal dimensions. The current controlled devices are similar to the ones used for the study in Section 5.2. V_{ISHE} obtained in the electric-field controlled device is found to be clearly higher than that obtained from the current controlled device at an input power of 20 dBm, as seen from Fig. 6.6b. The V_{ISHE} is found to be maximum at 3 GHz. The input power dependence of V_{ISHE} at $f=3 \text{ GHz}$ in the current controlled device is shown in Fig. 6.8a. Using Eq. (6.3) we can estimate the corresponding current densities. A maximum $J_s \sim 8.7 \times 10^7 \text{ Am}^{-2}$ is obtained for current controlled device as shown in Fig. 6.8b, which is comparable with that reported by Feiler *et al.* and Gupta *et al.* [34,35]. A two order increase in the spin current densities for the electric-field compared with the current controlled devices points towards the power efficiency of electric-field controlled magnetization dynamics in spintronic devices.

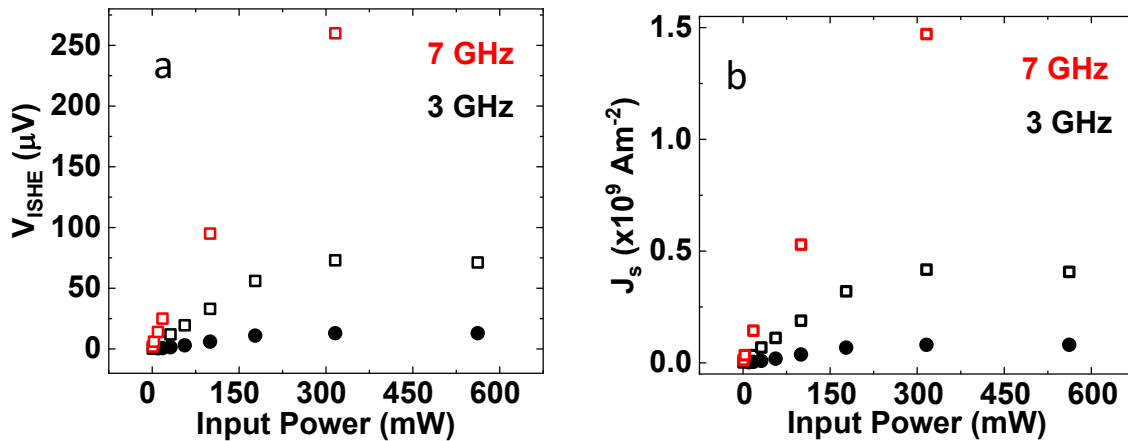


Figure 6.8a, Inverse spin Hall effect voltages (V_{ISHE}) and **b**, corresponding spin current densities J_s from uniform resonance modes for electric-field (squares) and current controlled (circles) devices at input frequencies $f=3 \text{ GHz}$.

6.4. Power dependent inverse spin Hall spectra

Following our observations of enhanced spin pumping in the electric-field controlled devices, we investigated the effect of input power P_{in} on the rectified voltage spectra. As discussed in Section 6.1, magnetization dynamics at high P_{in} are especially important to understand various spintronic device operations. Figure 6.9 shows the V_{ISHE} spectra at $f = 2$ GHz as a function of P_{in} from 0 dBm to 27.5 dBm. Aside from an obvious increase in the rectified voltage intensity of the uniform ferromagnetic resonance peak at $\mu_0 H_{\text{ex}} = 32$ mT, several distinct features emerge from the spectra at higher excitation powers. Firstly, at high excitation powers, the lineshape of the rectified voltage obtained at $\mu_0 H_{\text{ex}} \sim 33$ mT deviates from purely symmetric behavior. The second, and most remarkable, is the emergence of a subsidiary peak at $\mu_0 H_{\text{ex}} \sim 11$ mT. Such a peak is due to the parametric excitation of FMR. Both these scenarios are discussed in this section.

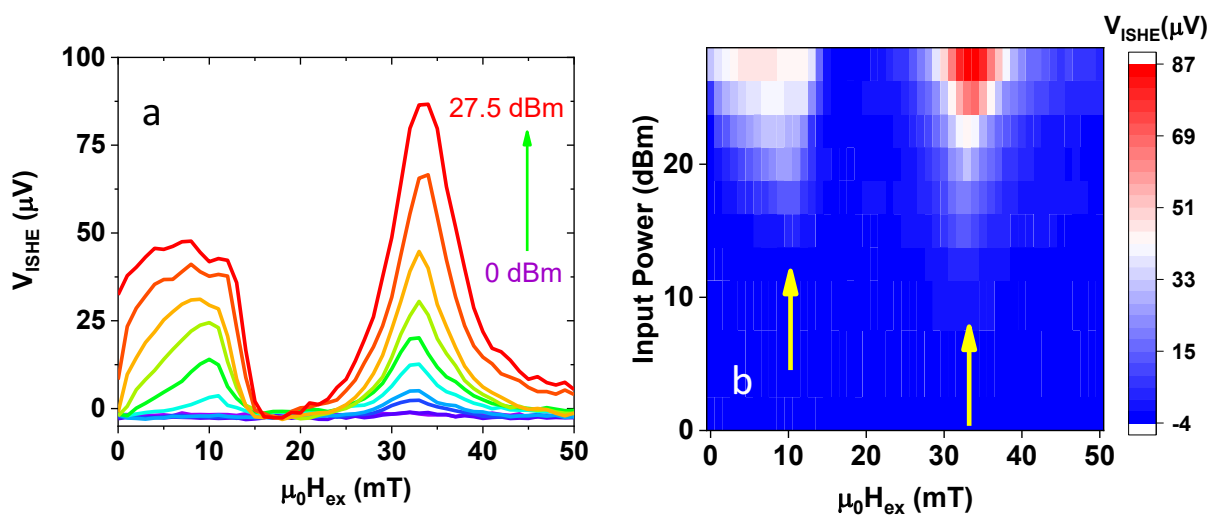


Figure 6.9a, Inverse spin Hall effect voltages (V_{ISHE}) spectra as a function of input power for the electric field controlled device at a frequency $f = 2$ GHz. **b**, Corresponding data is shown as a color map indicating the positions of uniform and parametric resonance fields (arrows).

6.4.1. Change of lineshapes of uniform resonance peak at higher excitation power.

As observed in Fig. 6.9a, the rectified voltage of the uniform resonance peak increases with an increase in the input microwave power. Since the corresponding ac magnetic field is proportional to the $P_{\text{in}}^{1/2}$, the maxima of the rectified voltages are plotted as a function of $P_{\text{in}}^{1/2}$ in Fig. 6.10. It can be seen that upto $P_{\text{in}}^{1/2} = 7.5 \text{ mW}^{1/2}$, V_{ISHE} of the uniform FMR (UFMR) mode increases as a function of P_{in} , beyond which it starts to saturate. This can be understood from the deviation of V_{ISHE} from the fit to square dependence on $P_{\text{in}}^{1/2}$ at higher powers. Typically, at low excitation powers, only UFMR mode is excited. The deviation from the fit in Fig. 6.10a happens because along with the UFMR mode, spin wave modes with $k \neq 0$ are also excited. Such an excitation also gives rise to additional effects such as enhancement of the resonance linewidth and contributes to the asymmetric lineshape of the rectified voltage spectra as observed earlier in Fig. 6.9a. Lustikova *et al.* investigated the effect of excitation powers on V_{ISHE} lineshapes in YIG/Pt systems [36]. Although it is possible for the opening up of cone angle or heating up of the sample to give rise to asymmetry in the lineshapes, it was found that such origins could not explain the observed asymmetry at high powers in YIG/Pt bilayers. Based on this, the asymmetry was explained using the non-linearity in the samples arising from spin wave excitations.

In addition, an increase in H_{res} of UFMR mode is also observed, which is more pronounced in lower frequencies as shown in Fig. 6.10b. Such an increase in H_{res} can be attributed to the decrease in demagnetizing field H_{d} because of a reduced static magnetization M_{s} of the sample at high excitation powers. Zhang *et al.* measured the FMR spectra of YIG thin films under different orientations of static and microwave fields and explained that both spin wave instabilities and larger precession cone angles have to be considered to quantitatively account for such a decrease [37]. Additionally, the frequency dependence of such a shift has been explained using the excitation of forward volume waves at lower magnetic fields by Khivintsev *et al.* [38]. It is interesting to note that the onset of the non-linear regime also marks the emergence of the parametric resonance peak as shown in Fig. 6.10a. The parametric resonance will be discussed in the following section.

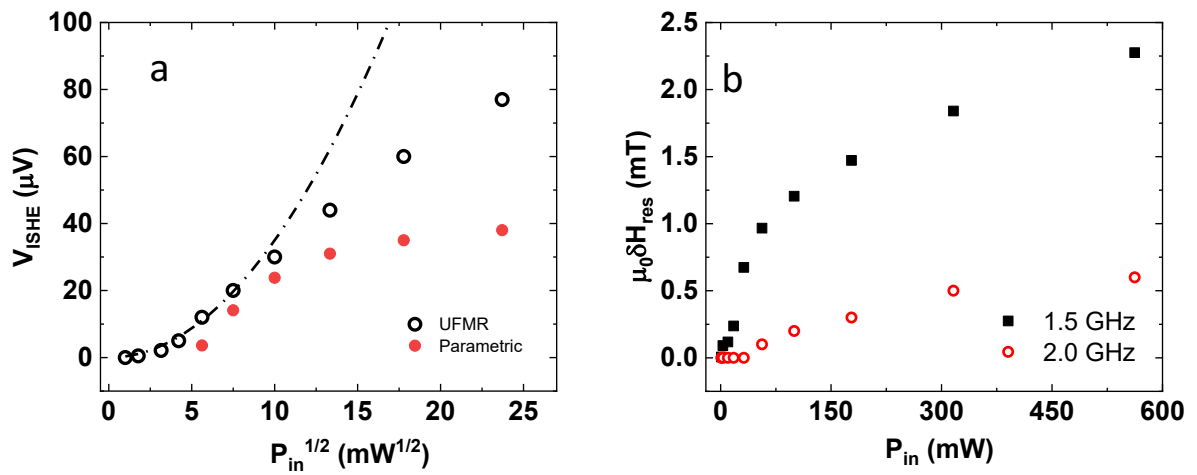


Figure 6.10 a, Inverse spin Hall effect voltages (V_{ISHE}) amplitudes of the uniform and parametric peaks as a function of square root of input power for the electric field controlled device at a frequency $f = 2$ GHz. **b**, Change in the resonance field δH_{res} with respect to H_{res} at 5 dBm in case of the uniform resonance mode as a function of power.

6.4.2. Parametric resonance using electric-fields.

Parametric excitation is typically classified into two types, depending on the orientation of the external magnetic field that defines the direction of the magnetization vector M and the microwave field. Experiments carried out by Bloombergen and Wang revealed two interesting anomalies in the FMR spectra at high excitation powers [20]. When an ac magnetic field is applied perpendicular to M , a uniform precession mode can be excited. FMR occurs when the frequency of the ac field matches with that of such a uniform precession mode. As the excitation power increases, precession amplitude increases upto a certain point, beyond which it is expected to saturate. However, their experiments revealed that the threshold power required to saturate the FMR amplitude can be achieved at a hundredth of the field expected from earlier theory. Additionally, a subsidiary peak was observed at similar power levels at a field much below the uniform resonance peak. Suhl first developed the theory for such anomalies in the FMR at high excitation power [19]. The major consideration behind his theory was the fact that uniform ferromagnetic resonance and spin wave modes present in the magnetic system are coupled to each other. Therefore, when the ac field of frequency ω_p excites a uniform magnetization precession, it can subsequently amplify the spin wave modes. The threshold ac field required to excite such spin wave modes is given by Eq. (6.4) below:

$$h_t^\perp = \frac{1}{|\rho|} \sqrt{\omega_{rk}^2 + \left(\frac{\omega_p}{2} - \omega_k\right)^2} \quad , (6.4)$$

where, ρ is the and ω_{rk} is . From this equation it can be easily seen that the threshold is lowest for spin waves with frequency $\omega_{k\perp} = \omega_p/2$. This explains the emergence of the subsidiary peak the experiments by Bloombergen and Wang. Since the ac magnetization that mediates as the pumping mode is transverse to the static magnetization, this case is called *perpendicular* pumping.

In addition to the perpendicular pumping, Kavanov and Tsukernik first predicted the possibility of absorbing energy from an ac magnetic field applied parallel to the static magnetization i.e. parallel pumping [39]. It was first experimentally observed by Schlomann, Green and Milano wherein instead

of an ac magnetization, the parametric resonance was seen to be excited if an ac magnetic field of sufficient magnitude is applied parallel to the static magnetization [40]. As discussed earlier in Section 6.2, whenever the magnetization trajectory follows an elliptical trajectory around an external magnetic field, the component of magnetization parallel to H_{ex} oscillates at twice the frequency $2\omega_{\text{k//}}$ of the transverse components. Such oscillations or spin wave modes can typically exist in ferromagnets owing to thermally induced stochastic processes. Therefore, even when an oscillating field of frequency ω is applied parallel to the static magnetization, there is a possibility for such spin wave modes to absorb energy from the pumping field. The absorption of energy from the pumping field in this mechanism is maximum when $\omega = 2\omega_{\text{k//}}$. It should be noted that the ellipticity of a magnetization trajectory is a necessary condition for this type of parametric excitation process [17].

The threshold field of parallel pumping mechanism $h_t^{\text{//}}$ is given by the minimum value of the expression below:

$$h_t^{\text{//}} = \frac{\omega}{\omega_M} \min\left(\frac{\Delta H_k}{\sin^2 \theta_k}\right) \quad , (6.5)$$

where, ω_M is the frequency corresponding to effective demagnetizing field, ΔH_k is the linewidth and θ_k is the angle between the spin wave vector and H_{ex} . Such a dependence indicates that this excitation mechanism is most likely to couple with spin waves travelling at an angle $\theta_k = 90^\circ$ with respect to H_{ex} . An important outcome of Eq. (6.5) is that the threshold field is low for samples with higher M_{eff} . However, as seen earlier from Fig. 6.4b, the amplitude of M_y (i.e. the component of magnetization oscillating at twice the natural frequency) is lower at higher value of M_{eff} . This would lower the coupling of the driving rf field to the spin wave modes of the ferromagnet via parallel pumping mechanism. Maximum amplitude of the magnetization component δM_y was seen to be achieved for $H_{\text{d,eff}} \sim 300$ mT. Additionally, the linewidth of ferromagnetic systems are a major factor in determining the ability to excite parametric pumping. This is why a majority of the early reports on parametric excitation is for magnetic systems such as YIG with low demagnetizing fields and ultralow damping [13-14]. Recently,

ultralow damping of 0.002 was demonstrated for 10 nm thick thin films of Co – Fe based alloys [41]. It should be noted that we obtain a damping factor of ~ 0.005 for our multilayers with 5 nm thick CoFeB layers. In case of the electric-field controlled devices which have a CoFeB thickness of 1.9 nm, the damping factor is ~ 0.018 , which is reasonable due to the reduced thickness. An increase in the damping in ultrathin films can be expected due to an increase in the contributions from interfacial spin orbit coupling.

Microstrips and coplanar waveguides have emerged as a popular candidate for exciting forced spin wave excitations towards developing spintronics applications. Typically, in case of parametric excitations using microstrips and waveguides for the flow of currents, both parallel and perpendicular pumping components are present. Using a systematic study of for microstrip and dielectric resonators, Neumann *et al.* explained the differences in the excitation regimes where the parallel and perpendicular pumping mechanisms are dominant [42]. For a microstrip resonator, a critical field H_c is defined upto which parallel pumping is dominant. For $H_{ex} > H_c$, a significant jump in the threshold field is observed. Such an increase is attributed to the onset of perpendicular pumping mechanism above H_c . The expression for H_c can be written as follows:

$$H_c = -\frac{M_{eff}}{2} + \sqrt{\left(\frac{M_{eff}}{2}\right)^2 + \left(\frac{\omega}{2\gamma}\right)^2}, \quad (6.6)$$

Electric-fields are not only localized but are also highly directional. Nonetheless, it should be noted that both parallel and perpendicular pumping fields could be possible in our samples magnetized along $\theta = \phi = 0$ degree. While the former is the oscillating field generated by the VCMA of H_k , the possibilities for the latter are the VCMA of H_p and y-axis microwave field as explained using the COMSOL simulations in Section 5.4. Therefore, it becomes imperative for us to consider all scenarios during our investigation of the origin of parametric pumping process in our samples. Following the findings of Neumann *et al.*, we measured the rectified voltage spectra at different frequencies. Figure 6.11a shows the spectra at 22 dBm input power from frequencies $f = 1.0$ GHz to 4.0 GHz. The fields corresponding to the emergence of the parametric peaks at threshold power is plotted in Figure 6.11b.

These fields as a function of pumping frequency fit well to Eq. (6.6) using $M_{\text{eff}} = 88$ mT, which is similar to the value obtained from the Kittel fitting of the uniform resonance mode of the same device as shown in Fig. 6.7a. In addition, as seen earlier from the power dependent spectra in Fig. 6.9a, the excitation of parametric instability at $H_{\text{ex}} > H_c$ is highly suppressed, unlike at $H_{\text{ex}} < H_c$. Such a behaviour indicated that the mechanism of excitation of parametric resonance in our samples is parallel pumping due to the VCMA of an in-plane magnetic anisotropy.

Subsequently, if this excitation is due to the parallel pumping, it should scale as a function of $\sin^2\theta_k$. In our device geometry, spin waves are most likely to propagate along the y-axis i.e. $\phi = 90$ degree. We measured the in-plane angle dependence of the parametric resonance peak amplitude as plotted for $f = 3$ GHz in Fig. 6.11c. The peak amplitudes can be fit using $\cos^3\phi$. Kurebayashi *et al.* have shown that detection of magnons using ISHE is independent of the wavenumber k [43]. As discussed in Section 5.4, detection of magnetization dynamics using ISHE should scale as a function of $\sin\phi$ for our sample geometry. A $\cos^3\phi$ dependence shows that the decrease in parametric amplitude is not only because of detection efficiency but also due to excitation efficiency as ϕ increases from 0 to 90 degree. This can be attributed to the decrease in excitation efficiency as a function of $\sin^2\theta_k$. Additionally, it should be mentioned here that electric-field modulation of H_p is always perpendicular to H_{ex} in the in-plane magnetized film geometry. Therefore, if the parametric excitation is due to VCMA of H_p , it should only scale as a function of $\sin\theta$. By using such a symmetry argument, we can nullify the effect of VCMA of H_p in this case.

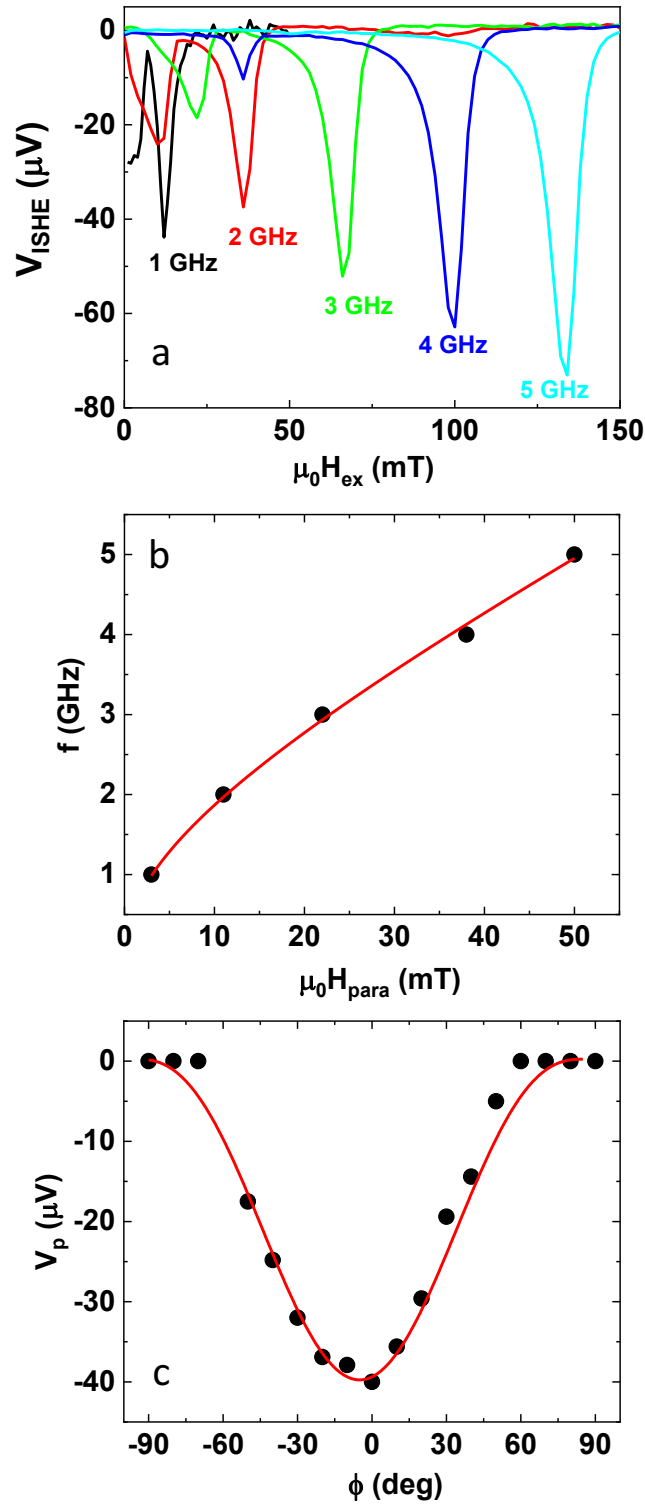


Figure 6.11 a, Inverse spin Hall effect voltages (V_{ISHE}) spectra as a function of frequency for the electric field controlled device at input power of 22.5 dBm. **b**, External field at which the parametric peak first emerges at threshold power (H_{para}) as a function of frequency with fit using Eq. (6.6). Peak amplitude of the parametric peak V_p as a function of ϕ , with fit using $\cos^3 \phi$.

6.5. Conclusions

In conclusion, we discussed the effect of PMA on the dynamical magnetization trajectories during FMR in nanostructured CoFeB using micromagnetic simulations. The two magnetization components transverse to the static field applied in the y-direction was found to have different PMA dependent behavior. While the M_z component increased monotonically with increasing PMA, the M_x component increased upto $\mu_0 H_p \sim 1000$ mT, beyond which it decreased. This results in a non-monotonous PMA dependent area of magnetization trajectory during excitation of FMR. This area is found to be maximum around the condition where $M_z: M_x \sim 1:2$. Such a behavior is found to be independent of the excitation power in the range of applied microwave field amplitudes. Subsequently spin pumping efficiency is compared between an electric-field and a current controlled device. Spin current density pumped from the electric-field controlled excitation of FMR was found to be upto 2 order higher than the current controlled excitation in our devices. Finally, we demonstrated that parametric pumping can be excited using VCMA of IMA in an in-plane magnetized CoFeB/MgO junction. We believe these findings are a significant step towards the development of both spin current and magnon based information processing.

References

1. J.E. Hirsch, *Phys. Rev. Lett.* **83**, 1834 (1999).
2. M. Johnson and R.H. Silsbee, *Phys. Rev. Lett.* **55**, 1790 (1985).
3. K. Uchida, S. Takahashi, K. Harii, J. Ieda, W. Koshibae, K. Ando, S. Maekawa and E. Saitoh, *Nature* **455**, 778-781 (2008).
4. Y. Tserkovnyak, A. Brataas and G.E.W. Bauer, *Phys. Rev. B* **66**, 224403 (2002).
5. T. Nozaki, Y. Shiota, S. Miwa, S. Murakami, F. Bonell, S. Ishibashi, H. Kubota, K. Yakushiji, T. Saruya, A. Fukushima, S. Yuasa, T. Shinjo and Y. Suzuki, *Nat. Phys.* **8**, 491–496 (2012).
6. J. Zhu, J.A. Katine, G. E. Rowlands, Y-J. Chen, Z. Duan, J.G. Alzate, P. Upadhyaya, J. Langer, P.K. Amiri, K.L. Wang and I.N. Krivorotov, *Phys. Rev. Lett.* **108**, 197203 (2012).
7. B. Rana, Y. Fukuma, K. Miura, H. Takahashi and Y. Otani, *Appl. Phys. Lett.* **111**, 052404 (2017).
8. V.V. Kruglak, S.O. Demokritov and D. Grundler, *J. Phys. D: Appl. Phys.* **43**, 264001 (2010).
9. A. Khitun, K.L. Wang, *J. Appl. Phys.* **110**, 034306 (2011).
10. M. Macia, A.D. Kent and F.C. Hoppensteadt, *Nanotechnology* **22**, 095301 (2011).
11. R. Nakane, G. Tanaka and A. Hirose, *IEEE ACCESS* **6**, 4462 (2018).
12. Y. Kajiwara, K. Harii, S. Takahashi, J. Ohe, K. Uchida, M. Mizuguchi, H. Umezawa, H. Kawai, K. Ando, K. Takanashi, S. Maekawa and E. Saitoh, *Nature* **464**, 262–266 (2010).
13. A.A. Serga, A.V. Chumak and B. Hillebrands, *J. Phys D: Appl Phys* **43**, 26 (2010).
14. A.V. Chumak, V.Y. Vasyuchka, A.A. Serga and B. Hillebrands, *Nat. Phys.* **11**, 453–461 (2015).
15. J.S. Slonczewski, *J. Magn. Magn. Mater.* **159**, L1-L7 (1996).
16. L. Berger, *Phys. Rev. B* **54**, 9353-9358 (1996).
17. A.G. Gurevich and G.A. Melkov, *Magnetization Oscillations and Waves*; CRC Press: Boca Raton, FL, (1996).
18. P.W. Anderson and H. Suhl, *Phys. Rev.* **100**, 1788 (1955).
19. H. Suhl, *J. Phys. Chem. Solids* **1**, 209 (1957).
20. N. Blombergen and S. Wang, *Phys. Rev.* **93**, 72 (1954).
21. C.W. Sandweg, Y. Kajiwara, A.V. Chumak, A.A. Serga, V.Y. Vasyuchka, M. B. Jungfleisch, E. Saitoh, and B. Hillebrands, *Phys. Rev. Lett.* **106**, 216601 (2011).
22. E. Sagasta, Y. Omori, S. Velez, R. Llopis, C. Tollan, A. Chuvillin, L.E. Hueso, M. Gradhand, Y. Otani and F. Casanova, *Phys. Rev. B* **98**, 060410 (2018).
23. Y. Fukuma, L. Wang, H. Idzuchi, S. Takahashi, S. Maekawa and Y. Otani, *Nat. Mater.* **10**, 527-531 (2011).
24. K. Ando, T. Yoshino and E. Saitoh, *Appl. Phys. Lett.* **94**, 152509 (2009).
25. K. Ando, S. Takahashi, J. Ieda, Y. Kajiwara, H. Nakayama, T. Yoshino, K. Harii, Y. Fujikawa, M. Matsuo, S. Maekawa, and E. Saitoh, *J. Appl. Phys.* **109**, 103913 (2011).

26. B. Rana, Y. Fukuma, K. Miura, H. Takahashi and Y. Otani, *Sci. Rep.* **7**, 2318 (2017).
27. T. Maruyama, Y. Shiota, T. Nozaki, K. Ohta, N. Toda, M. Mizuguchi, A.A. Tulapurkar, T. Shinjo, M. Shiraishi, Y. Ando and Y. Suzuki, *Nat. Nanotechnol.* **18**, 158-161 (2009).
28. Y. Shiota, T. Nozaki, F. Bonell, S. Murakami, T. Shinjo and Y. Suzuki, *Nat. Mater.* **11**, 39–43 (2012).
29. LLG Micromagnetics developed by M.R. Sheinfein and E.A. Price.
30. J. M. Shaw, H.T. Nembach, M. Weiler, T.J. Silva, M. Schoen, J.Z. Sun and D.C. Worledge, *IEEE Magn. Lett.* **6**, 1-4 (2015).
31. S. Chikazumi, “International series of monographs on physics 94: Physics of Ferromagnetism”, Oxford University Press (2009).
32. T. Maruyama, Y. Shiota, T. Nozaki, K. Ohta, N. Toda, M. Mizuguchi, A.A. Tulapurkar, T. Shinjo, M. Shiraishi, S. Mizukami, Y. Ando and Y. Suzuki, *Nat. Nanotech.* **4**, 158–161 (2009).
33. L. Liu, T. Moriyama, D.C. Ralph and R.A. Buhrman, *Phys. Rev. Lett.* **106**, 036601 (2011).
34. L. Feiler, K. Sentker, M. Brinker, N. Kuhlmann, F.-U. Stein and G. Meier, *Phys. Rev. B* **93**, 064408 (2016)
35. S. Gupta, R. Medwal, D. Kodama, K. Kondou, Y. Otani and Y. Fukuma, *Appl. Phys. Lett.* **110**, 022404 (2017).
36. J. Lustikova, Y. Shiomi, Y. Handa, E. Saitoh, *J. Appl. Phys.* **117**, 073901 (2015).
37. Y.T Zhang, C.E. Patton and G. Srinivasan, *J. Appl. Phys.* **63**, 5433 (1988).
38. Y. Khivintsev, B. Kuanr, T.J. Fal, M. Haftel, R.E. Camley, Z. Celinski and D.L. Mills, *Phys. Rev. B* **81**, 054436 (2010).
39. M.I. Kaganov and V.M. Tsukernik, *Sov. Phys. JETP* **10**, No. 3, 587, (1960).
40. E. Schlomann, J.J. Green and U.J. Milano, *J. Appl. Phys.* **31**, No. 5, Suppl., 386S, (1960).
41. M.A.W. Schoen, D. Thonig, M.L. Schneider, T.J. Silva, H.T. Nembach, O. Eriksson, O. Karis and J.M Shaw, *Nat. Phys.* **12**, 839–842 (2016).
42. T. Neumann, A.A. Serga, V.Y. Vasyuchka, and B. Hillebrands, *Appl. Phys. Lett.* **94**, 192502 (2009).
43. H. Kurebayashi, O. Dzyapko, V. E. Demidov, D. Fang, A. J. Ferguson and S. O. Demokritov, *Appl. Phys. Lett.* **99**, 162502 (2011).

Conclusions and future outlook based on the results reported in this thesis

In this thesis we performed a series of experiments and simulations to investigate the possibility of controlling magnetization purely using electric-fields in an easy cone state and by controlling of the symmetry of interfacial anisotropy. We use CoFeB/MgO junctions owing to their VCMA and high value of interfacial anisotropy. Initially we perform a systematic study of magnetic anisotropy in CoFeB/MgO junctions using magnetic annealing and temperature dependent FMR measurements. We notice that the symmetry of interfacial anisotropy can be controlled to have an in-plane component, in addition to the perpendicular anisotropy. Micromagnetic simulations were performed to investigate the use of easy cone state of CoFeB thin films in the field of purely voltage induced magnetization switching. Since the stable state is at an intermediate direction from the in-plane and perpendicular to the film plane, a non-zero electric field can be expected in the stable configuration. This is useful for purely electric-field control of magnetization. The switching speeds were found to decrease with an increase in the cone angle of stable state in the easy cone state. The cone angle on the other hand depends on the magnetic anisotropy of the sample. Thus, such an understanding can enable us to design MRAMs by tuning the magnetic anisotropy of the devices.

Following this, we investigated purely voltage-controlled magnetization by changing the symmetry of interfacial anisotropy. Typically, interfacial anisotropy is perpendicular to the film surface. However, our FMR measurements indicated that an in-plane magnetic anisotropy (IMA) can also be interfacial, in addition to perpendicular magnetic anisotropy (PMA). So using an electrical detection of FMR, we studied the change in magnetic anisotropy by applying bias electric fields at the CoFeB/MgO junction interface. We demonstrated that both IMA and PMA could be modulated by a DC voltage. Following this, we investigated the effect of microwave voltages and saw that the VCMA of IMA enables us to have non-zero electric-field torque on the magnetization and thereby allows us to excite FMR in an in-plane magnetized

CoFeB/MgO junction. Such an electric-field excitation is useful for purely voltage-controlled magnetization of a metallic ferromagnet.

Micromagnetic simulations indicated that the optimum condition for spin current generation using spin pumping is achieved when the ferromagnet has an in-plane easy axis with the PMA slightly lower than the demagnetizing field. Experimental results from electric-field controlled devices with different values of effective demagnetizing fields exhibit a similar behavior. Most interesting observation was that the spin current generation in electric-field controlled devices generated up to 2 order higher spin current density compared to the current controlled device. Pure spin currents can act as a non-scalar quantity because they are caused by flow of the electronic spins. Thus they can be useful for control of magnetic logic devices. The existing logic device architectures face limitations due to higher current densities and tunneling effects as the size of field effect transistors are reduced. This could be overcome using spin current based FET, which is where our findings of enhanced spin pumping can be applicable.

However, it should be noted that most spin currents in metals disappear in very short length scales due to the low diffusion lengths. Such a limitation can be overcome by the transmission of information using spin waves instead of spin currents. Spin waves can have up to three order higher diffusion lengths in metals and also coherently carry the information of phase. This is very useful to overcome the limitations of spin currents in logic applications. The wavelengths of spin waves are limited by the excitation area. This is a major drawback towards device miniaturization. Therefore, a mechanism to excite spin waves with shorter wavelengths is desirable. This is often attempted using parametric excitation of resonance which can help us to reach wavelengths down to the exchange interaction ranges. Parametric excitation is typically excited using electric currents. Being a non-linear process, current excitation results in a high-power consumption. Thus electric-field excitation of parametric resonance is desirable. We demonstrated that using VCMA, parametric resonance can be achieved in our CoFeB/MgO junctions. This can enable us to excite spin waves shorter than the excitation area. Therefore, the ability to excite spin waves with

wavelengths tunable down to few nanometers using electric-fields can be useful for low power spinwave based logic devices along with an ability to scale down such magnonic logic devices.

In conclusion, we studied the possibilities for purely electric-field control of magnetization using CoFeB/MgO junctions in this thesis. At present spin transfer torque and spin orbit torques are most commonly utilized to achieve magnetization switching in MRAMs and spin wave excitation. Compared to STT and SOT, VCMA promises to further reduce power consumption in spintronic devices because it does not require the flow of charge currents. But purely electric-field control of magnetization has not been possible so far due to a perpendicular symmetry of interfacial anisotropy. We have demonstrated that such a limitation of electric-field controlled magnetization can be overcome using an easy cone state or by controlling the symmetry of interfacial anisotropy. The experiments and simulations performed in this thesis help us to understand the control of magnetization in metallic ferromagnets purely using electric-fields and enable us to design power efficient spintronic devices for memory and logic applications.

ACKNOWLEDGEMENTS

At the very outset, I would like to sincerely thank my supervisor Prof. Yasuhiro Fukuma from Kyushu Institute of Technology for agreeing to supervise me for my doctoral degree and nurturing me into a much better researcher than I could otherwise have been. His help with my experiments and simulations, the freedom in performing research in the laboratory, his critical evaluation of my results and collaborative research with brilliant researchers from different laboratories has definitely enabled me to approach scientific research in a very inquisitive, responsible and independent manner.

I would also like to thank Prof. Hironori Asada for providing his laboratory facilities in Yamaguchi University for a lot of my research work and also agreeing to be the reviewer of my PhD thesis. I am also very thankful to Prof. Edmund S. Otabe and Prof. T. Okamoto from Kyushu Institute of Technology for reviewing my thesis.

My thanks are due to Prof. Yoshichika Otani, who provided access to several advanced experimental facilities in RIKEN without which my thesis would not be complete. In addition, despite being an extremely busy academic, I am grateful that he took time out of his busy schedule to comment on my research at various stages. I am particularly thankful to Dr. Bivas Rana from RIKEN who helped me a lot with device fabrication and scientific understanding. He has always been ready to discuss and help me out with my doubts over the past several years. I am especially grateful for the long discussions during the early stages of my PhD, without which I could not have become accustomed to my field of research fast enough. I am also grateful to Dr. Katsuya Miura and Dr. Hiromasa Takahashi from Hitachi for providing me such high quality magnetic multilayers for the experiments in my thesis.

I am thankful to Dr. Surbhi Gupta and Dr. Rohit Medwal, currently in Nanyang Technological University, for helping me start my PhD in this group and then teaching me the various experimental techniques in the laboratory during their tenure at Kyushu Institute of Technology. I would also like to

acknowledge the help of Mr. Ryo Anami for helping me with the device fabrication. I am also extremely grateful to my fellow laboratory members that I had the opportunity to work with during the course of my PhD, especially Kajiwara, Shashank, John, Utkarsh, Shibata, Matsui and Tanaka for their help both inside and out of the laboratory.

As for the people outside of work, first and foremost, I would like to thank my parents and sister for constantly being there for me and supporting me throughout my PhD. I could never have imagined aiming for an advanced educational degree like a PhD without their constant motivation and support. In the same breath, I would also like to thank Miwa for treating me like family in Iizuka. I am thankful to all my friends that I met in this university, especially Kobayashi-san and Prakash for their continued help and support since my arrival in Japan. The new friends from different parts of the world that I made over the course of my PhD definitely helped me to understand diverse cultures from across the world and broaden my views, which I feel is equally important in the life of a student.

I really could not have been able to complete my PhD without the support of all the aforementioned people and many more from the wonderful city of Iizuka. Thank you all so much.

Angshuman Deka

Kyushu Institute of Technology, Japan

June 2020